UNIVERSITÀ DEGLI STUDI DI PADOVA

Plasmonic Gratings for Sensing Devices

Scuola di Dottorato di Ricerca in Fisica

XXIV Ciclo

Direttore della scuola: Ch.mo Prof. Andrea Vitturi

Supervisore: Ch.mo Prof. Filippo Romanato

Dottorando: Gianluca Ruffato

To my parents

Abstract

In last decades surface plasmon resonance has known an increasing interest in the realization of miniaturized devices for label-free sensing applications. The research in the direction of such plasmonic sensors with innovative performance in sensitivity and resolution opened to a wide range of unexpected physical phenomena. This work is aimed at understanding and modeling the physical principles of plasmonic platforms which support the exploitation of propagating plasmon modes for sensing purposes. Surface plasmon polaritons excitation and propagation on metallic gratings have been deeply studied and fully analyzed with theoretical models, numerical simulations and optical characterizations of fabricated samples. In particular the physics underlying azimuthal rotation of these nanostructures and the polarization role in this configuration have been theoretically and experimentally examined. The rotated configurations revealed considerable benefits in sensitivity and this improvement has been demonstrated by analyzing the optical response to surface functionalization and liquid solutions flowing through an embodied microfluidic cell. The exploitation of this plasmonic phenomenon in the conical mounting led to the design and realization of a promising setup for a new class of compact and innovative grating-based sensors. The different approaches, modeling − numerical − experimental, through which the problem has been examined, provided an exhaustive investigation into the physics of grating-coupled surface plasmon resonance and its innovative and original applications for advanced sensing devices.

Abstract

Negli ultimi decenni la risonanza plasmonica di superficie ha conosciuto un crescente interesse nella realizzazione di dispositivi minaturizzati per applicazioni sensoristiche label-free. La ricerca nella direzione di sensori plasmonici con prestazioni innovative in sensibilita' e risoluzione ha aperto ad un vasto panorama di inattesi fenomeni fisici. Questo lavoro di tesi ha l'obbiettivo di capire e analizzare i pricipi fisici su cui si basano i supporti plasmonici che sfruttano l'eccitazione di onde di superficie per fini sensoristici. L'eccitazione e la propagazione di plasmoni polaritoni di superficie su reticoli metallici sono state studiate e analizzate a fondo con modelli teorici, simulazioni numeriche e caratterizzazioni ottiche di campioni nanofabbricati. Nello specifico la fisica della rotazione azimutale di queste nanostrutture e il ruolo della polarizzazione in questa configurazione sono state esaminate con strumenti sia teorici che sperimentali. La rotazione del reticolo plasmonico ha rivelato considerevoli benefici in sensibilita' e questo effetto e' stato testato e dimostrato analizzando la risposta ottica a funzionalizzazioni di superficie e tramite l'analisi di soluzioni liquide flussate attraverso una cella microfluidica integrata. L'applicazione di questo fenomeno plasmonico ha portato all'individuazione di una configurazione promettente per una nuova classe di sensori a base plasmonica compatti e innovativi. I differenti approcci, modellistico – numerico – sperimentale, con cui il problema e' stato affrontato, hanno fornito un'analisi completa della fisica della risonanza plasmonica di superficie con reticoli metallici e delle sue innovative applicazioni per dispositivi sensoristici avanzati.

Summary

Preface

Plasmonics is the study and application of the interactions of optical-frequency electromagnetic waves with electrons in metals. One key advantage of plasmonic devices is that they provide the possibility to confine and exploit electromagnetic oscillations at optical frequencies to a size that is much smaller that the wavelength in vacuum. This is useful for creating intense and concentrated electromagnetic fields that can be used as extremely sensitive probes for spectroscopy or in order to enhance light interaction with matter in any application which requires it. In last decades Plasmonics has known an increasing interest in a growing range of scientific fields and its advances and progress have offered promising ideas for applications in many areas: sensing, solar cells, optoelectronics and communication. The possibility to exploit material properties at the nanoscale and to control light interaction with matter revealed new unexpected phenomena and opened the route to new research-threads in many disciplines: physics, material science and information engineering, biotechnology, biochemistry and medicine. In this way Plasmonics has increasingly become a cross-disciplinary research field, where contributions of different backgrounds, engineering and physics as well as biology and chemistry, is needed in order to provide the required know-how so to design and realize such plasmonic devices.

Advances in nanotechnology in last decades provide the needed instrumentation and facilities for the manipulation and control of matter at the nanoscale. However a preliminary study of design and analysis in necessary in order to optimize the optical response of such nanostructures and provide to nanofabrication the proper windows of process for the realization of optimized devices. Once the components have been fabricated and assembled, a characterization step is performed to verify the real optical behaviour and compare results with the theoretical expectations. Thus the realization of a plasmonic device should consider and overcome each step of this chain of processes: simulation – fabrication – characterization. This is a sort of technological translation of the galileian scientific method that moves from hypothesis and verification to the comparison of experimental data with the formulated theory which results either reinforced or corrected.

This thesis deals with the design and realization of plasmonic gratings for sensing applications and is the result of an interdisciplinary work of three years on plasmonics. Both a theoretical analysis of the problem and an experimental activity of fabrication and characterization have been required, as well as the intergration of the physics background with the acquisition of material science and engineering expertise.

Plasmonic gratings are nanostructured metallic surface that support the excitation and propagation of Surface Plasmon Polaritons (SPPs). These modes are localized surface-waves propagating along the interface between a metal and a dielectric medium and have rise in the coupling of electromagnetic-field with electron-plasma oscillations inside the metal. Thanks to the great confinement of the electromagnetic energy at the nanoscale on the surface, these modes are extremely sensitive to interface properties and reveal themselves as a powerful probe for surface analysis and sensing applications. The change in refractive index of the medium, for example due to a change in concentration of an analyzed solution, or to the binding of molecules to the metal surface, alters the propagation constant of surface plasmon polaritons and changes the coupling conditions of incident light. In this way a variation in resonance conditions can be transduced into a measure of surface functionalization or solution concentration: this is the basic principle of moderm Surface Plasmon Resonance (SPR) sensors.

Since its first demonstration for the study of processes at the surfaces of metals and sensing of gases in the early 1980s, SPR sensing has made vast advances in terms of both development of technology and its applications for label-free fast and compact sensors. In particular the application for detection of chemical and biological species has gained considerable importance and interest in several fields: medical diagnostics, environmental monitoring, food safe and security. Common SPR affinity biosensors consist of a biorecognition element that is able to interact with a particular selected analyte in solution and an SPR transducer, which translates the binding event into an output signal. The core of the transducer is the optical platform, such as a metallic grating, on which surface plasmon polaritons are optically excited and propagate.

In this work an analysis of surface plasmon polaritons excitation and propagation on metallic gratings has been carried out with the use of physical models and numerical analysis. A numerical algorithm has been implemented in order to rigorously compute the grating optical behaviour and to select the proper geometry and materials that optimize grating response for sensing purposes. The rigorous approach of numerical simulation provides a complete and reliable analysis of the electromagnetic field and allows also computing the plasmonic field on the metal surface. This considerable result offers a near-field point of view of the phenomenology which far-field experimental techniques cannot give otherwise, and exhibits one of the most remarkable skills that simulation codes can perform. Moreover simulation results have been compared with the real optical response of fabricated metallic gratings and a successful matching of theoretical and experimental data is shown. The fabricated gratings have been realized by interferential lithography technique, a fabrication process that provides periodic pattern with great coherence over large areas. The metal deposition on such patterned samples promotes the modulated surface to a metallic grating. Several characterization techniques have been employed for quality-check and otpical analysis of the samples: scansion electron and atomic force microscopy (SEM-AFM), spectroscopic ellipsometry, reflectivity analysis. The suitability of these grating supports for sensing has been tested and proved with surface functionalization and with the flowing of solutions into a microfluidic cell embodied to the samples. Functionalization with self-assembling monolayer of simple molecules such as alkanethiols and organic polymers has been done in solution and the optical response after the process has been compared with the response of a bare sample. Differences in the optical spectra are a clear evidence of grating sensitivity and can give information, once the system has been properly calibrated or modelized, either on the coating layer or on the analyte-concentration flowing into the cell.

One of the most important result of this thesis work is the explanation and demonstration of the sensitivity enhancement with an azimuthal rotation of the grating support. If a grating is azimuthally rotated, more SPPs can be supported with the same illuminating wavelength and a refractive index sensitivity al least one order of magnitude greater than that in a

conventional configuration with null azimuth can be provided. Moreover the symmetry breaking with grating rotation makes incidence polarization have a fundamental role on surface plasmon polaritons excitation: *p*-polarization is no longer the most effective, as stated in literature, but polarization must be tuned to a different value in order to optimize the coupling. The optimal value is strictly dependent on the azimuth value and on the resonance conditions, that change after a functionalization of the grating surface. This important result suggests the use of polarization as a parameter for sensing and provide the possibility to realize more compact, fast and cheap grating-coupled SPR sensors based on polarization modulation. The experimental demonstration with a polarization-scan analysis before and after the functionalization of a properly rotated grating, clearly shows the promising and competitive performances of this technique.

In addition, the study of a nanoporous metallic substrate has been done. Thanks to the concomitance of plasmonic properties and an enhanced surface-to-volume ratio, a grating in nanoporous gold guarantees an improved sensitivity to surface functionalization. Nanoporous gold properties have been studied with several characterization techniques and a periodic modulation has been patterned on by focused-ion-beam lithography. Moreover, by acting on specific parameters during the fabrication process, it is possibile to control porosity nanostructure and thus tune the optical and plasmonic features of this material.

In summary, the content of this thesis work is organized as it follows:

Chapter 1: Plasmonics on metallic gratings. A brief introduction to surface plasmon polaritons properties is given, e.g. propagation and extinction lengths, dispersion relation, transverse-magnetic nature. A description of the commonly employed metals is provided and the typical configurations (prism/grating-coupling) for surface plasmon polaritons excitation are described. More details on calculations are postponed in appendices A and B. The chapter ends with a summary of surface plasmon resonance sensors: the most important characteristic of an SPR sensor are described and last advances are reported.

Chapter 2: Vectorial model. The phenomenology of surface plasmon polaritons excitation on metallic gratings is analysed and explained through the use of the vectorial model. This simple approach, based on the momentum-conservation law at resonance condition, provides a useful tool in order to understand surface plasmon dependence on the incidence parameters, such as wavelength, azimuth and polar angles. Polarization role on SPP excitation in the conical mounting is tackled and vectorial model allows to give an heuristic explanation of this phenomenon. Moreover, the model provides an analytical formulation of the optimal polarization angle that well fits experimental data.

Chapter 3: Chandezon's method. Limitations of the vectorial model impose the necessity of a more rigorous approach to metallic gratings. Chandezon's method provides an efficient algorithm to exactly solve the problem of a monochromatic plane-wave incident on a patterned surface. The algorithm has been implemented in MATLAB environment and simulation codes have been used to compute the reflectivity of multi-layered stacks with a sinusoidal profile. The usefulness of the code for grating design has been shown through a procedure of profile optimization of a sinusoidal bimetallic grating. Therefore the simulated optical response of a multilayered metallic grating has been successfully compared with experimental data of reflectivity analysis on the fabricated model. In last section, the results of the near-field computation of the plasmonic modes propagating on the grating surface are shown and discussed.

Chapter 4: Experimental: nanofabrication and characterization. This part is dedicated to the modern techniques and instruments for the fabrication and characterization of plasmonic gratings. Interferential lithography process and soft-lithography technique for grating-replica production are explained, with experimental pictures and results from the characterization measurements performed during this thesis work. With soft-lithography technique a microfluidic cell has been realized and the system has been embodied to a grating for a calibration test with water-solutions of sodium-chloride flowing through the cell: reflectivity meaurements for increasing sodium-chloride concentrations are reported. Functionalization processes with self-assembling monolayer of alkanethiols and polyethilenoxide are described.

In last sections, the nanofabrication and characterization of nanoporous gold substrates is presented. Physical and optical properties of nanoporous gold samples fabricated in different experimental conditions are reported and discussed. In particular, the analysis highlighs the plasmonic properties of this material.

Chapter 5: Improving the performance of Grating-Coupled SPR. The consequences of symmetry breaking with azimuthal rotation, experimentally shown and theoretically described in chapters 2 and 3, are here exploited in order to enhance surface plasmon resonance sensitivity. The phenomenon of sensitivity enhancement with increasing azimuth is explained and experimental results are presented that demonstrate and confirm this improvement. An analysis of sensitivity dependence on azimuth is performed by functionalizating grating surface with dodecanethiol (C12) or polyethileonxide (PEO) self-assembling monolayer and with sodium-chloride solution flowing through the embodied cell. The combination of azimuthal rotation and enhanced sensitive surface, provides a further sensitivity enhancement with the choice of a nanoporous-gold sensing platform. The idea of a new grating-coupled surface plasmon resonance analysis based on polarization modulation is proposed and described. The performance of this technique is experimentally tested on a C12-functionalization and results confirm the possibility to use the phase term of the polarization scan as a parameter for high-resolution sensing. Moreover this result improves SPR technology with the possibility to realize a new generation of more compact, fast and economic grating-based sensors.

31 January 2012, Padova

Gianluca Ruffato

In memory of Alessandro

1 Plasmonics on metallic gratings

1.1 Introduction

Surface Plasmon Polaritons (SPPs) are electromagnetic waves propagating along the interface between a metal and a dielectric medium and have origin from the coupling of the electromagnetic field with electron-plasma density oscillations inside the metal. SPPs are localized solutions of Maxwell's equations: field intensity decays exponentially from the surface with an extension length of the same order of the wavelength inside the dielectric and almost one order shorter in the metal[1]. These features make SPPs extremely sensitive to the optical and geometrical features of the supporting interface, such as shape, roughness and refractive indices of the facing media.

Since these modes have a non-radiative nature, the excitation with a wave illuminating the metallic surface is possible only in such proper configurations that provide the wavevector-matching between the incident light and SPP dispersion law (Surface Plasmon Resonance - SPR). A solution is to couple a prism to the metal in order to properly increase incident light momentum and achieve SPP excitation (Kretschmann-Raether configuration), however this system suffers from cumbersome prism presence and alignment. A more amenable and cheaper solution consists in Grating-Coupling SPR (GCSPR), where the metal surface is modulated with a periodic corrugation.

Actually grating-coupling has been the first method in order to exploit surface plasmon resonance: the plasmonic behaviour of such modulated metallic surfaces had been discovered since the early years of the last century by R.W. Wood[2] who observed an anomalous lowering in light reflected by metallic gratings illuminated under certain conditions. Fano has proven that these anomalies are associated with the excitation of electromagnetic surface waves on the surface of the diffraction gratings[3]. In 1968 Otto[4] and Kretschmann[5] independently demonstrated that the drop in reflectivity in the attenuated total reflection (ATR) method is due to surface plasmon excitation. The physical explanation of this phenomenon and the connection between Wood's anomalies and surface plasmons was finally established by J.J. Cowan and E.T. Arakawa[6]: a plane-wave illuminating the patterned area is diffracted by the

periodic structure and it is possible for at least one of the diffracted orders to couple with SPP modes.

Because of the peculiar capability of harvesting light and confine it to the surface, surface plasmon resonance has known an increasing interest in the design and realization of miniaturized devices based on plasmonic platforms for sensing purposes. Surface plasmon modes in fact are extremely sensitive to changes in the refractive index of the facing dielectric medium: a thin coating film or the flowing of a liquid solution alter SPP dispersion curve and cause resonance conditions to change. Thus it is possible to detect refractive index variations by simply analyzing resonance shift: it is the basis of modern SPR-sensing devices. The strong compatibility of gratings with mass production makes these SPP couplers extremely attractive for fabrication of low-cost SPR platforms for applications in a wide range of fields: bio- and chemical sensing [7,8], medical diagnostics[9], environmental analysis[10], food safety and security[11].

1.2 Surface Plasmon Polaritons

If a plane interface between two semi-infinite media with dielectric permettivity ε_A and ε_B is considered and we look for localized solutions of Maxwell's equation that propagate along the surface, boundary conditions for EM-fields[12] impose specific prescriptions on materials and the resulting propagating modes, the so called Surface Plasmon Polaritons (SPPs) exhibit peculiar features (see Appendix A).

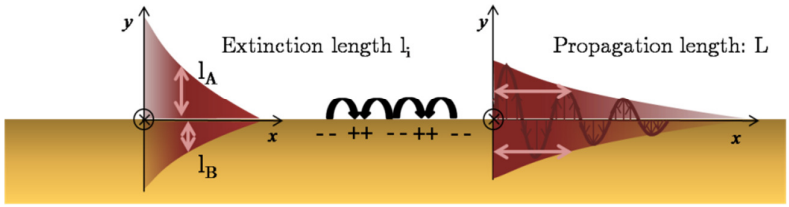

Figure 1-1: Pictorial description of SPPs propagation along a metal-dielectric interface. Extinction of the electromagnetic field along the propation direction and exponential decay from the interface inside each medium.

The two media in fact have to exhibit permittivities with opposite signs at the considered wavelength:

$$\varepsilon_A \cdot \varepsilon_B < 0 \tag{1.2.1}$$

i.e. if the former medium has a positive dielectric permettivity $\varepsilon_A \geq 0$ (dielectric), the latter one have to necessarily show $\varepsilon_B < 0$ (metal). Thus Surface Plasmon Polaritons are supported by the interface between a metal and a dielectric medium and exhibit the following characteristics (see Figure 1-1 and Appendix A):

- SPP are Transverse-Magnetic (TM) modes: the magnetic field is parallel to the interface and perpendicular to the propagation direction. Transverse Electric (TE) modes are not supported by this configuration.
- SPP wavevector k_{SPP} is given by:

$$k_{SPP} = \frac{2\pi}{\lambda}\sqrt{\frac{\varepsilon_A\varepsilon_1}{\varepsilon_A+\varepsilon_1}} + i\frac{2\pi}{\lambda}\left(\frac{\varepsilon_A\varepsilon_1}{\varepsilon_A+\varepsilon_1}\right)^{\frac{3}{2}}\frac{\varepsilon_2}{2\varepsilon_1^2} \tag{1.2.2}$$

  where $\varepsilon_A > 0$ (dielectric), $\varepsilon_1\left(< 0\right)$ and ε_2 are respectively the real and imaginary parts of the permettivity ε_B in the metallic medium, λ is the considered wavelength. It is worth noting that $\Im\left[k_{SPP}\right] \propto \varepsilon_2$, i.e. SPP dissipation is strictly related to the adsorption contributions inside the metal. The traveling SPPs are damped with a propagation length $L_{SPP} = \left(2\Im\left[k_{SPP}\right]\right)^{-1}$, tipically between 10 and 100 mm in the visible range, depending on the configuration.
- EM-field intensity decays exponentially in direction normal to the surface with decay lengths l_A and l_B inside the two media:

$$l_A = \frac{\lambda}{2\pi}\sqrt{-\frac{\varepsilon_A+\varepsilon_1}{\varepsilon_A^2}} \tag{1.2.3}$$

$$l_B = \frac{\lambda}{2\pi}\sqrt{-\frac{\varepsilon_A+\varepsilon_1}{\varepsilon_1^2}} \tag{1.2.4}$$

Thus the SPP field falls off exponentially in the normal direction with a characteristic length in the order of the exciting wavelength into the diectric medium and about one order shorter inside the metal.

Therefore Surface Plasmon Polaritons are localized solutions of Maxwell's equations, propagating along the surface between a dielectric medium and a metal. In order to analyze SPP dispersion curve and the excitation of these modes on a metallic surface, an analytical description of the dielectric permettivity of the metal is necessary. As it will be explained in the following section, a free-electron gas approach is a good approximation to describe in the visible range the optical response of the metals of interest for plasmonic applications.

1.3 Metals - Drude model

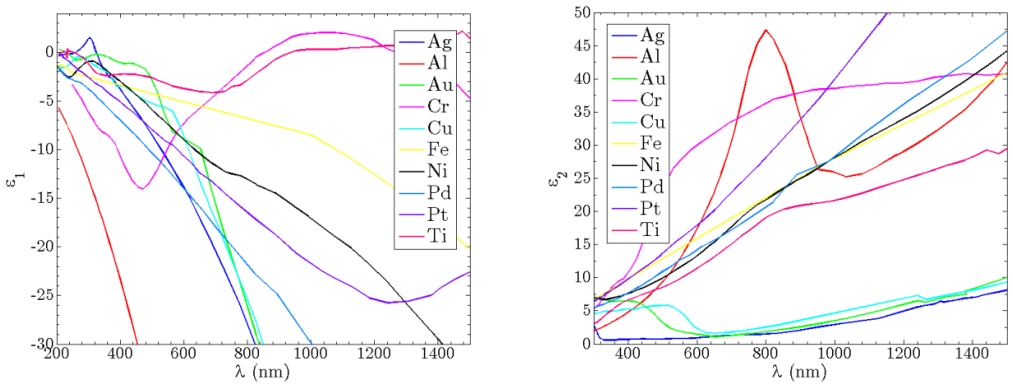

Figure 1-2: dielectric permettivity real ε_1 and imaginary ε_2 parts for common metals: silver (Ag), aluminum (Al), gold (Au), chromium (Cr), copper (Cu), iron (Fe), nickel (Ni), palladium (Pd), platinum (Pt), titanium (Ti).

In Figure 1-2 dielectric permettivity real ε_1 and imaginary ε_2 parts are showed in the range $200 - 1500\,\text{nm}$ for the most common metals[13]. Most of metals exhibit a common trend in the VIS-*near*IR spectral range: ε_1 decreases for increasing wavelength and is negative in the VIS-IR range, while ε_2 increases with wavelength.

Over a wide frequency range, the optical properties of metals can be explained by a plasma model, where a gas of free electrons of number density N moves against a fixed background of positive ion cores (*Drude model* [14]). In this model, details of the lattice potential and electron-electron interactions are not taken into account. The electrons oscillate

in response to an applied electromagnetic field and their motion is damped via collisions occurring with a characteristic collision frequency $\gamma = 1/\tau$, where τ is known as the relaxation time of the free electron gas, typically in the order of 10^{-14}-10^{-15} s at room temperature. This model provides the following expression for the dielectric permettivity as a function of the frequency ω (see Appendix B):

$$\varepsilon(\omega) = 1 - \frac{\omega_p^2}{\omega^2 + i\omega\gamma} \tag{1.3.1}$$

Thus the real and imaginary parts are given by:

$$\varepsilon_1(\omega) = 1 - \frac{\omega_p^2\tau^2}{1+\omega^2\tau^2} \tag{1.3.2}$$

$$\varepsilon_2(\omega) = \frac{\omega_p^2\tau}{\omega(1+\omega^2\tau^2)} \tag{1.3.3}$$

where ω_p, the so called *Plasma Frequency*, is given by:

$$\omega_p = \sqrt{\frac{Ne^2}{m\varepsilon_0}} \tag{1.3.4}$$

where ε_0 is vacuum permettivity, m and e are respectively electron mass and charge. As we saw in previous section, the imaginary part of SPP wavevector is proportional to the adsorption contribution of metal dielectric permettivity (see eq. (1.2.2)), thus it is not only necessary that the material exhbits a metallic behaviour $(\varepsilon_1 < 0)$, but it should be also appreciable to reduce dissipation sources. As Figure 1-2 shows, the lowest adsorption in the visible range is exhibited by the three noble metals: Copper (Cu), Silver (Ag) and Gold (Au). In Table 1-1 Drude parameter for noble metals are collected. The free-electron response of these metals is quite similar, since they hold the same electronic structure in the outer shells, $(n-1)d^{10}ns^1$, and the same lattice structure (Face Centered Cubic - FCC) with almost comparable interatomic distances: 132 (Cu), 145 (Ag), 136 (Au) pm.

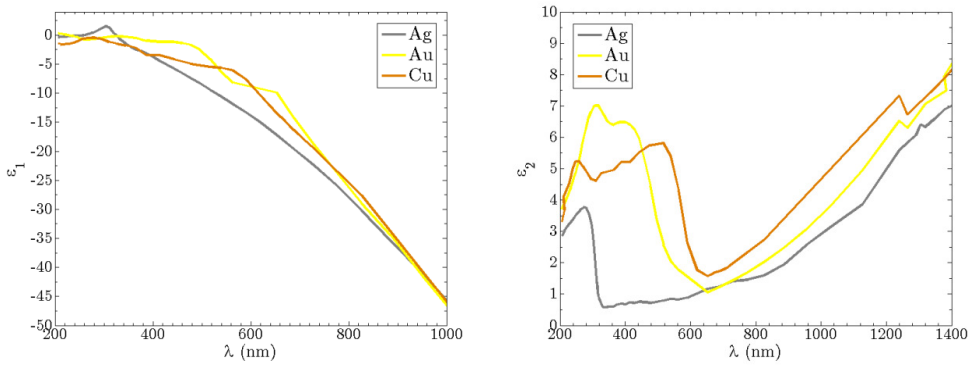

Figure 1-3: dielectric permettivity real ε_1 and imaginary ε_2 parts of noble metals Cu, Ag, Au.

Table 1-1: Drude parameters of noble metals.

	$\omega_p(eV)$	$\tau(10^{-15}s)$	$N(10^{21}cm^{-3})$
Copper - *Cu*	9.31	12	60.0
Silver - *Ag*	9.02	16	58.6
Gold - *Au*	8.36	10	50.8

At lower wavelengths (higher frequencies) in the near-UV, permettivity values for real metals markedly diverges from Drude's model. For noble metals, an extention to this model is needed in the region $\omega > \omega_p$, where the response is dominated by free s electrons, since the filled d band close to the Fermi surface causes a highly polarized environment. This residual polarization due to the positive background of the ion cores can be described by adding a constant contribution ε_∞ (usually $1 \le \varepsilon_\infty \le 10$). Moreover, the applicability of the free-electron model breaks down due to the occurrence of interband transitions of sp electrons to the conduction band, leading to an increase of ε_2 in the nearUV-VIS range. These adsorption contribution can be taken into account and described in the permettivity function in the form of Lorentz-oscillator terms, centered at a resonance frequency ω_i and with a band-width $\omega_{\tau,i}$, amplitude A_i. After these considerations, a more realistic model for the dielectric permettivity of a real metal is given by:

$$\varepsilon(\omega) = \varepsilon_\infty - \sum_i \frac{A_i}{\omega^2 - \omega_i^2 + i\omega_{\tau,i}\omega} - \frac{\omega_p^2}{\omega^2 + i\omega\gamma} \tag{1.3.5}$$

Because of the absence of interband transitions in the visible range (see Figure 1-3), silver seems to be the best choice for the realization of plasmonic supports for the excitation and propagation of surface plasmon polaritons, however this metal is exposed to oxidation in air and the surface gets coated by a layer of silver oxide which affects SPP propagation and silver affinity. On the other hand, gold exhibits a peculiar chemical stability in air, but the strong interband transitions up to $\sim 550\,\text{nm}$ affects the optical response in the nearUV-VIS range. As regards copper, it exhibits a strong adsorption in the near-UV and is exposed to oxidation in air as well.

Thus the best choice seems to be a silver substrate coated by a thin layer of gold in order to prevent silver oxidation in air.

1.4 Excitation of Surface Plasmon Polaritons

Figure 1-4 shows the dispersion curve $\left(\omega, k\right)$ for surface plasmon polaritons propagating on a silver surface in air, calculated using equation (1.2.2) for k_{SPP} and tabulated values for silver permettivity (Palik). In the same picture, the dispersion relation for a plane wave in air is reported (*light line*).

It is worth noting that SPP dispersion curve lies totally on the right of the light line and no intersection takes place. Thus propagating surface plasmons have a non-radiative nature: once these modes are excited, coupled energy propagates along the interface as far as it is dissipated by metal adsorptions. On the other hand, the non-radiative nature of SPPs implies that excitation by a direct illumination of the metal surface is not possible and propagating surface plasmons can be excited only in such proper configurations that provide the momentum-matching between incident light and surface modes[15]. Two alternative configurations are possible:

- *Prism-Coupled Surface Plasmon Resonance* (PCSPR)
- *Grating-Coupled Surface Plasmon Resonance* (GCSPR).

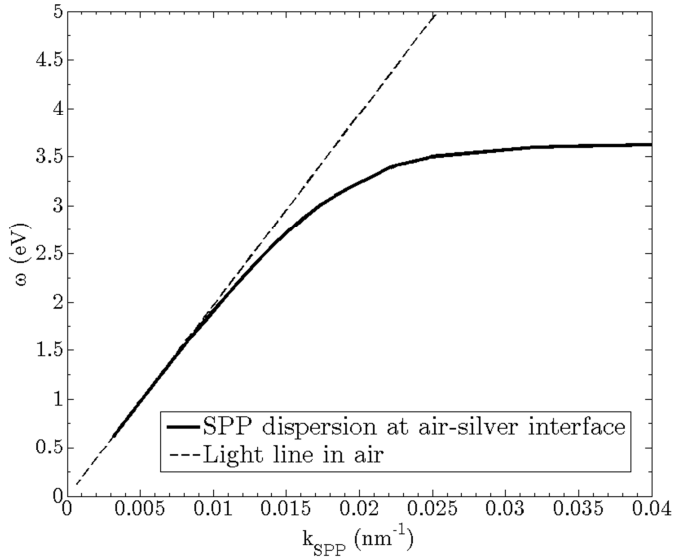

Figure 1-4: SPP dispersion curve on the interface between silver and air (solid line). Comparison with dispersion curve of light in air (dashed line).

1.4.1 Prism-Coupled Surface Plasmon Resonance

Introduced for the first time by the prioneerig works of Otto and Kretschmann in 1968, prism-coupling configuration provides SPP excitation in the attenuated total reflection (ATR) method. In this configuration a prism is exploited in order to increase incident light momentum and achieve the momentum-matching condition. This technique consists in giving rise to surface polaritons at the metal-dielectric surface thanks to the passage of the exciting wave through a medium with a refractive index n_p greater than the dielectric one. In this way photons gain the momentum-gap which is necessary for the matching of the light line with the SPP dispersion law and the incident electromagnetic wave couples with surface electron excitations:

$$\Re\left[k_{SPP}\right] = \frac{2\pi}{\lambda} n_p \sin\theta \tag{1.4.1}$$

where θ is the incidence angle. In the simplest configuration, three different layers are employed: a prism to increase photon momentum and the metal-dielectric sequence. Two setups are possible: *Otto's configuration* and *Kretschmann-Raether's configuration* [16]. In the former the dielectric medium is sandwiched between the prism and the metal at a distance of about λ. The evanescent field couples with SPP modes at the dielectric-metal interface. In

the latter setup instead, the metal layer is placed in the middle: the electromagnetic field decreases esponentially in the film and excites SPPs at the interface between metal and dielectric medium (Figure 1-5).

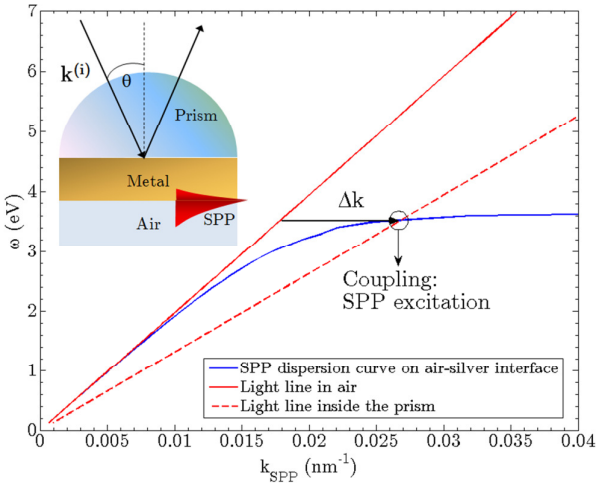

Figure 1-5: Prism-coupling mechanism. In the inset graph: Kretschmann's configuration.

1.4.2 Grating-Coupled Surface Plasmon Resonance

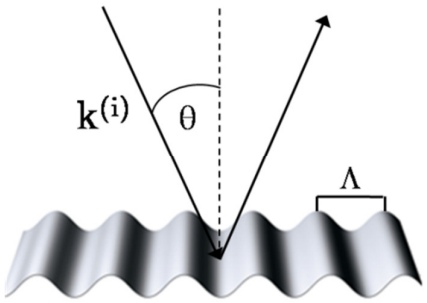

Figure 1-6: Grating coupling mechanism

An alternative solution in order to optically excite surface plasmons polaritons is based on the diffraction of light incident on a metallic grating. Incident light momentum $\boldsymbol{k}^{(in)}$ couples to grating crystal momentum $\boldsymbol{G}$, whose modulus is given by:

$$G = \frac{2\pi}{\Lambda} \tag{1.4.2}$$

where Λ is the grating period. Each diffracted order holds a momentum $\boldsymbol{k}^{(n)}$ given by:

$$\boldsymbol{k}^{(n)} = \boldsymbol{k}^{(i)} + n \cdot \boldsymbol{G} \tag{1.4.3}$$

where n is the diffraction order. Thus surface plasmon polaritons excitation takes place when the on-plane momentum component of a particular diffracted order equals SPP momentum $\boldsymbol{k}_{SPP}$:

$$\Re\left[\boldsymbol{k}_{SPP}\right] = \boldsymbol{k}_{\parallel}^{(i)} + n \cdot \boldsymbol{G} \tag{1.4.4}$$

In the classical mounting, where the scattering plane is parallel to the grating symmetry plane, i.e. $\boldsymbol{k}_{\parallel}^{(i)} \parallel \boldsymbol{G}$, the previous relation implies the following resonance equation:

$$\Re\left[k_{SPP}\right] = \frac{2\pi}{\lambda} n_i \sin\theta + n\frac{2\pi}{\Lambda} \tag{1.4.5}$$

where λ is the illuminating wavelength, θ is the incidence polar angle and n_i is the refractive index of the dielectric medium facing the grating surface. This vectorial description of surface plasmon resonance in terms of grating momentum, only provides information about coupling conditions such as resonance wavelength and angle for a given grating period and stack. Further details about coupling strength, i.e. weights of the diffracted orders, are not provided by this approach and a more accurate analysis, such as a numerical solution of grating diffraction problem, is recommended (see Chapter 3).

1.5 Plasmonics for sensing devices

In principle, SPR sensors measure changes in the refractive index occuring at the surface of a metal film supporting propagating surface plasmons[17]. A surface plasmon excited by an incident wave, propagates along the metal surface and its evanescent field probes the medium in contact with the metal film. As eq. (1.2.2) shows, surface plasmon momentum is strictly dependent on the refractive index n of the dielectric medium:

$$\Re\left[k_{SPP}\right] = \frac{2\pi}{\lambda}\sqrt{\frac{n^2\varepsilon_M}{n^2 + \varepsilon_M}} \tag{1.5.1}$$

where λ is the illuminating wavelength, ε_M is the dielectric permettivity of the metal. Either a change in the refractive index n of the facing dielectric or the coating of the metal surface with a thin film, gives rise to a change of the propagation constant k_{SPP} of surface plasmon modes and thus alter coupling conditions of the incident light, such as resonance angle or wavelength, coupling intensity and phase. On the basis of which characteristic of the light modulated by a surface plasmon is measured, SPR sensors are classified as sensors with *angular, wavelength, intensity* or *phase modulation* [18].

In SPR sensors with angular modulation, a monochromatic light wave is used to excide SPPs and the strength of coupling between the incident wave and surface plasmons is observed at multiple angles of incidence: SPP excitation is observed as a dip in the angular spectrum of reflected light. The angle of incidence yielding the strongest coupling (reflectivity minimum) is measured and used as sensor output[19]. In wavelength modulation SPR instead, surface plasmons are excited by a beam of polychromatic light and the excitation is observed as a dip in the wavelength spectrum of reflected light: the wavelength yielding the strongest coupling corresponds to sensor output[20]. In SPR sensors with intensity modulation the strength of the coupling between the light wave and surface plasmons is measured at a single angle of incidence and wavelength and the intensity of light serves as sensor output[21]. In phase modulation SPR, the shift in phase of reflected light is measured at a single angle of incidence and wavelength of the light wave and used as sensor output[22].

SPR affinity biosensor consists of a biorecognition element that is able to interact with a particular selected analyte and an SPR transducer, which translates the binding event into an output signal. The core of the transducer is the optical platform on which a surface plasmon is optically excited and propagates, e.g. a modulated metallic grating or a flat Kretschmann's stack. The biorecognition element is fixed in the proximity of the surface of the metal film supporting SPP modes and it recognizes and is able to interact with a selected analyte. Analyte molecules in a liquid sample in contact with the SPR sensor bind to the biorecognition elements, producing an increase in the refractive index at the sensor surface which is optically measured by SPP excitation and translated into an output signal. The

sensor response Y to a given value X of the measurand can be predicted by the sensor transfer function T, $Y = T(X)$ determined from a theoretical model of sensor response or from a sensor calibration. Some of the most important characteristics of SPR sensor performance are: *sensitivity, linearity, resolution, accuracy, limit of detection (LOD).*

1.5.1 SPR sensitivity

Sensor sensitivity S is the ratio of the change in sensor output Y to the change in the measurand X, i.e. the slope in the calibration curve:

$$S = \frac{\partial Y}{\partial X} \tag{1.5.2}$$

Refractometric sensitivity S_n is a measure of the sensitivity of the SPR sensor to a change of the dielectric refractive index n and is given by:

$$S_n = \frac{\partial Y}{\partial n} \tag{1.5.3}$$

An interest quantity for solution analysis is the sensitivity S_c of a SPR biosensor to the concentration c of an analyte in the solution:

$$S_c = \frac{\partial Y}{\partial c} = \frac{\partial Y}{\partial n}\frac{\partial n}{\partial c} = S_n \frac{\partial n}{\partial c} \tag{1.5.4}$$

where $\partial n / \partial c$ is the refractive index change due to the analyte presence in the solvent.

If instead the metal surface is coated with a biorecognition layer which is sensitivive and bind to a particular type of analytes in the analyzed solution, the concentration sensitivity S_c can be expressed as:

$$S_c = \frac{\partial Y}{\partial n_{eff}}\frac{\partial n_{eff}}{\partial n_l}\frac{\partial n_l}{\partial c} = S_{n,eff}\frac{\partial n_{eff}}{\partial n_l}\frac{\partial n_l}{\partial c} \tag{1.5.5}$$

where $S_{n,eff}$ denotes the sensitivity to a refractive index profile change (it is equivalent to S_n), $\partial n_{eff} / \partial n_l$ describes the variation of the effective refractive index due to a change in the refractive index n_l of binding layer, $\partial n_l / \partial c$ expresses the refractive index change in the

layer due to the analyte concentration in the solution. The first term $S_{n,eff}$ depends on the method of excitation of surface plasmons and on the modulation approach and it is referred as to an instrumental contribution, whereas the second term expresses the sensitivity of a surface plasmon to refractive index and is independent of the modulation method and the method of excitation of SPP: it mainly depends on the profile of the refractive index and of the SPP probing field (see section 4.5.1).

1.5.2 Linearity

Sensor linearity defines the extent to which the relationship between the measurand and the sensor output is linear over the working range. Linearity is usually specified in terms of the maximum deviation from a linear transfer function over the specified dynamic range. Sensors with linear transfer function are desirable as they require fewer calibration points to produce an accurate sensor calibration. However, response of SPR biosensors is usually a non-linear function of the analyte concentration and therefore calibration needs to be carefully considered.

1.5.3 Resolution and accuracy

The resolution of a SPR biosensor is defined as the smallest change in the bulk refractive index that produces a detectable change in the sensor output and it is strictly related to the level of uncertainty of the sensor output: the sensor noise. The refractive index resolution σ_n is typically expressed in terms of the standard deviation of noise of the sensor output σ_Y translated to the refractive index of bulk medium:

$$\sigma_n = \frac{\sigma_Y}{S_n} \tag{1.5.6}$$

where S_n is the refractive index sensitivity. Dominant sources of noise are the fluctuations in the light intensity emitted by the light source, shot noise associated with photon statistics, noise in conversion of light intensity into electric signal by the detector[23]. Noise in the intensity of light emitted by the light source is proportional to the intensity and

its standard deviation σ_L can be given as $\sigma_L = \sigma_L^r I$ where σ_L^r is the relative standard deviation and I is the measured light intensity. Shot noise is associated with random arrival of photons on a detector and corresponding random production of photoelectrons. Photon flux usually obeys Poisson statistics and produces a shot noise σ_S directly proportional to the square root of the detected light intensity: $\sigma_S = \sigma_S^r \sqrt{I}$, where σ_S^r is a relative standard deviation. Detector noise consists of several contributions that originate mostly in temperature noise and its standard deviation σ_D is independent on light intensity. The resulting noise of a measured light intensity σ_I is a statistical superposition of all the noise components and is given by:

$$\sigma_I\left(I\right) = \sqrt{I^2\sigma_L^{r2} + I\sigma_S^{r2} + \sigma_D^2} \tag{1.5.7}$$

To reduce the noise, light intensity is averaged: time averaging involves the average of time series of intensity from the same detector, spatial averaging instead the average of the output of multiple detectors. As in the time domain all the noise contributions behave independently, the time averaging of N spectra reduces the total noise as follows:

$$\sigma_I^N = \frac{\sigma_I}{\sqrt{N}} \tag{1.5.8}$$

The noise in the light intensity is translated to sensor output noise by the data processing algorithm that is used to generate the sensor output. Although various methods for processing data from spectroscopic SPR sensors have been developed (centroid method[24], polynomial fitting[25], optimal linear analysis[26]), the noise in angular or wavelength spectra was found to transform to the noise in the sensor output in a similar fashion. Centroid method uses a simple algorithm which finds the geometric center of the SPR dip under a certain threshold. The centroid position x_c is calculated as follows using a weigth centroid algorithm[27]:

$$x_c = \frac{\sum_i x_i \left(I_T - I_i\right)^2}{\sum_i \left(I_T - I_i\right)^2} \tag{1.5.9}$$

where x_i is the spectral position of the contributing intensity I_i and I_T denotes the threshold value. If the noise of each intensity value can be detected and treated as independent, the resulting standard deviation of calculated dip position σ_c can be calculated from eq. (1.5.9):

$$\sigma_c^2 = \sum_i \left(\frac{\partial x_c}{\partial I_i} \right)^2 \sigma_i^2 \tag{1.5.10}$$

As demonstrated by Piliarik and Homola[23], if a lorentzian profile is assumed for the portion of the SPR dip that is used for the centroid estimation, the following expression for resolution is given:

$$\sigma_n = K \frac{1}{\sqrt{N}} \frac{\sigma_T}{d} \frac{w}{S_n} \tag{1.5.11}$$

where N is the number of points used for the calculation of the centroid, σ_T is the total intensity noise at the threshold, d is the difference of intensities between SPR minimum and the threshold value, w is the width of the resonance dip, S_n is the refractive index sensitivity of the device and K is a factor depending on the relative contribution of the different sources of noise[23], e.g. $K_1 = 0.5$ for additive noise, $K_2 = 0.43$ for shoit noise, $K_3 = 0.38$ for intensity noise, thus $K^2 = g_1^2 K_1^2 + g_2^2 K_2^2 + g_3^2 K_3^2$, where g_i indicate the weights of each noise source.

This results shows that resolution strictly depends on resonance profile and, as expected, output noise. From eq. (1.5.11) resolution is proportional to output noise σ and resonance width w, whereas it decreases with increasing sensor sensitivity S_n and depth of resonance dip d. The ratio w / S_n depends only weakly on the choice of coupler and modulation and therefore has only a minor effect on the sensor resolution. As a consequence of eq. (1.5.11), it is worth noting that resonance-dip width w should be minimized while depth d should be maximized in order to optimize the refractive index resolution σ_n.

1.5.4 Limit of detection

Limit Of Detection (LOD) is the concentration of analyte c_L derived from the smallest measure Y_L that can be detected with resonable certaintly and it is given by:

$$Y_L = Y_b + m \cdot \sigma_b \tag{1.5.12}$$

where Y_b is an estimation of blank (without analyte) sample output, σ_b is the standard deviation of the blank measure, m is a numerical factor chosen according to the desired confidence level (typically 2.5-3 [28]). If $c_b = 0$, the LOD concentration c_L is given by:

$$c_L = \frac{m \cdot \sigma_b}{S_c} \tag{1.5.13}$$

1.5.5 Advances in SPR Technology

Currently, several groups are using different approaches to detect the change of refractive index with surface plasmon resonance sensors. Sensors using Prism-Coupled SPR (PCSPR) with Kretschmann configuration can be readily combined with any type of interrogation: angular, wavelength, intensity or phase modulation. Devices based on intensity modulation for sensing puroposes or SPR imaging showed refractive index resolutions down to $6 \cdot 10^{-6}$ RIU (Lechuga's et al.[29]) and $2 \cdot 10^{-6}$ RIU (Homola's group[30]). Sensors based on spectroscopy of Surface Plasmons through angular or wavelength scanning, exhibit better performance in sensitivity and resolution. PCSPR typically show refractive index sensitivity for typical angular interrogation architecture that ranges between $50 - 150^{\circ}/\text{RIU}$[31], with higher sensitivity at shorter wavelengths[32], and refractive index resolutions in the orders $10^{-6} - 10^{-7}$. In the early 1990s, an angular modulation-based SPR sensor consisting of a light-emitting diode (LED), a glass prism and a detector array with imaging optics, was adopted by Biacore and resulted in a family of commercial SPR sensors with resolution down to $1 \cdot 10^{-7}$ RIU. An SPR sensor with wavelength modulation and parallel channel architecture was reported by Homola's group[33] and it was demonstrated to be able to resolve refractive index changes down to $2 \cdot 10^{-7}$ RIU. An improvement of Nenninger's

configuration[34] based on spectroscopy of long-range surface plasmon, demonstrated[35] a resolution as low as $3 \cdot 10^{-8}$ RIU. Nowadays numerous SPR sensors based on spectroscpy of surface plasmons are commercially available. However, PCSPR sensors suffer from cumbersome optical alignment and are not amenable to miniaturization and integration[36].

On the other hand, Grating-Coupled SPR (GCSPR) sensors with either wavelength or angular interrogation have been demonstrated to have sensitivity $2-3$ times lower[37] than PCSPR, however GCSPR eliminates the prism presence and is more suitable to miniaturization. Grating couplers have not been used in SPR sensors as widely as the prism couplers, but their compatibility with mass production and the prism absence, make GCSPR an attractive approach for the fabrication of low-cost compact sensing devices. GCSPR has the intrinsic possibility to be used with different sensing architectures and interrogation systems. A parallel SPR angular detection was shown by Unfrict et al.[38] to have the possibility for multi-detection for proteomic multiarray. Homola's group[39] demonstrated a miniaturized GCSPR sensor implemented with a CCD allowed detection sensitivity of $50°$/RIU and resolution of $5 \cdot 10^{-6}$ over 200 sensing parallel channels. Alleyne[40] has exploited the generation of an optical band gap by using prism-coupled to achieve sensitivity up to $680°$/RIU by bandgap-assisted GCSPR. A recent approach was reported by Telezhnikova and Homola[41] with the development of a sensor based on spectroscopy of SPPs down to $3 \cdot 10^{-7}$ RIU.

1.6 Conclusions

In the light of what exposed in previous sections on surface plasmon polaritons features and their exploitation for sensing devices, we can draw the following conclusions:

- Grating-Coupled is rather preferable than prism-coupling, since it is more suitable to miniaturization and integration. Moreover, by acting on configuration and signal transduction, it is possible to achieve competitive sensitivity and resolution performance.

- A silver layer coated by a thin anti-oxidation gold film seems to be the best combination for realizing a plasmonic substrate with low adsorption and chemical stability.

- Grating profile and materials should be properly chosen and optimized in order to provide the deepest and sharpest resonance dips.

2 Vectorial model

2.1 Introduction

The Vectorial Model provides a simple but effective approach for the study of surface plasmon polaritons excitation and propagation on periodic structures. In this analysis, the grating is modeled as a uniaxial crystal and the periodicity effect is exploited by the crystal momentum $\boldsymbol{G}$, whose modulus is given by $G = 2\pi / \Lambda$, where Λ is the grating period. Incident light momentum couples with grating vector $\boldsymbol{G}$ and surface plasmons are excited if the resonance condition for the on-plane components is satisfied (eq. (1.4.4)).

The equation of momentum-conservation law plays a fundamental role in this approach, since it represents the only available condition in order to describe and analyse the excitation of propagating surface plasmons. By applying this model, information about surface plasmon excitation dependence on incidence angles and wavelength can be obtained, however since further details such as grating profile and shape are not taken into account, this approach reveals a good approximation just for shallow gratings. An analysis of the effects of groove depth and shape on SPP resonance, should require a more complex and rigorous approach.

In this chapter an introduction to SPP excitation on metallic grating is given and the dependence of resonance condition on the incidence wavelength and angles is described through the application of the vectorial model. The comparison with experimental results confirms the applicability of this method for resonance analysis. On the other hand, the necessity of exacly computing the intensity of the several diffracted orders, e.g. reflectivity, and in particular to analyse their dependence on the grating profile, imposes the choice of a numerical solution to the problem which will be considered in the next chapter.

In following sections the results from vectorial model are compared with experimental results from reflectivity characterization of a bimetallic grating. Experimental data refer to a sinusoidal grating with period of 505 nm and amplitude of 25 nm, fabricated by UV interferential lithography in Lloyd's mirror configuration. The fabricated pattern has an almost perfect sinusoidal profile with a local roughness of the order of 1 nm rms. Thereafter a

gold (7nm) /silver (37nm) bi-metallic layer was thermally evaporated (see experimental – chapter 4).

2.2 Momentum-conservation law

If a metallic grating is illuminated with fixed wavelength λ and varying incident polar angle θ, a reflectivity dip appears in correspondence of the incidence angle θ_{res} at which the momentum-conservation law on the grating plane is satisfied:

$$\boldsymbol{k}_{SPP} = \boldsymbol{k}_{\parallel}^{(i)} + n \cdot \boldsymbol{G} \tag{2.2.1}$$

where $\boldsymbol{k}_{SPP} = k_{SPP}\left(\cos\beta, \sin\beta\right)$ is the wavevector of the excited SPP, $\boldsymbol{k}_{\parallel}^{(i)} = 2\pi \,/\, \lambda \cdot \left(\sin\theta_{res}, 0\right)$ is the on-plane component of the incident light wavevector, $\boldsymbol{G} = 2\pi \,/\, \Lambda \cdot \left(\cos\varphi, \sin\varphi\right)$ is the grating momentum, Λ being the grating periodicity.

In the case of shallow grooves, the expression of k_{SPP} valid for flat interfaces is a good approximation (eq. (1.2.2)):

$$k_{SPP} = \frac{2\pi}{\lambda}\sqrt{\frac{\varepsilon_m \varepsilon_D}{\varepsilon_m + \varepsilon_D}} \tag{2.2.2}$$

where ε_m and ε_D are respectively the metal-side and the dielectric-side effective dielectric permittivity. In the considered reference frame, the scattering plane is kept fixed and parallel to the *x*-axis and the grating vector $\boldsymbol{G}$ and the SPP momentum $\boldsymbol{k}_{SPP}$ form respectively angles φ and β with the *x*-axis positive direction (see Figure 2-4). Since the grating period Λ is typically in the order of 500 nm, i.e. lower than the typical incident wavelength in the optical range, in our cases of interest the resonance order is usually $n = -1$, thus eq. (2.2.1) becomes:

$$\boldsymbol{k}_{SPP} = \boldsymbol{k}_{\parallel}^{(i)} - \boldsymbol{G} \tag{2.2.3}$$

In the case of null azimuth $\varphi = 0°$, following expression leads to the scalar relation:

$$\frac{2\pi}{\lambda}\sqrt{\frac{\varepsilon_m \varepsilon_D}{\varepsilon_m + \varepsilon_D}} = \left|\frac{2\pi}{\lambda}\sin\theta_{res} - \frac{2\pi}{\Lambda}\right| \tag{2.2.4}$$

As Figure 2-1 shows, under resonance order $n = -1$, resonance dips shift towards greater angles for increasing wavelength (cfr. Figure 2-2.a). By applying resonance eq. (2.2.4) to resonance angle position, it is possibile to reconstruct the dispersion relation $\omega - k$:

$$\omega\left[eV\right] = \frac{1240}{\lambda\left[nm\right]}$$
$$k\left[nm^{-1}\right] = \left|\frac{2\pi}{\lambda\left[nm\right]}\sin\theta_{res} - \frac{2\pi}{\Lambda\left[nm\right]}\right| \tag{2.2.5}$$

The estimated points (ω, k) are reported in Figure 2-2.b and are well fitted by the theoretical curve calculated using eq. (2.2.2) for approximated surface plasmon momentum.

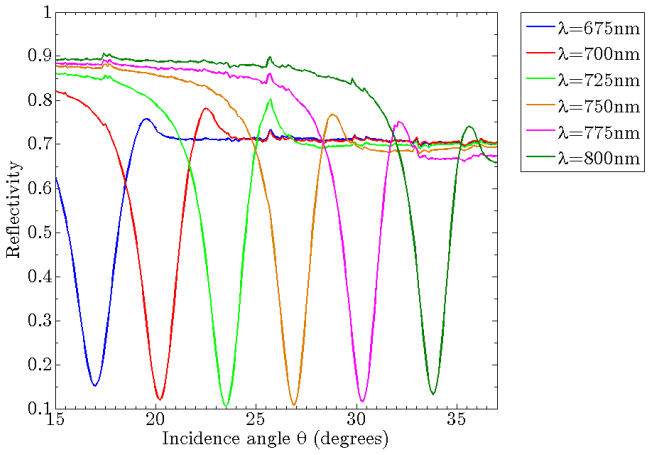

Figure 2-1: experimental reflectivity in angular scan in the range $15° - 37°$, step size $0.2°$, for incident wavelength in the range $675 - 800$ nm, step 25 nm, *p*-polarization.

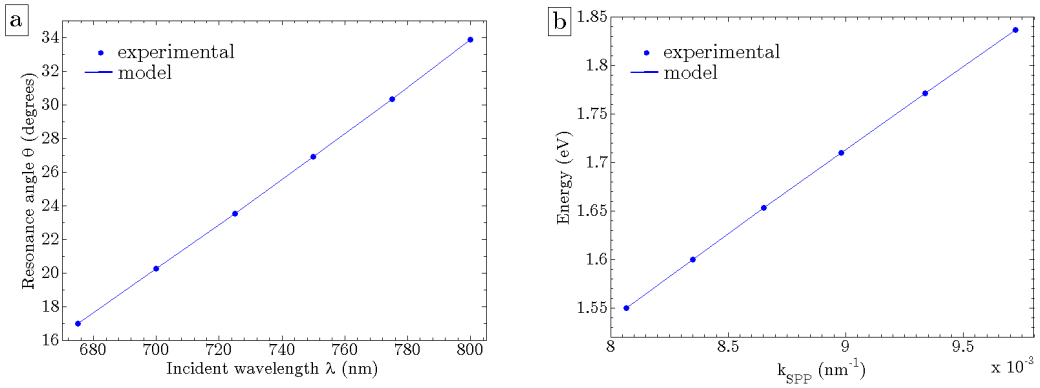

Figure 2-2: a) Resonance angle as a function of the incident wavelength (from Figure 2-1) and fitting model from eq.(2.2.4). b) Surface plasmon polaritons dispersion curve $\omega - k$, experimental data and model from eq.(2.2.4).

2.3 Azimuthal rotation of the grating plane

After rearranging resonance equations (2.2.3) in the polar angle θ_{res} unknown, an analytical expression for the resonance angle is obtained[42]:

$$\theta_{\mp} = \arcsin\left(\frac{\lambda}{\Lambda}\cos\varphi \mp \sqrt{S^2 - \left(\frac{\lambda}{\Lambda}\sin\varphi\right)^2}\right) \tag{2.3.1}$$

where $S = k_{SPP} \,/\, \left(2\pi \,/\, \lambda\right)$.

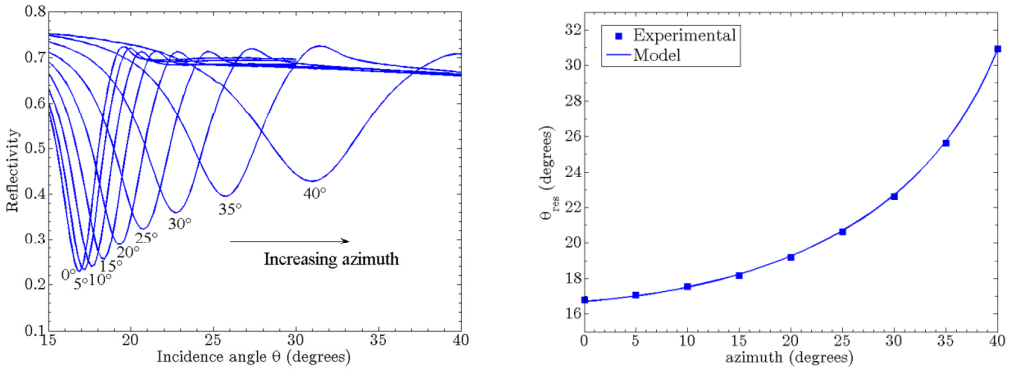

Figure 2-3: a) Experimental reflectivity for polar angular scan in the range $15° - 40°$, step size $0.1°$, at incident $\lambda = 675$ nm and increasing azimuth values $\varphi = 0° - 40°$, step $5°$, *p*-polarization. b) Resonance angle θ_{res} as a function of azimuth φ : experimental points and fit with eq. (2.3.1).

As a consequence of the last expression, SPPs are supported by a grating structure only in the azimuth range where the term under square-root is positive:

$$S^2 - \left(\frac{\lambda}{\Lambda}\sin\varphi\right)^2 \geq 0 \tag{2.3.2}$$

that is to say in the range between $\varphi = 0°$ and the maximum value $\varphi_{\max}$ given by:

$$\varphi_{\max} = \arcsin\left(S\frac{\Lambda}{\lambda}\right) \tag{2.3.3}$$

For greater azimuth values, no resonance angle θ_{res} can exist. $\theta_{-}\left(\varphi\right)$ is an increasing function of azimuth: when azimuth increases, the resonance polar angle θ_{res} shifts towards greater values (see Figure 2-3.a) as far as the resonance value in correspondence of the maximum azimuth $\varphi_{\max}$ is assumed.

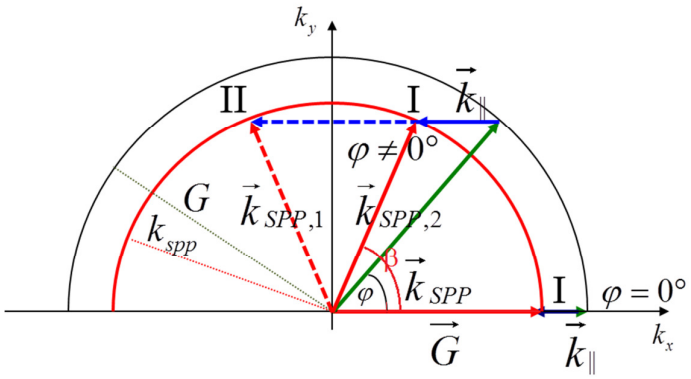

Figure 2-4: scheme of the wavevector composition at resonance condition in the reciprocal k-space, both for null azimuth $\varphi = 0°$ and in the rotated-grating case $\varphi \neq 0°$.

Depending on the grating period Λ and on the illuminating wavelength λ, also a second solution θ_+ in eq. (2.3.1) could exist between a limit azimuth value φ_c and the maximum value $\varphi_{\max}$: in this range two resonance dips can be excited with the same incident wavelength at two distinct resonance angles θ_- and θ_+. In correspondence of $\varphi = \varphi_c$ the resonance angle is equal to $90°$, thus rearranging terms in eq. (2.3.1) we get the following expression for the critical azimuth φ_c:

$$\varphi_c = \arccos\left(\frac{1 - S^2 + \frac{\lambda^2}{\Lambda^2}}{2\frac{\lambda}{\Lambda}}\right) \tag{2.3.4}$$

On the other hand, $\theta_+(\varphi)$ is a decreasing function of azimuth: when azimuth increases from the critical value φ_c, the resonance angle θ_{res} shifts towards lower values as far as it reaches the resonance value in correspondence of the maximum azimuth $\varphi_{\max}$.

Also the increase in resonance-dip width with azimuth angle (cfr. Figure 2-3.a) can be explained by the geometrical description in wavevector space (Figure 2-4). The k_{SPP}-circle has a natural width Δk_{SPP} that is related to SPP-decay and is associated to adsorption sources such as metal dissipation. For increasing azimuth the circle is intersected along a gradually increasing thickness, thus the width in wavevector-space scales with azimuth φ as:

$$\Delta k_{SPP}(\varphi) = \frac{\Delta k_{SPP}(\varphi = 0°)}{\cos\varphi} \tag{2.3.5}$$

In summary, in the case of $n = -1$ resonance, resonance angle increases for increasing azimuth angle. For azimuth greater then a critical value φ_c, a second resonance appears which shifts in the opposite direction for increasing azimuth with respect to the first one. The two dips approach and merge into a single broad dip in correspondence of the maximum azimuth value $\varphi_{\max}$.

2.4 Polarization Role in the conical mounting

In the classical mounting, i.e. when the scattering plane is parallel to the grating symmetry plane, $\left(\boldsymbol{k}_{\parallel}^{(i)} \parallel \boldsymbol{G}\right)$, *p*-polarization (TM-mode) is the most effective for SPP excitation: while under *s*-illumination almost all incident energy is reflected away at every incidence angle, since TE-SPP cannot be supported, in the case of *p*-polarization instead, a dip appears in reflectivity in correspondence of the incidence angle θ_{res} at which the incident energy couples with surface plasmon modes and dissipates while propagating along the metal surface. On the other hand, as a consequence of the symmetry breaking after azimuthal rotation, not only *p*-polarized but also *s*-polarized light can contribute to SPP excitation: a reflectivity dip can appear under *s*-illumination and the far-field can exhibit a *s*-contribution also in the case of incident *p*-polarization (*polarization conversion*). As azimuth increases, *p*-polarization is no longer the most effective for SPP excitation and the illuminating polarization must be tuned in order to optimize the coupling.

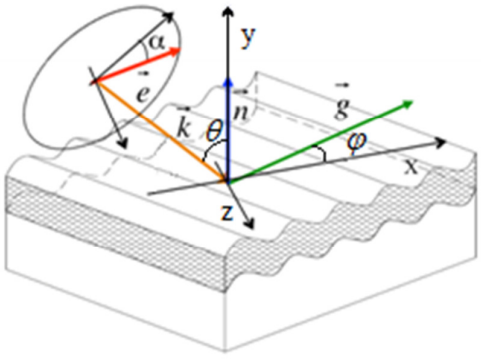

Figure 2-5: scheme of the incidence frame.

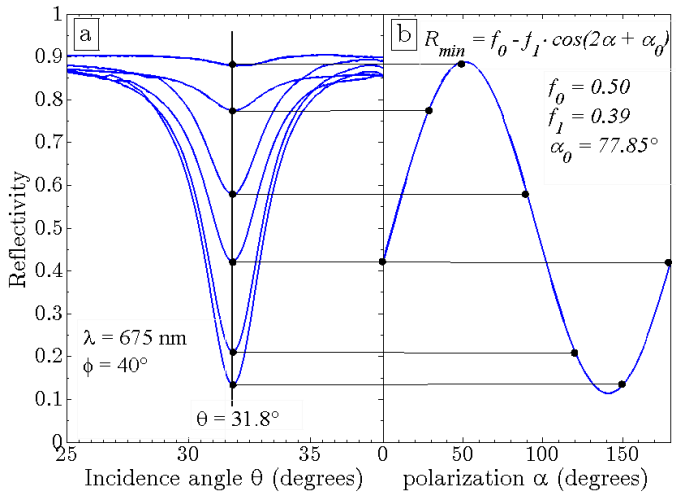

Figure 2-6: Reflectivity for angular scan in the range $25° - 38°$, step size $0.1°$, at incident $\lambda = 675$ nm and azimuth $\varphi = 40°$ for different incident polarization α in the range $0° - 180°$, step size $30°$. b) Reflectivity minima as a function of polarization angle and fit curve (eq. (2.4.1)).

Reflectivity-minimum $R_{\min}$ exhibits a periodic dependence on the polarization angle α which is well fitted by a harmonic function:

$$R_{\min} = f_0 - f_1 \cos\left(m \cdot \alpha + \alpha_0\right) \tag{2.4.1}$$

where f_0, f_1, m and α_0 are expected to be fitting parameters that depend on the incidence angles and wavelength and on the optical properties of the metallic grating (layer materials and thicknesses).

This behaviour can be explained by assuming that only the electric-field component that lies on the grating symmetry plane is effective for SPP excitation and the other components contribute to the reflectivity term, thus:

$$R \propto \left|\hat{\boldsymbol{e}} \cdot \left(\hat{\boldsymbol{g}} \times \hat{\boldsymbol{n}}\right)\right|^2 \tag{2.4.2}$$

where the versor $\hat{\boldsymbol{e}}$ is paraller to the incident electric-field direction, $\hat{\boldsymbol{g}}$ indicates the grating momentum direction and $\hat{\boldsymbol{n}}$ is the normal to the grating plane. In the considered reference frame (see Figure 2-5) these versors have the following expressions:

$$\begin{aligned}\hat{\boldsymbol{e}} &= \left(\cos\theta\cos\alpha, \sin\alpha, \sin\theta\cos\alpha\right)\\ \hat{\boldsymbol{k}} &= \left(\cos\beta, \sin\beta, 0\right)\\ \hat{\boldsymbol{g}} &= \left(\cos\varphi, \sin\varphi, 0\right)\end{aligned} \tag{2.4.3}$$

This model[43] forecasts that $m = 2$, i.e. the polarization oscillation has a π periodicity, and gives an analytical expression for the phase term $\alpha_{\min}$ as a function of the azimuth φ and the resonance angle θ:

$$\alpha_0 = \arcsin\left(-\frac{\cos\theta\sin 2\varphi}{\cos^2\theta\sin^2\varphi + \cos^2\varphi}\right) \tag{2.4.4}$$

The coupling strength is maximized, i.e. the reflectivity depth is minimized, if the relation $\cos\left(2\alpha_{\min} + \alpha_0\right) = 1$ is satisfied in eq. (2.4.1), where $\alpha_{\min}$ is the optimal polarization angle. Thus we get the following relation:

$$\alpha_{\min} = -\frac{\alpha_0}{2} + k\pi \tag{2.4.5}$$

where $k \in \mathbb{Z}$. A simpler expression for $\alpha_{\min}$ as a function of the incidence angles θ, φ is given by:

$$\alpha_{\min} = \pi - \arctan\left(\tan\varphi\cdot\cos\theta_{res}\right) \tag{2.4.6}$$

Reflectivity spectra have been collected at the fixed azimuth value $\varphi = 56.5°$ for different incident wavelengths λ in the range $600 - 640$ nm, step 5 nm (see Figure 2-7). In correspondence of each resonance angle, a scan of the polarization angle α (from $0°$ to $180°$, step $20°$, $\alpha = 0°$ and $\alpha = 90°$ correspond respectively to *p*-polarization and *s*-polarization) registering for each resonance condition the corresponding optimal polarization $\alpha_{\min}$. From the data analysis of all the samples performed at different wavelength it results that m has a mean value of 2.004 ± 0.002 rad^{-1}, indicating that the polarization oscillation has a π periodicity in perfect accordance with the model (2.4.1) and that SPP excitation can be suppressed at $\alpha_{\min} \pm 90°$ as expected. Figure 2-9 reports the experimental data of the phase term α_0 as a function of the incident λ. Experimental points are well fitted by the curve given in eq. (2.4.4), both for the first (blue line) and second (red line) dip.

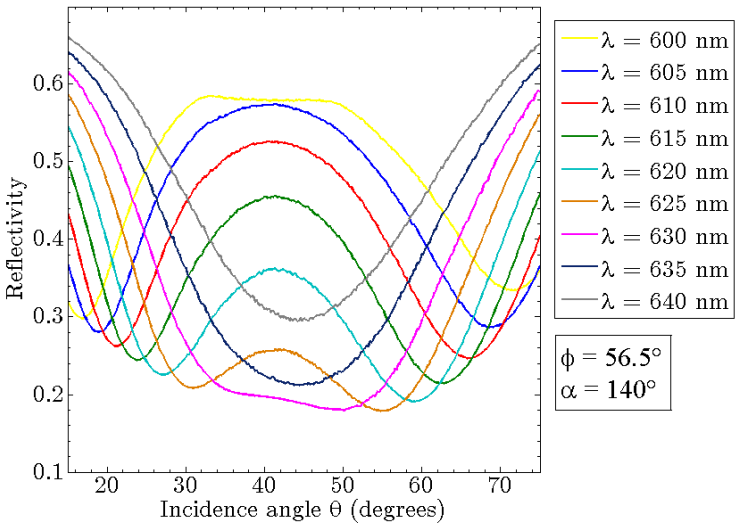

Figure 2-7: Experimental reflectivity for angular scan in the range $15° - 75°$, step size $0.2°$, at incident walengths λ in the range $600 - 640$ nm, step size 5 nm, fixed azimuth $\varphi = 56.5°$, polarization $\alpha = 140°$.

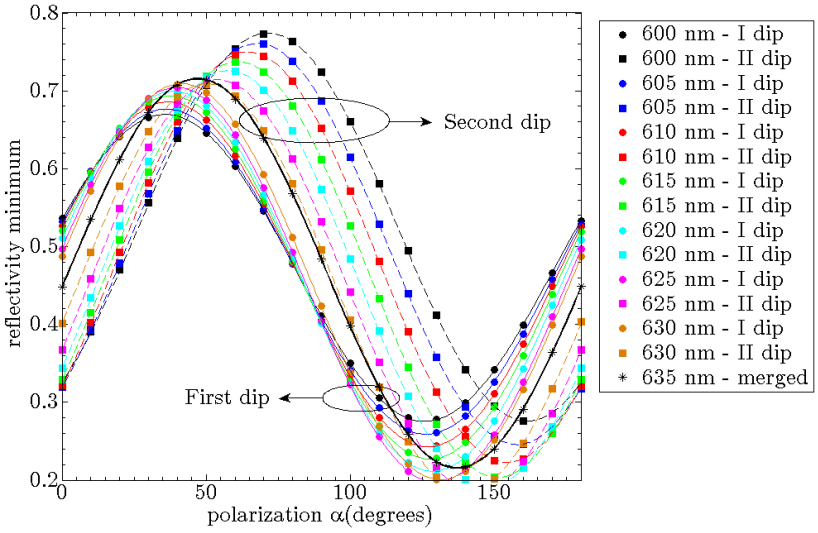

Figure 2-8: Experimental reflectivity minima at fixed $\varphi = 56.5°$ reported as a function of the polarization angle $\alpha = 0° - 180°$, step size $20°$, for different incident wavelengths in the range $600 - 635$ nm, step 5 nm. Data have been fitted using eq. (2.4.1).

Table 2-1: parameter estimation from the fit of data in Figure 2-8 with eq. (2.4.1)

λ (nm)	f_0	f_1	m	$\alpha_0(^\circ)$
600 (I)	0.4726	0.1971	2.005	108.3595
600 (II)	0.5249	0.2494	2.003	37.1052
605 (I)	0.4678	0.2087	1.997	107.3980
605 (II)	0.5032	0.2576	1.998	44.3879
610 (I)	0.4642	0.2213	2.010	106.1403
610 (II)	0.4863	0.2637	2.003	51.2243
615 (I)	0.4602	0.2333	1.999	104.7854
615 (II)	0.4706	0.2671	2.003	58.0174
620 (I)	0.4554	0.2440	2.009	102.8037
620 (II)	0.4586	0.2673	2.010	64.5736
625 (I)	0.4507	0.2535	1.997	100.5446
625 (II)	0.4493	0.2650	1.999	71.9077
630 (I)	0.4549	0.2544	2.002	97.1915
630 (II)	0.4484	0.2607	2.004	79.6195
635(merged)	0.4655	0.2498	2.009	85.9224

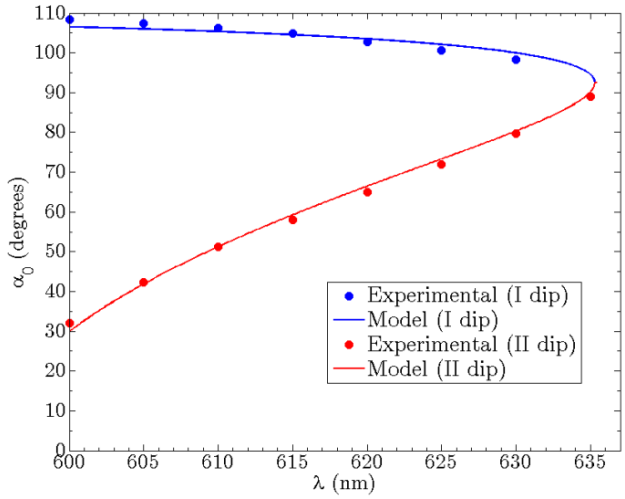

Figure 2-9: comparison of model (2.4.4) with experimental values of α_0 from data fit in Figure 2-8.

2.5 Conclusions

The vectorial model provides a simple analytical approach to the description of surface plasmon polaritons excitation and propagation on metallic gratings. For given grating period and dielectric function of the stack, an estimation of the resonance angle can be calculated and its dependence on the incident wavelength and on the azimuth rotation well fits experimental data. Vectorial model allowed to understand the consequences of symmetry breaking after azimuthal rotation and provided an analytical expression for the optimal polarization angle which well reproduces the trend of experimental data:

$$\tan \alpha_{\min} = \tan \varphi \cdot \cos \theta_{res} \tag{2.5.1}$$

where φ is the azimuth angle and θ_{res} the resonance angle at the considered wavelength λ. Last expression of $\alpha_{\min}$ will result extremely useful in chapter 4, when it will be necessary to select the incident polarization that optimized the reflectivity depth for sensing purposes. As the comparison with experimental data has showed, this formula provides a good approximation without the need of more rigorous calculations.

On the other hand, the vectorial model is affected by strong limitations in the estimation of reflectivity curve trend, and in the calculation of diffracted-orders intensity in general. In order to properly estimate the reflectivity curve and study its dependence on the grating profile, a more rigorous approach to the problem is necessary.

3 Chandezon's method

3.1 Introduction

In the previous chapter the vectorial model was introduced and exploited in order to analyze surface plasmon polaritons excitation on metallic gratings and understand the phenomenology underlying an azimuthal rotation of the structure and the polarization role in this configuration. However this model is a simple tool that allows identifying resonance position with an accuracy that decreases for increasing grating amplitude, i.e. when grating profile must be taken into account in order to properly describe the coupling of the incident light. Moreover, the vectorial model cannot predict coupling strength and thus it is not able to give a precise estimation of diffracted order weights, e.g. reflectivity or transmission intensity.

Therefore a rigorous approach is necessary in order to exactly solve the problem of a monochromatic plane wave incident on a patterned surface and to simulate the optical response of such multilayered patterned structures. In the past decades, several numerical methods have been developed in order to compute the optical response of periodically modulated multilayered stacks. Among these algorithms, Chandezon's method (hereafter the *C-method*) revealed itself as one of the most efficient techniques for a rigorous solution of smooth grating diffraction problem. The algorithm is a curvilinear coordinate modal method by Fourier expansion that has gone through many stages of extension and improvement. The original theory was formulated by J. Chandezon et al.[44,45] for uncoated perfectly conducting gratings in classical mountings. Various author extended the method to conical diffraction gratings[46]. G. Granet et al. [47], T.W. Preist et al. [48] and L. Li et al. [49] allowed the various profile of a stack of gratings to be different from each other, although keeping the same periodicity. Solving the vertical faces case in a simple manner, J.P. Plumey et al. [50] have showed that the method can be applied to overhanging gratings. In the numerical context, L. Li improved the numerical stability[51] and efficiency[52] of the C-method.

In this work, the C-method has been implemented in MATLAB environement in order to compute the optical response of sinusoidal metallic gratings and compare the numerical

results with experimental data from reflectivity analyses on fabricated samples. Moreover a simulation code provides a fundamental tool for the optimization of grating supports that exhibit the best optical features. Thus simulation provides to nanofabrication the optimal windows of process for the realization of optimized optical components.

3.2 The C-Method

3.2.1 The coordinate transformation

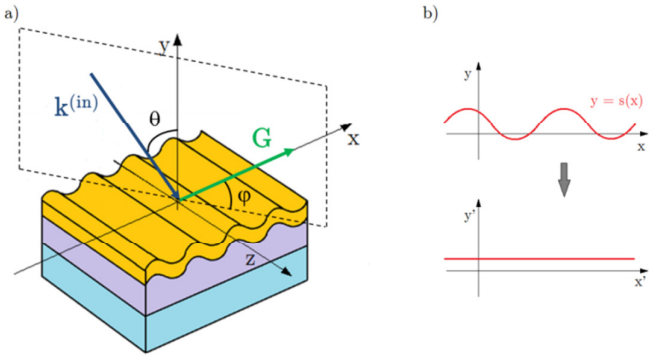

Figure 3-1: a) Scheme of the considered reference frame and scattering plane orientation. b) Coordinate transformation in Chandezon's method (3.2.1).

The setup is as it follows: the grating profile is described by a differential curve $y = s(x)$, periodic in the x-direction with periodicity Λ. The basic feature of the C-method consists in the choice of a non-orthogonal coordinate system (u, v, w) that maps the interfaces between different media to parallel planes (see Figure 3-1.b):

$$\begin{aligned} u &= y - s(x) \\ v &= x \\ w &= z \end{aligned} \tag{3.2.1}$$

Since (3.2.1) is a global coordinates transformation, Maxwell's equations covariant formalism is necessary. In a source-free medium the time-harmonic Maxwell equations in term of the covariant field component can be written as[53]

$$\partial_i \sqrt{g} g^{ij} E_j = 0 \tag{3.2.2}$$

$$\frac{1}{\sqrt{g}} \varepsilon^{ijk} \partial_j E_k = i\mu \frac{\omega}{c} g^{ij} H_j \tag{3.2.3}$$

$$\partial_i \sqrt{g} g^{ij} H_j = 0 \tag{3.2.4}$$

$$\frac{1}{\sqrt{g}} \varepsilon^{ijk} \partial_j H_k = -i\varepsilon \frac{\omega}{c} g^{ij} E_j \tag{3.2.5}$$

ε^{ijk} being the completely antisymmetric Levi-Civita tensor[i]. The parameter g is the determinant of the contravariant metric tensor g^{ij}, ε and μ are respectively the dielectric permittivity and the magnetic permeability of the medium. The covariant form[ii] g_{ij} is the following:

$$g = \begin{pmatrix} 1+s'^2 & s' & 0 \\ s' & 1 & 0 \\ 0 & 0 & 1 \end{pmatrix} \tag{3.2.6}$$

In this case $g = 1$, since coordinate transformation (3.2.1) conserves volumes.

The reference frame is the following: the *y*-axis is perpendicular to the grating plane and the grating vector $\boldsymbol{G}$ is oriented along the *x*-axis positive direction (Figure 3-1.a). The scattering plane is perpendicular to the grating plane and forms an azimuth angle φ with the grating symmetry plane. This reference frame is different from the choice in the previous section (chapter 2 - Vectorial model), in order to simplify the coordinate transformation (3.2.1) and the form of the metric tensor g (3.2.6) after azimuthal rotation: with these conventions, the grating is kept fixed and the scattering plane azimuthally rotates.

The incident wavevector $\boldsymbol{k}^{(i)}$ is given by:

$$\boldsymbol{k}^{(i)} = \frac{\omega}{c}\left(\sin\theta\cos\varphi, -\cos\theta, \sin\theta\sin\varphi\right) = (\alpha_0, -\beta_0, \gamma) \tag{3.2.7}$$

and the wavevector of the *n*-th diffraction order has the following form:

$$\boldsymbol{k}^{(n)} = \left(\alpha_n, \beta_n, \gamma\right) \tag{3.2.8}$$

---

[i] ε^{ijk} equals 1 if (i,j,k) is an even permutation of $(1,2,3)$, -1 if it is an odd permutation, and 0 if any index is repeated.

[ii] $g_{i'j'} = \Lambda^i_{i'} \Lambda^j_{j'} \delta_{ij}$ where δ_{ij} is Kronecker's delta, Λ^i_j is the Jacobi's matrix associated to the coordinate transformation: $\Lambda^i_j = \partial x^i / \partial x^j$. The metric tensor g_{ij} allows calculating covariant components v_i of a vector $\boldsymbol{v}$ from contravariant ones v^i and vice-versa: $v_i = g_{ij} v^j$, $v^i = g^{ij} v_j$.

where $\alpha_n = \alpha_0 + n \cdot G$ and $\beta_n = \sqrt{k^{(i)2} - \alpha_n^2 - \gamma^2}$.

With these definitions and after some algebraic manipulations, curl equations (3.2.3) and (3.2.5) can be rearranged into the following system of differential equations in the tangential components unknown $\left(H_x, E_z, H_z, E_x\right)$:

$$\frac{\partial H_x}{\partial u} = i\omega\varepsilon E_z + \frac{\partial}{\partial x}\left(\frac{s'}{1+s'^2} H_x\right) + \frac{\partial}{\partial x}\left(\frac{1}{1+s'^2}\frac{i}{\omega\mu}\frac{\partial E_z}{\partial x} + \frac{1}{1+s'^2}\frac{\gamma}{\omega\mu} E_x\right) \tag{3.2.9}$$

$$\frac{\partial E_z}{\partial u} = \frac{s'}{1+s'^2}\frac{\partial E_z}{\partial x} + \frac{1}{1+s'^2}\frac{\gamma}{\omega\varepsilon}\frac{\partial H_z}{\partial x} + \frac{1}{1+s'^2}\left(i\omega\mu - i\frac{\gamma^2}{\omega\varepsilon}\right) H_x \tag{3.2.10}$$

$$\frac{\partial H_z}{\partial u} = \frac{s'}{1+s'^2}\frac{\partial H_z}{\partial x} - \frac{1}{1+s'^2}\frac{\gamma}{\omega\mu}\frac{\partial E_z}{\partial x} - \frac{1}{1+s'^2}\left(i\omega\varepsilon - i\frac{\gamma^2}{\omega\mu}\right) E_x \tag{3.2.11}$$

$$\frac{\partial E_x}{\partial u} = -i\omega\mu H_z + \frac{\partial}{\partial x}\left(\frac{s'}{1+s'^2} E_x\right) - \frac{\partial}{\partial x}\left(\frac{1}{1+s'^2}\frac{i}{\omega\varepsilon}\frac{\partial H_z}{\partial x} + \frac{1}{1+s'^2}\frac{\gamma}{\omega\varepsilon} H_x\right) \tag{3.2.12}$$

where we used the following relation:

$$\frac{\partial F_i}{\partial z} = i\gamma F_i \tag{3.2.13}$$

where F stands for H_x, E_z, H_z, E_x . In fact, since the grating vector has no components in the z-direction, momentum z-component is conserved (see eq. (2.2.1)) and is a constant parameter of the problem.

3.2.2 Bloch-Floquet's theorem

As suggested by Bloch-Floquet's theorem (see appendix C), thanks to the periodicity of the media in the x-direction a generic field $F(x,y,z)$ (where F may stand for H_x, E_z, H_z, E_x) can be expanded in pseudo-Fourier series:

$$F\left(x,u,z\right) = e^{i\gamma z} \sum_{m=-\infty}^{+\infty} F_m(u) e^{i\alpha_m x} \tag{3.2.14}$$

where $F_m(u)$ is a function periodic in x .

Likewise, also the profile functions $C(x) = 1 / \left(1 + s'^2\right)$ and $D(x) = s' / \left(1 + s'^2\right)$ in eq. (3.2.9) - (3.2.12) are periodic in x and can be expanded as well (see Appendix D). Laurent's rule[iii] can been applied for the Fourier factorization[54], assuming the continuity of profile function derivative. In the case of sharp edges instead, equations should be rearranged in order to make the inverse-rule factorization applicable[55]. Since in our case of interest the grating profile is a regular function, after applying Laurent's factorization we get the following system of equations in the Fourier space:

$$-i\frac{\partial H_x^m}{\partial u} = \omega\varepsilon E_z^m + \sum_n \alpha_m D_{m-n} H_x^n - \frac{1}{\omega\mu}\sum_n \alpha_m C_{m-n}\alpha_n E_z^n + \frac{\gamma}{\omega\mu}\sum_n \alpha_m C_{m-n} E_x^n \quad (3.2.15)$$

$$-i\frac{\partial E_z^m}{\partial u} = \sum_n D_{m-n}\alpha_n E_z^n + \frac{\gamma}{\omega\varepsilon}\sum_n C_{m-n}\alpha_n H_z^n + \left(\omega\mu - \frac{\gamma^2}{\omega\varepsilon}\right)\sum_n C_{m-n} H_x^n \quad (3.2.16)$$

$$-i\frac{\partial H_z^m}{\partial u} = \sum_n D_{m-n}\alpha_n H_z^n - \frac{\gamma}{\omega\varepsilon}\sum_n C_{m-n}\alpha_n E_z^n - \left(\omega\varepsilon - \frac{\gamma^2}{\omega\mu}\right)\sum_n C_{m-n} E_x^n \quad (3.2.17)$$

$$-i\frac{\partial E_x^m}{\partial u} = -\omega\mu H_z^m + \sum_n \alpha_m D_{m-n} E_x^n + \frac{1}{\omega\varepsilon}\sum_n \alpha_m C_{m-n}\alpha_n H_z^n - \frac{\gamma}{\omega\varepsilon}\sum_n \alpha_m C_{m-n} H_x^n \quad (3.2.18)$$

3.2.3 Truncation

After truncation[56] to a finite order N, the problem consists in the numerical solution of a system of $8N + 4$ first order differential equations in each medium:

$$-i\frac{\partial \boldsymbol{U}}{\partial u} = T\,\boldsymbol{U} \quad (3.2.19)$$

where $\boldsymbol{U} = \left(H_x^{-N}, \cdots, H_x^N, E_z^{-N}, \cdots, E_z^N, H_z^{-N}, \cdots, H_z^N, E_x^{-N}, \cdots, E_x^N\right)$ is a $8N + 4$ vector and T is a $8N + 4$ squared matrix:

[iii] For given functions $f(x)$ and $g(x)$ that are continuous, smooth, bounded and periodic, either everywhere in the domain or piecewise with concurrent jump discontinuities, the Fourier cofficients of $h(x) = f(x)g(x)$ can be obtained from the Fourier coefficients of $f(x)$ and $g(x)$ by: $h_n = \sum f_{n-m} g_m$.

$$T = \begin{pmatrix} A1 & A2 & B1 & B2 \\ A3 & A4 & B3 & B4 \\ C1 & C2 & D1 & D2 \\ C3 & C4 & D3 & D4 \end{pmatrix} \tag{3.2.20}$$

where $A1, A2 \ldots D4$ are 16 matrices of size $2N+1$, given for $m,n \in \left(-N,+N\right)$ by:

$$\begin{aligned} A1_{mn} &= \alpha_m D_{m-n} \\ A2_{mn} &= \omega\varepsilon\delta_{mn} - \frac{1}{\omega\mu}\alpha_m D_{m-n}\alpha_n \\ A3_{mn} &= \left(\omega\mu - \frac{\gamma^2}{\omega\varepsilon}\right) C_{m-n} \\ A4_{mn} &= D_{m-n}\alpha_n \end{aligned} \tag{3.2.21}$$

$$\begin{aligned} B1_{mn} &= 0 \\ B2_{mn} &= \frac{\gamma}{\omega\mu}\alpha_m C_{m-n} \\ B3_{mn} &= \frac{\gamma}{\omega\varepsilon} C_{m-n}\alpha_n \\ B4_{mn} &= 0 \end{aligned} \tag{3.2.22}$$

$$\begin{aligned} C1_{mn} &= 0 \\ C2_{mn} &= -\frac{\gamma}{\omega\mu} C_{m-n}\alpha_n \\ C3_{mn} &= -\frac{\gamma}{\omega\varepsilon}\alpha_m C_{m-n} \\ C4_{mn} &= 0 \end{aligned} \tag{3.2.23}$$

$$\begin{aligned} D1_{mn} &= D_{m-n}\alpha_n \\ D2_{mn} &= \left(\frac{\gamma^2}{\omega\mu} - \omega\varepsilon\right) C_{m-n} \\ D3_{mn} &= -\omega\mu\delta_{mn} + \frac{1}{\omega\varepsilon}\alpha_m C_{m-n}\alpha_n \\ D4_{mn} &= \alpha_m D_{m-n} \end{aligned} \tag{3.2.24}$$

The problem is led to the diagonalization problem of the matrix T and the solution $\boldsymbol{U}^j(u)$ in the j-th medium can be expressed as a function of eigenvectors $\boldsymbol{V}_q^j$ and eigenvalues λ_q^j of the matrix T:

$$\boldsymbol{U}^j(u) = \sum_q b_q^j \boldsymbol{V}_q^j \, e^{i\lambda_q^j u} \tag{3.2.25}$$

where b_q^j are the weights of the corresponding eigenmodes in the expansion.

3.2.4 Boundary conditions

Thereafter boundary conditions in each medium must be imposed: continuity of the tangential components at each interfaces and outgoing-wave conditions in the first (*air*) and last (*substrate*) media. This leads to a system of $8N+4$ equations in $8N+4$ unknowns that can be solved numerically. Further details of algebraic manipulations and numerical calculations are postponed to Appendix D.

Once the mathematical problem has been solved, the electromagnetic fields can be computed inside each j-th medium:

$$F^j\left(x,u,z\right) = e^{i\gamma z}\sum_{m=-N}^{+N}\sum_{n=-N}^{+N} F_{mn}^j e^{i\lambda_n^j u} e^{i\alpha_m x} \tag{3.2.26}$$

where F stands for H_x, E_z, H_z, E_x, and F_{mn} are the F-field mn-Fourier weight. Transversal components E_y, H_y are calculated from Maxwell's equations (3.2.2)-(3.2.5) as a function of tangential components.

By applying the metric tensor to covariant components F_i, the contravariant components F^i, which represent the physical fields, can be obtained. For incident wavelength λ, polar and azimuth angles $\left(\theta,\varphi\right)$ and polarization α, the implemented algorithm yields the spatial dependency of the diffracted fields everywhere in space for the modeled grating stack. An estimation of reflection and transmission coefficients for the different diffraction orders, in particular transmittance and reflectivity values (0-diffraction orders) can be obtained. By analyzing real and imaginary parts of eigenvalues λ_q^j in (3.2.26) it is possible to distinguish between propagating and evanescent modes, which respectively contribute to far-field and near-field solutions. Thus by selecting only the evanescent contributions in the configurations where surface plasmon polaritons are excited, it is possible to describe the localized plasmonic fields of the excited modes.

3.3 Results

3.3.1 Grating design and optimization

The C-Method has been implemented in MATLAB® code and simulations have been performed[57] with a truncation order $N = 6$. The simulated stack reproduces the typical multilayer gratings that we fabricate in laboratory by laser interference lithography in the so called Lloyd's configuration (see chapter 4). This fabrication technique produces patterned areas with an almost perfect sinusoidal profile and a great homogeneity over cm^2. Thereafter the fabricated masters are replicated by soft-lithography technique by imprinting onto a thin polimeric resin film[63] (NOA61) exposed to UV light. Finally, the resin grating is coated by thermal evaporation with a multilayer metallic film: 5 nm of chromium adhesion layer, a silver film of optimized thickness, a gold layer of about 7 nm in order to prevent silver oxidation.

Silver thickness must be properly chosen in order to optimize the plasmonic response of the structure, i.e. the coupling of SPPs with the incident light, and the optimal thickness strictly depends on the amplitude of grating modulation. Simulations have been performed at the incident wavelength $\lambda = 632\,\text{nm}$ for several values of the profile amplitude in the range 20-60 nm and for varying silver thickness in the range 10-80 nm, in the case of a sinusoidal grating with fixed period $\Lambda = 500\,\text{nm}$, gold thickness 7 nm and a fixed chromium adhesion layer of 5 nm over a NOA61 substrate.

As Figure 3-2 shows, for each amplitude value a silver thickness exists that optimizes the coupling of incident light with SPP modes, i.e. that minimizes the depth of the reflectivity dip. Figure 3-3 shows some examples of reflectivity curves in angular scan for optimal combinations of profile amplitude and silver thickness. For increasing amplitude of the grating profile, the optimal silver thickness decreases (Figure 3-2) and the corresponding reflectivity curve becomes broader (Figure 3-3). This result seems to suggest the choice of a shallow grating modulation with the evaporation of the corresponding optimal thickness of silver: for an amplitude $A = 30\,\text{nm}$ the optimal silver thickness is around 80 nm. On the other hand, the coating with a great quantity of metal could affect the preservation of the

original pattern and cause lacks in accuracy of the final profile. The evaporation of about 40 nm of silver instead, could assure the control of the grating profile and at the same time a reasonable value for the reflectivity-dip FWHM (Full Width at Half Maximum). In the following analyses, an amplitude $A = 44\,\text{nm}$ has been considered and the grating optical response has been simulated for the corresponding optimal thickness of the silver film $d_{Ag} = 37.5\,\text{nm}$.

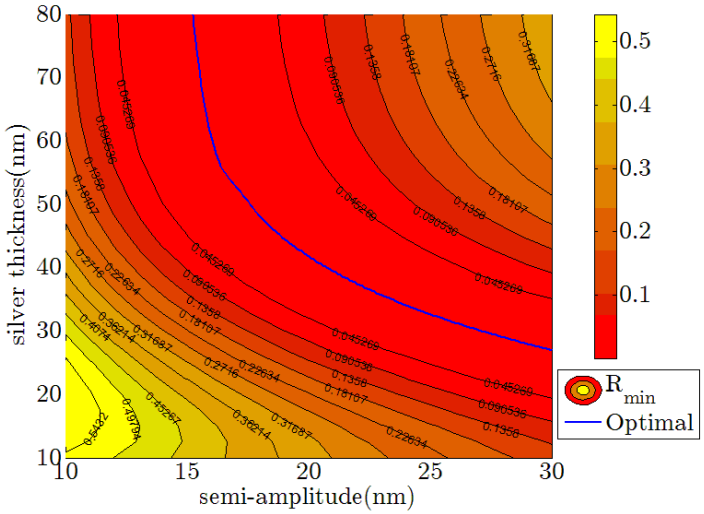

Figure 3-2: Reflectivity minimum as a function of profile amplitude and silver-film thickness for fixed period $\Lambda = 500\,\text{nm}$, fixed gold-film thickness 7 nm, incident wavelength $\lambda = 632\,\text{nm}$ (sinusoidal profile). Superimposed blue line: optimal configurations.

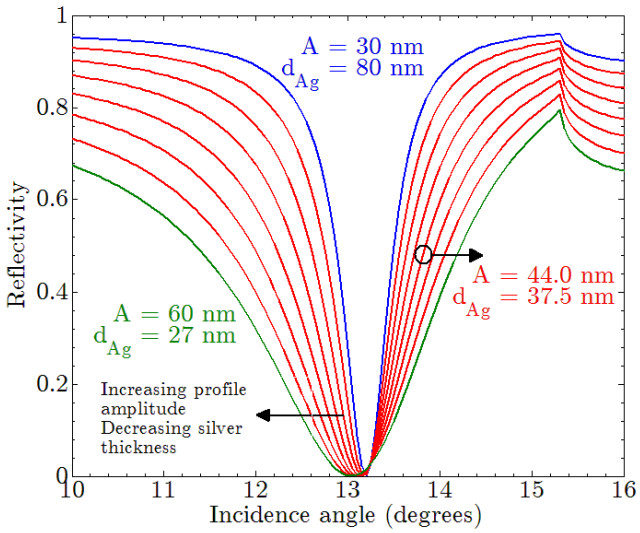

Figure 3-3: Reflectivity in angle scan for values of amplitude and silver thickness along the optimal configuration line in Figure 3-2: amplitude range 30-60nm, step 4 nm.

3.3.2 Reflectivity analysis: classical and conical mounting

If the incident wavelength is kept fixed at $\lambda = 632\,\text{nm}$, the resonance angle θ_{res} shifts towards greater values for increasing azimuth, according to eq. (2.3.1). Figure 3-4 exhibits the reflectivity spectra in angular interrogation at *p*-polarization ($\alpha = 0°$) for the azimuth values $\varphi = 0°,10°,20°,30°,40°,45°,50°,53.5°,54.5°$. As this figure shows, if *p*-polarization is maintained, dips become broader and shallower for increasing azimuth resonance since *p*-polarization becomes less effective for SPP excitation. The inset graph shows the resonance angle trend as a function of the azimuth angle: dip positions θ_{res} have been evaluated using a weighted centroid algorithm[27] and the data (θ_{res},φ) have been fitted using (2.3.1) with the parameter S unknown. The resulting estimation $S = 1.036$ allows calculating the limit azimuth values $\varphi_c = 52.91°$ and $\varphi_{\max} = 55.03°$ (see section 2.2).

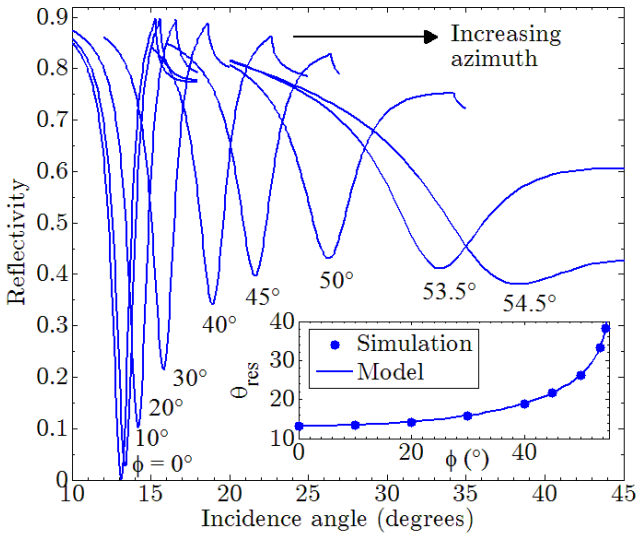

Figure 3-4: Reflectivity spectra for angular interrogation, variable azimuth $\varphi = 0°,10°,20°,30°,40°,45°,50°,53.5°,54.5°$ for the incident wavelength $\lambda = 632$ nm, *p*-polarization ($\alpha = 0°$). In the inset graph: resonance angle θ_{res} as a function of the azimuth angle φ : simulation data points and fit with vectorial model (solid line).

Figure 3-5 displays the reflectivity data in the case of azimuth $\varphi = 53.5°$. This value is greater than φ_c and thus it is possible to excite two SPP modes with the same incident wavelength. As the figure shows, two distinct resonance dips appear in correspondence of the resonance angles $\theta_- = 33.36°$ and $\theta_+ = 70.21°$. In this configuration, the incident

polarization angle α has been tuned in the range $0° - 150°$ with step size $30°$. Reflectivity depth strictly depends on polarization: the deepest dip is obtained for a polarization which is different from $\alpha = 0°$ (p-polarization) and moreover the two dips have different phase terms α_0. The minimum of reflectivity $R_{\min}$ as a function of the polarization angle exhibits a trend which is well fitted by a harmonic function with a period of $180°$, see eq. (2.4.1). In Figure 3-6 the harmonic trend is calculated for a polarization scan in a period of $180°$, for different azimuth angles $\varphi = 0°, 30°, 53.5°$ (double SPP excitation), $56°$ (merged dips) and the phase dependence on grating rotation is clearly demonstrated.

While for $\varphi = 0°$ (classical mounting) the minimum is obtained, as expected, at $\alpha = 0°$ (or $180°$), on the other hand for increasing azimuth the optimal polarization decreases both for the first and the second dip (in the range where it exists) and the two phases converge to the same value in correspondence of the dip merging close to the azimuth value $\varphi_{\max}$: $\alpha_{\min}(30°) = 149°$, $\alpha_{\min}(53.5°, Idip) = 135°$, $\alpha_{\min}(53.5°, IIdip) = 158°$, $\alpha_{\min}(56°, merged) = 143°$. The map in Figure 3-6 of the reflectivity minima as a function of both polarization and azimuth angles, provides a complete description of this phenomenology.

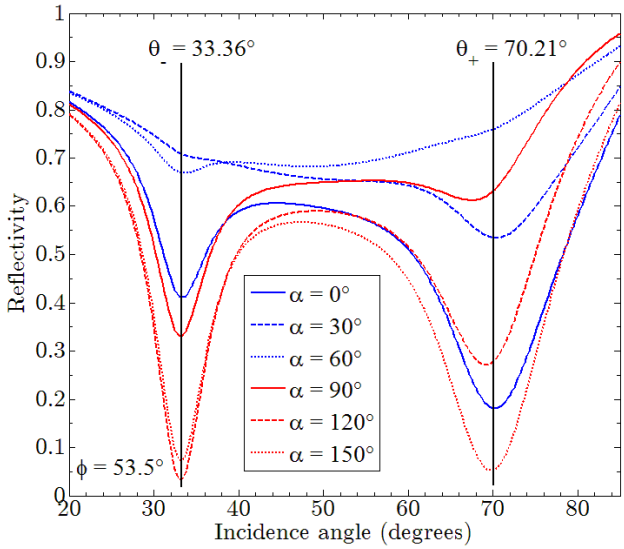

Figure 3-5: Reflectivity spectra for angular interrogation at azimuth $\varphi = 53.5°$ for the incident wavelength $\lambda = 632\,\text{nm}$, variable incident polarization α in the range $0° - 150°$ step $30°$.

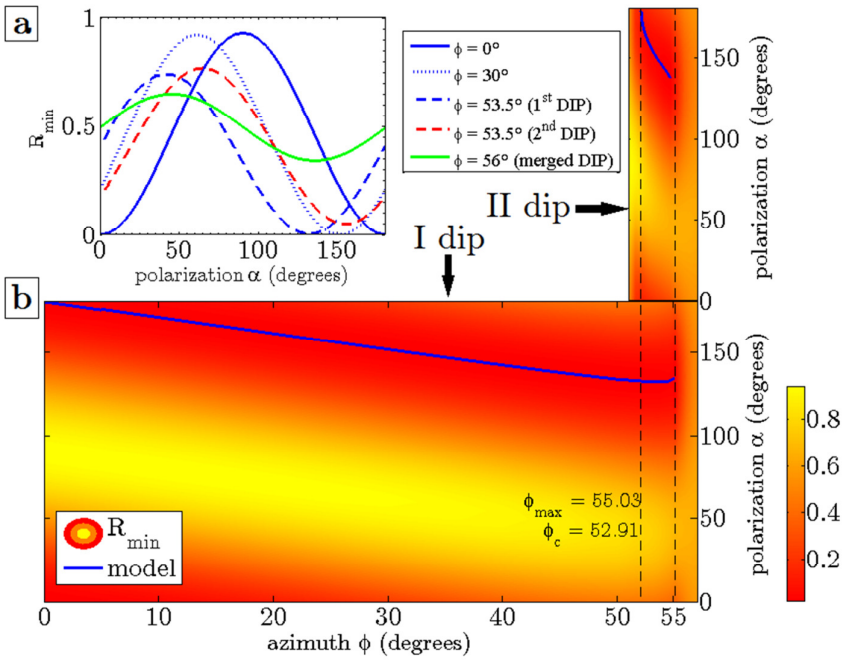

Figure 3-6: a) Reflectivity minima as a function of polarization for azimuth angles $\varphi = 0°, 30°, 53.5°$ (I and II dip), $56°$ (merged dips) at incident wavelength $\lambda = 632\,\text{nm}$. b) Reflectivity map as a function of polarization and azimuth angles for first and second dip. Superimposed blue lines: optimal polarization angle calculated with the vectorial model eq.(2.4.6).

3.3.3 Comparison with experimental data

The optical response of a fabricated metallic grating has been computed with truncation order $N = 6$ and numerical results have been compared with experimental data from reflectivity analysis of the real sample[58]. The simulated stack reproduces the multilayer structure of the considered grating: air (upper medium), Au (8 nm), Ag (35 nm), Cr (9 nm), photoresist (70 nm), Si (substrate). For each layer the optical constants (refractive index n, extinction coefficient k) have been extrapolated from ellipsometric analysis (see section 4.3.3) and have been inserted into the code. From AFM analysis, the grating profile results sinusoidal with period 505 nm and peak-to-valley amplitude 26 nm.

As Figure 3-7 shows in the case of illuminating $\lambda = 700\,\text{nm}$ at polarization $\alpha = 30°$, numerical estimation of grating reflectivity well fits experimental data within instrumental errors $(\sim 2\%)$. Reflectivity measurements have been performed by means of the

monochromatized 75 W Xe-Ne lamp of a spectroscopic ellipsometer VASE (J. A. Woollam), with angular and spectroscopic resolution respectively 0.01° and 0.3 nm

Figure 3-8 shows reflectivity spectra for angular interrogation at null azimuth $\varphi = 0^\circ$ for incident wavelengths λ in the range $675 - 775$ nm with step size 25 nm, *p*-polarization ($\alpha = 0^\circ$). In angular interrogation, reflectivity dips shift towards greater resonance angles for increasing wavelength as expected. Numerical results perfectly reproduce experimental data trends. From dip position it is possible to reconstruct SPP dispersion relation $\omega - k$ using eq. (2.2.5).

Figure 3-9 exhibits reflectivity spectra in angular interrogation for the azimuth values $\varphi = 0^\circ, 10^\circ, 20^\circ, 30^\circ, 40^\circ, 44^\circ$, incident wavelength $\lambda = 675$ nm and *p*-polarization ($\alpha = 0^\circ$). As the figure shows, if *p*-polarization is maintained, resonance dips become broader and shallower since *p*-polarization becomes less effective for SPP excitation.

Figure 3-10 shows reflectivity data for incident $\lambda = 675$ nm in the case of azimuth $\varphi = 40^\circ$: polarization is tuned in the range $0^\circ - 180^\circ$ with step size 30°. Reflectivity depth strictly depends on the incident polarization and the deepest dip is obtained for a polarization $\alpha = 141^\circ$ which is different from $\alpha = 0^\circ$ (*p*-polarization) in the case of classical incidence. The minimum of reflectivity as a function of polarization angle exhibits a trend which is well fitted by a harmonic function with a period of 180 degrees.

In Figure 3-11 experimental minima as a function of polarization for azimuth angles $\varphi = 0^\circ, 40^\circ$ at the incident wavelength $\lambda = 675$ nm and for $\varphi = 53^\circ$ at $\lambda = 610$ nm are plotted with the corresponding simulated curves superimposed. In the case $\varphi = 53^\circ$ two SPPs can be excited with the same wavelength $\lambda = 610$ nm: two distinct resonance dips appear in reflectivity spectra at the resonance angles $\theta_- = 41.8^\circ$ and $\theta_+ = 63.4^\circ$ and the resonance depth changes with a different phase α_0 for the two modes.

Table 3-1 collects α_0 estimations for the considered azimuth configurations: α_0 has been calculated from the fit of experimental and simulated data points in Figure 3-11 with eq.(2.4.1) and from the application of eq. (2.4.4) to the experimental values $\left(\theta_{res}, \varphi\right)$.

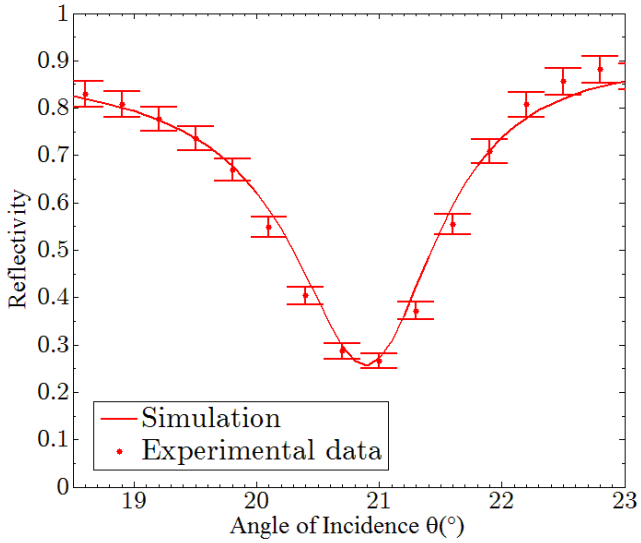

Figure 3-7: Reflectivity spectra for angular interrogation at null azimuth $\varphi = 0°$ for incident wavelengths $\lambda = 700$ nm, polarization $\alpha = 30°$. Experimental data points and simulation results (solid lines).

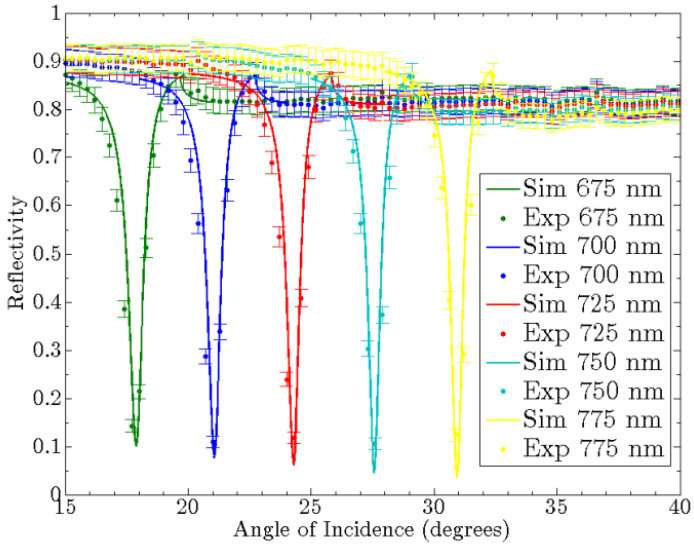

Figure 3-8: Reflectivity spectra for angular interrogation at null azimuth $\varphi = 0°$ for incident wavelengths λ in the range $675 - 775$ nm with step 25 nm, *p*-polarization ($\alpha = 0°$). Experimental data points and simulation results (solid lines).

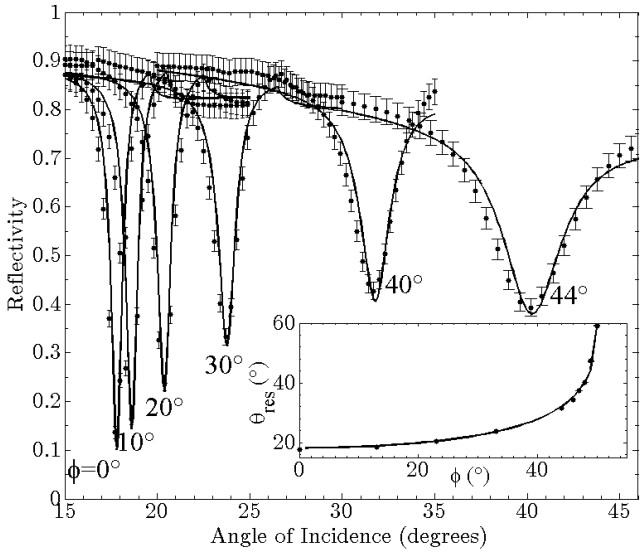

Figure 3-9: Reflectivity spectra for angular interrogation, variable azimuth $\varphi = 0°, 10°, 20°, 30°, 40°, 44°$ for the incident wavelength $\lambda = 675$ nm, p-polarization ($\alpha = 0°$). Experimental data points and simulation (solid lines). In the inset graph: resonance angle θ_{res} as a function of the azimuth angle φ : experimental points and simulation curve (solid line).

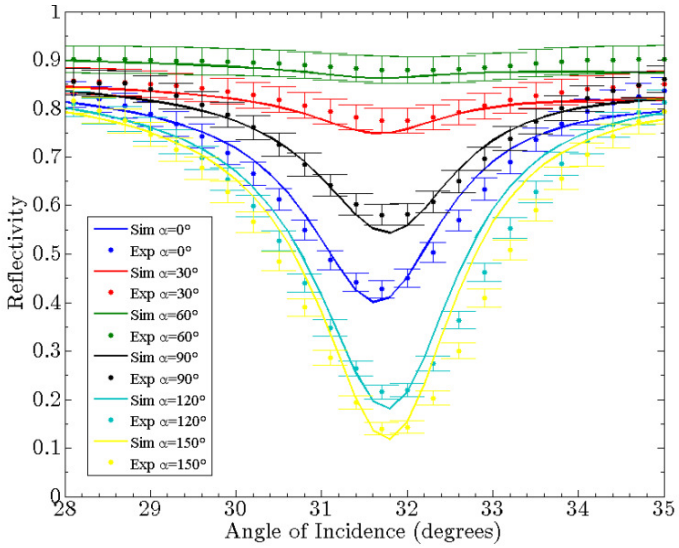

Figure 3-10: Reflectivity spectra for angular interrogation at azimuth $\varphi = 40°$ for the incident wavelength $\lambda = 675$ nm, variable incident polarization α in the range $0° - 150°$, step $30°$. Experimental data points and simulation results (solid lines).

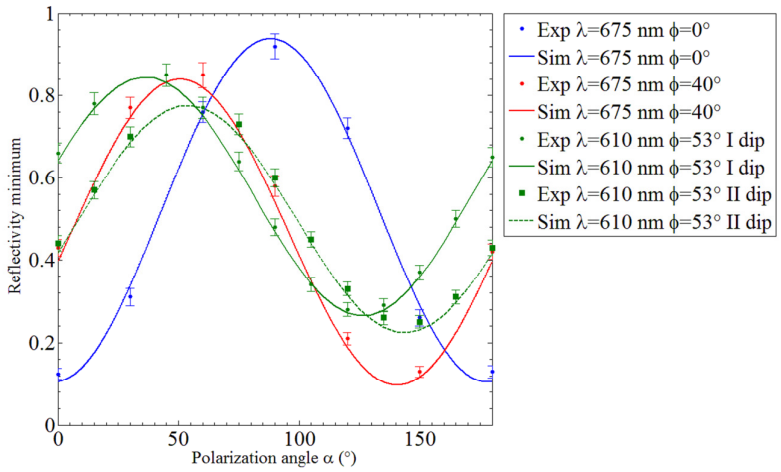

Figure 3-11: Reflectivity minima as a function of polarization for azimuth angles $\varphi = 0°$ (blue line), $\varphi = 40°$ (red line) at incident $\lambda = 675$ nm, and for $\varphi = 53°$ at $\lambda = 610$ nm (double SPP configuration – green lines). Experimental data points and simulation results (solid and dashed lines).

Table 3-1: estimation of phase α_0 from fit of experimental data with eq. (2.4.1), from simulations in Figure 3-11 and from the application of vectorial model (eq. (2.4.4)).

Phase $\alpha_0(°)$	Experimental	Vectorial model	Simulation
$\lambda = 675$ nm $\alpha = 0°$	0.5 ± 0.7	0	0.07 ± 0.04
$\lambda = 675$ nm $\alpha = 40°$	101.2 ± 0.7	101.1 ± 0.3	101.31 ± 0.01
$\lambda = 610$ nm $\alpha = 53°$ (I dip)	107.4 ± 1.6	104.1 ± 0.2	105.43 ± 0.82
$\lambda = 610$ nm $\alpha = 53°$ (II dip)	72.42 ± 2.28	71.2 ± 0.1	73.2 ± 0.54

3.3.4 Near-field numerical analysis

The electromagnetic field on the metallic surface has been computed under resonance condition at the corresponding optimal polarization values. The following graphs display some examples of this near-field numerical calculation. Figure 3-12 reports the magnetic field *z*-component over an area of $2\mu m \times 2\mu m$ for classical incidence: null azimuth and *p*-polarization ($\varphi = 0°, \alpha = 0°$). The *x*- and *y*-components are obviously null: the propagating

SPP is *p*-polarized. H-field intensity in air as a function of the distance from the grating surface is reported: the decay is exponential as expected from the theory.

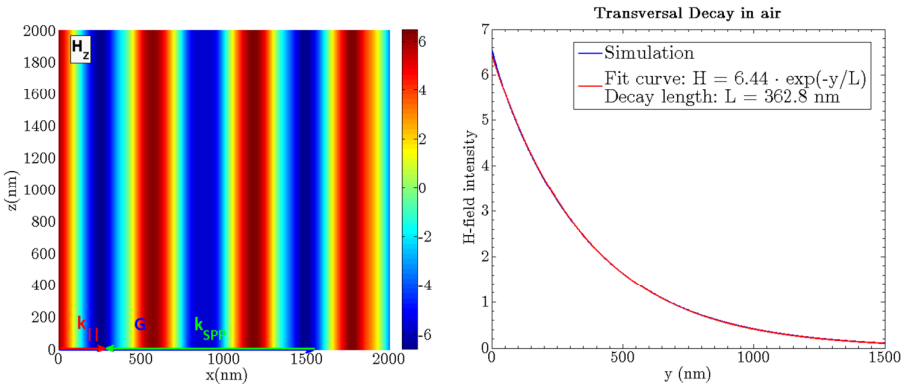

Figure 3-12: Magnetic field (*z*-component) calculation on the grating surface at SPP resonance condition for $\lambda = 632$ nm, null-azimuth, *p*-polarization, resonance polar angle $\theta_{res} = 13.12°$. Magnetic field intensity as a function of the distance from the grating surface into air. Fit curve and estimated extinction length L.

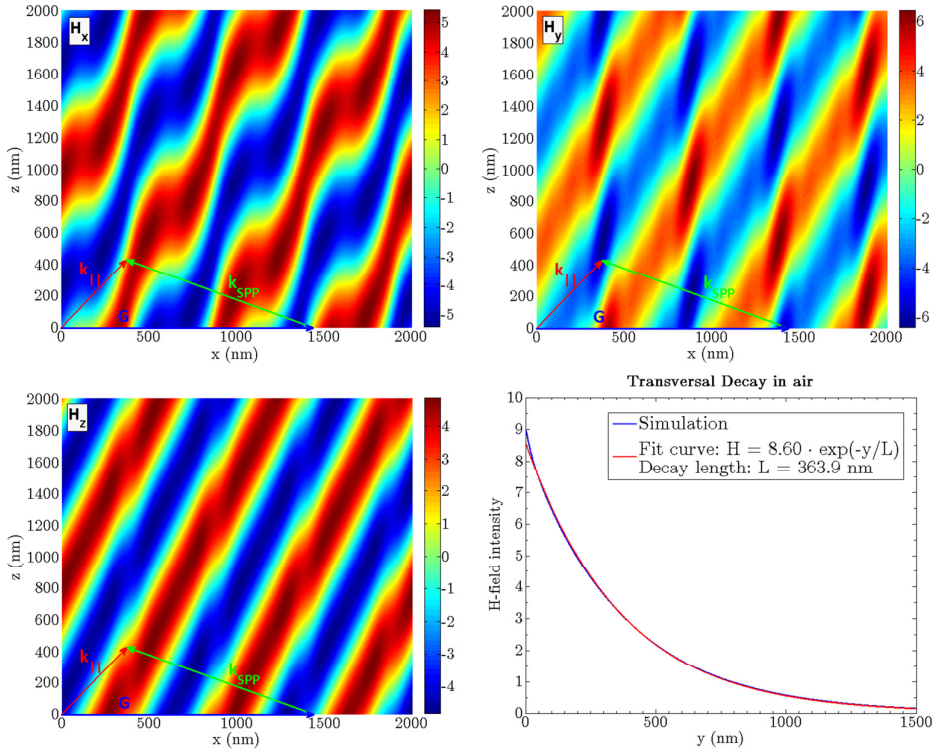

Figure 3-13: Magnetic- field component calculation on the grating surface at SPP resonance condition for $\lambda = 632$ nm, azimuth $\varphi = 53.5°$, polarization $\alpha_{\min} = 135°$, resonance polar angle $\theta_{res} = 33.36°$ (I dip) . Vector sum of eq. (2.2.1) is superimposed to each graph. Magnetic field intensity as a function of the distance from grating surface into air: fit curve and estimated extinction length L.

Fitting with an exponential curve allows to estimate the extinction length L which results equal to 362 nm and comparable with the decay length of SPPs propagating on a flat metallic surface in the PCSPR[59].

After the sample is azimuthally rotated, a different polarization is needed to optimize the coupling: the excited surface plasmon polaritons are no longer *p*-polarized as Figure 3-13 and Figure 3-14 show respectively for the first ($\theta_- = 33.36°$) and the second dip ($\theta_+ = 70.21°$) at $\varphi = 53.5°$, where all magnetic-field components are different from zero. Vector sum in momentum conservation law, eq. (2.2.3), has been superimposed to each graph in order to clearly represent grating orientation ($\boldsymbol{G}$ is perpendicular to the grating grooves), the scattering plane (parallel to $\boldsymbol{k}_{||}^{(in)}$) and the direction of SPP propagation (parallel to $\boldsymbol{k}_{SPP}$).

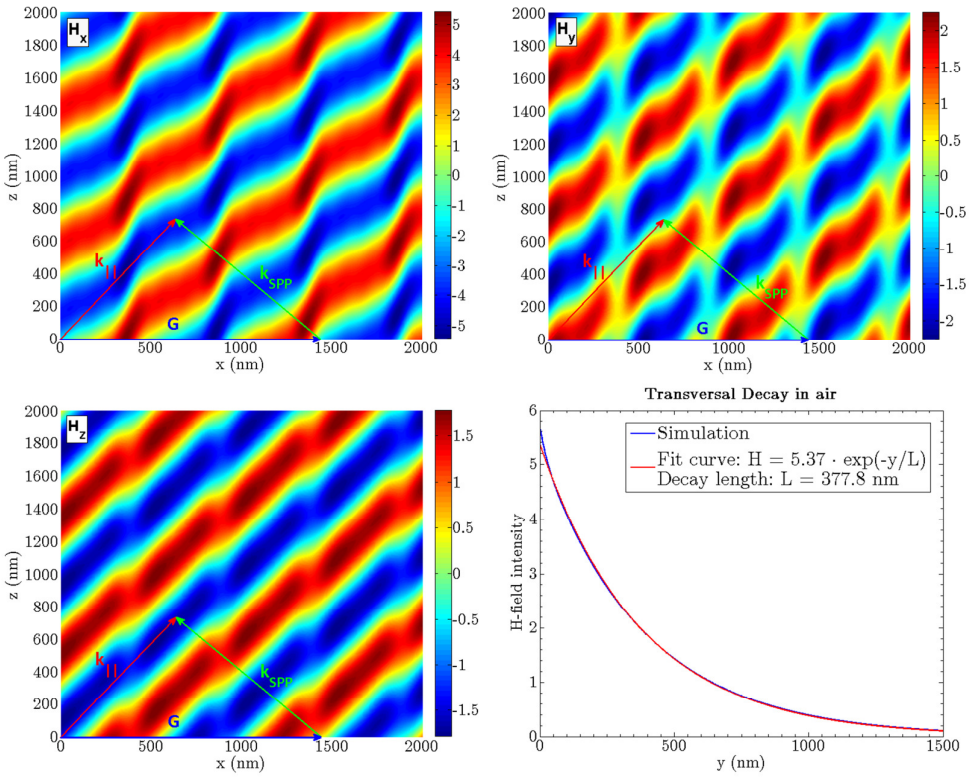

Figure 3-14: Magnetic- field component calculation on the grating surface at SPP resonance condition for $\lambda = 632$ nm, azimuth $\varphi = 53.5°$, polarization $\alpha_{\min} = 158°$, resonance polar angle $\theta_{res} = 70.21°$ (I dip) . Vector sum of eq. (2.2.1) is superimposed to each graph. Magnetic field intensity as a function of the distance from grating surface into air: fit curve and estimated extinction length L .

3.4 Conclusions

A numerical code has been implemented in MATLAB environment, which exploits Chandezon's method for a rigorous solution of metallic gratings diffraction problem. The written routines overcome vectorial method limitations and provide a rigorous calculation of diffraction orders intensity.

The existence of amplitude values and layer thicknesses that optimize the optical response has been shown through the optimization process of a sinusoidal bimetallic grating of unknown amplitude and silver thickness.

Polarization phenomenology with azimuthal rotation has been numerically studied and deepened with an analysis of the resonance dip dependence on incidence angles.

The reflectivity response of a real sample has been simulated and results are well-fitted by experimental data, proving the efficiency and the reliability of the implemented algorithms.

Numerical simulations exhibit their most peculiar feature in the computation of the plasmonic electromagnetic-field on the metal surface. This remarkable result offers a near-field point of view of the phenomenology which far-field experimental techniques cannot provide. The display of plasmonic wave-fronts propagating on the grating surface, confirms out-of-scattering plane propagation and the generic polarization state of these modes in the conical mounting.

4 Experimental: nanofabrication and characterization

4.1 Introduction

Modern nanotechnology has provided a wide range of instrumentation and techniques for the realization of multi-layered patterned structures for plasmonic applications. In this chapter several techniques for the nanofabrication of metallic periodic surfaces are presented: interferential lithography, soft-lithography for grating-replica process, focused ion beam lithography. All these techniques have been approached and exploited during this thesis work for the fabrication of plasmonic gratings. Afterwards we describe the techniques that we used for the optical and physical characterization of grating quality, performance and response.

A microfluidic cell has been realized by soft-lithography and has been embodied to grating samples. By analizing the resonance shift for an increasing concentration of solution flowing through the cell, it is possible to calibrate the sensing device and get an estimation of its resolution and sensitivity to refractive index change.

Further studies of grating functionalization with self-assembled monolayers have been performed. In particular, we analysed the optical response to functionalization with thiolate molecules, in our case alkanethiols, that bind to the gold surface in the form of a compact thin monolayer thanks to the great affinity of the sulphur group with gold. A more complex functionalization is offered by poly(ethyleneoxide), that is well-known for its anti-fouling property which provides the proper resistance to non-specific protein adsorption. PEO-buffer layers have been deposited on gratings and the resulting sensing platform has been characterized.

A section dealing with the fabrication and characterization of nanoporous gold films closes this chapter. This nanostructured material, thanks to the concomitance of a great surface-to-volume ratio and the tunable plasmonic behaviour in the near-infrared, reveals promising features for the realization of patterned surface for sensing applications (see chapter 5).

4.2 Nanofabrication of Metallic Gratings

4.2.1 Interferential Lithography

Interferential Lithography (IL) is the preferred method for the fabrication of periodic patterns that must be spatially coherent over large areas. It is a conceptually simple process where two coherent beams interfere in order to produce a standing wave which can be recorded over a sensitive substrate. The spatial period of the pattern can be as low as half the wavelength of the interfering light, allowing for structures down to about 100 nm using UV radiation.

The wave incident on the recording layer is given by the interference of two coherent waves generated by similar monochromatic sources (same wavelength λ), but different travel paths $\left(\boldsymbol{k}_1 \neq \boldsymbol{k}_2\right)$, and their intereference gives rise to a standing wave of dark and bright intensity fringes in correspondence of interference minima and maxima:

$$I \sim \left|\boldsymbol{E}\right|^2 \sim E_0^2 \cos\left(\frac{4\pi}{\lambda}\sin\theta \cdot x\right) \tag{4.2.1}$$

where θ is the incidence angle, x a coordinate on the sample plane, E_0 the amplitude of the incident electric fields. The illuminated substrate is usually a photoresist, a material that changes its solubility in a particular solvent, known as developer, after being exposed to radiation in a specific range. A photoresist film is usually spread over a substrated, e.g. glass or silicon wafer, with a spin coating procedure: an excess amount of resist solution is placed over the substrate which is then rotated at high speed until the fluid is spread on the surface and the desired thickness is achieved.

As eq. (4.2.1) shows, the period Λ of the standing wave is a function of the incident wavelength λ and of half the angle at which the two beams intersect θ:

$$\Lambda = \frac{\lambda}{2\sin\theta} \tag{4.2.2}$$

Thus the smallest grating periodicity Λ_m is limited by the wavelength λ of the light source and the resolution of the resist layer: $\Lambda_m \sim \lambda / 2$. The recorded pattern reproduces

the exposing standing waves and thus records an almost sinusoidal profile, depending on resist resolution. When more than one exposure is done, a wide variety of periodic structures is allowed to be patterned.

Two-beams interference is preferred because of its simplicity and because it can be done on very large areas, however the main limitation of this technique is that only a 1D periodic pattern can be exposed at once. IL offers advantages over several lithographic techniques such as Electron Beam Lithography (EBL) or Focused Ion Beam (FIB) due to its ability to define patterns over large areas in a single, fast, maskless exposure.

In Lloyd's Mirror Interferometer[60], one source is simply replaced by a 90° mirror. Lloyd's mirror is rigidly fixed perpendicular to the surface and used to reflect a portion of incident wavefront back to the other half (Figure 4-1). The angle of interference and thus the grating periodicity are set just by rotating the mirror/substrate assembly around the point of intersection between the mirror and the substrate. Simple trigonometry guarantees that the light reflected off the mirror is always incident at the same angle as the original beam. Thus in Lloyd's mirror only a single beam is used, moreover since the mirror is fixed with respect to the substrate, vibration of the setup or wandering of the incoming beam do not affect the exposure: this results in a more stable configuration and prevents the need of phase locking systems. Furthermore it allows to change and control grating period without any alignment or critical adjustment between two different sources and thus the system is very convenient to calibrate and tune.

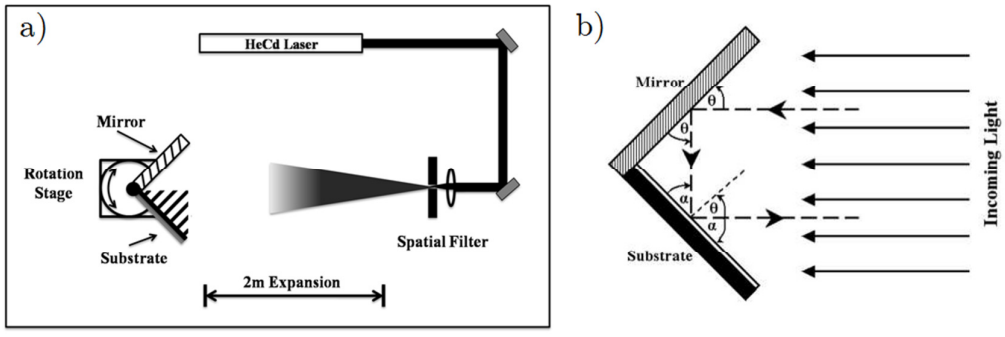

Figure 4-1: a) Lloyd's mirror setup for Interference Lithography. b) Lloyd's mirror in details.

The basic principles in order to record a pattern of desired period and amplitude are the following:

- **Grating period:** the incident beam angle has to be properly adjusted in order to obtain the desired peridicity. It is only necessary to rotate the mirror in order to set the corresponding incidence angle.
- **Grating amplitude:** amplitude is controlled by varying the distance of the mirror from the beam source, in order to control the intensity incident on the sample. The higher the intensity on the resist, the higher the amplitude that is obtained after resist development.

It is worth considering that the flatness and cleanliness of the mirror are very critical otherwise the fabricated grating could be easily distorted. Many sources of laser beam disturbance during the exposure time could lead to a blurring or a loss of resolution on the exposed surface, e.g. the intrinsinc laser instability or environmental vibrations that cause movements of mechanical and optical components. All these effects induce vibration modes which can affect interference fringes in different ways: fringe drifting and pitch blurring. In the case of Lloyd's mirror setup, small vibrations of the assembly do not cause fring drift as the image source created by the mirror automatically compensates the noise. However, a relative motion of the point-source with respect to the interferometer may induce pattern distortions. Since a change in the incident angle between beam and interferometer is related to a change in periodicity, the fluctuation of the fringe period during the exposure may cause contrast and resolution losses. The pin-hole vibration, that could induce a laser beam drift of several microns after 1 m of beam propagation, is mainly due to clean room air flux that impinges on the optical table. For this reason the whole setup has been properly enclosed in damping boxes that are set closed only when the system is running and kept open during the rest of the time.

In our system a 50 mW Helium-Cadmium (HeCd) laser emitting TEM_{00} single mode at 325 nm was used as light source. After a 2 m long free-space propagation, the expanded laser beam illumintes both the sample and the perpendicular mirror. The designed sample holder

offers translational and rotational degrees of freedom, while a rigid mechanical connection between the mirror and the sample-chuck prevents phase distortion. The possibility to translate the sample stage in two directions allows a fine positioning of the system in the zone where the Gaussian beam distribution reaches its maximum and the best conditions in terms of beam intensity, uniformity and spatial coherence are achieved. On the other hand the sample stage rotation around vertical axis, with 8 mrad resolution, allows a fine setting of fringes periodicity.

The IL fabrication process of the metallic gratings performed in this work proceeded through a sequence of steps[61,62]: resist spinning, IL exposure, resist devolpment, methal evaporation. Exposures were performed over silicon samples of 2×2 cm^2 surface area. Silicon wafers were pre-baked for $20 - 30$ minutes at $120°$ C. A bottom coating (XHRiC-11, BARC) was spun (5000 RPM, 30 seconds) in order to obtain a 100 nm-thick anti-reflection layer. After a soft baking step ($175°$ C for 1 minute) the substrate was coated with a 100 nm thick film of photoresist S1805 (Microposit, Shipley European Limited, U.K.) and Propylene glycol monomethyl ether-1,2-acetate (PGMEA) solution (ratio 2:3) at the spinning rate 6000 RPM for 30 seconds. UV exposure was performed with a laser incidence angle of $19°$ and a constant integrated exposure dose 80 mJ/cm^2 for sinusoidal grating with period ~ 500 nm and amplitude ~ 30 nm. Thereafter a developing solution of MICROPOSIT MF-319 and water in ratio 10:1 was used.

After the exposed resist has been developed, the result is a photonic crystal: a dielectric periodic surface which has no plasmonic feature yet. In order to realize a plasmonic crystal, the dielectric grating must be coated with a metallic layer of proper thickness. The fabricated metallic gratings have been realized by thermal evaporation. This technique is based on the boiling off or sublimation of heated pieces of metal onto a substrate in a vacuum chamber ($10^{-6} - 10^{-7}$ torr). The metal target is usually evaporated by passing a high current (about $100 - 150$ A) through a highly refractory-metal containment structure (boat), e.g. molibdenus boats for silver, tungsten boats for gold. The containment structure in fact must be made of a metal with a fusion temperature higher than the evaporating metal. This method is called

resistive heating. Evaporated metal condenses on the sample into a growing metal layer. By varying current intensity the deposition rate can be controlled: a typical rate is in the order $0.1 - 0.3$ nm/s.

4.2.2 Soft Lithography: grating replica

Soft-lithography is a useful technique in order to replicate pre-fabricated patterns with a nanometric resolution. It consists in making at first the negative replica of a pattern master onto a siliconic polymer and then in imprinting this pattern onto a photopolymeric substrate that cures when exposed to UV light (see Figure 4-2).

In principle, a plasmonic grating could be obtained, as explained in the previous section, by simply coating a developed resist surface with specific noble metals, such as silver and gold over few nanometers of chromium or titanium as adhesion layers. However, many bio-molecular surface functionalization methods involve the use of organic solvents that may attack the photoresist pattern. To avoid this problem, a replica molding approach was adopted in order to produce thiolene copies of the gratings. Commercial thiolene resin (Norland Optical Adhesive[63] – NOA61) was used in order to exploit its relatively good resistance to organic solvents.

Resist patterns were replicated onto the thiolene resist film supported on microscope glass slides using polydimethylsiloxane (PDMS) molds. The latter were obtained by replicating the resist grating masters using RTV615 silicone. Base and catalyst of the two component silicone were mixed 10:1 ratio and degassed under vacuum (Figure 4-2.a). The PDMS was then cast against the resin masters and cured at 60° C, well below the resist post-exposure bake temperature (115° C) in order to prevent the resist pattern from distortion (Figure 4-2.b) and after 2 hours the PDMS was peeled off from the resist master (Figure 4-2.c).

In order to obtain rigid and stable supports, the PDMS molds were bounded to glass slides by exposing the flat backside of the PDMS mold and the glass slide to oxygen plasma before contacting them. The PDMS mold was then used to UV imprint the initial pattern onto a drop of NOA61 resin dripped on top of a glass slide by just slightly pressing the mold onto the liquid resin and exposing it to the UV light (365 nm) of a Hg vapor flood lamp

(Spectroline SB-100P) at a distance of about 10 cm for 20 minutes (Figure 4-2.d-f). After removing the PDMS mold, the replicated NOA61 grating can be coated with metal layers by thermal evaporation.

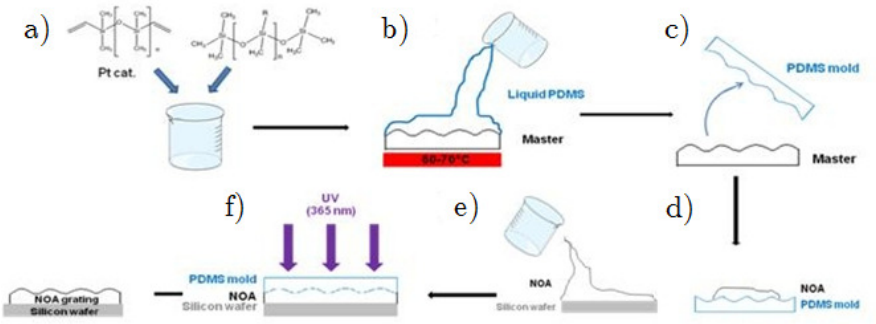

Figure 4-2: scheme of soft-lithography process for grating replica.

4.2.3 Focused Ion Beam (FIB) Lithography

FIB lithography uses a collimated and focused beam of accelerated ions that directly hit the sample surface and sputter a small amount of material[64]. Depending on the accelerating voltage and on the selected ion current, sample surface is milled and the desired pattern is recorded on the exposed area. Since this technique consists in directly milling the exposed surface, grating profile which is usually obtained by performing FIB lithography on a metal surface is almost digital, with amplitude values strictly related, at a fixed accelerating voltage, to current intensity and exposition time.

FIB instrument consists of a source for the generation of the ion beam, an accelerating, focusing and scanning system of electromagnetic lenses, a vacuum chamber directly connected to the ion column, where the sample is located and exposed. The use of an ion beam provides an interaction with the exposed area that is limitated to its surface: ions interact and remove surface atoms, and dwell time and size are controlled with great resolution down to a nanometer scale. Since the exposed surface is scanned with a nanometric-size writing spot, FIB lithography requires much longer times than interferential lithography. However FIB technique provides higher resolution on lithography and a complete control on pattern design.

In this work FIB lithography was performed by means of the gallium ion source (Ga^+) of the dual beam system FEI Nova 600i instrument. This system guarantees a resolution down to 5 nm for an accelering voltage of 30 kV. Ion beam can be selected in the range from 1.5pA up to 20 nA. This instrument also provides an Energy-Dispersive X-ray spectroscopy (EDX) analysis system for the elemental and chemical analysis of the sample. The stimulated emission of characteristic X-rays from the specimen is produced by the high-energy ion or electron beam that is focused on the sample. Since an X-ray energy pattern is characteristic of the energy difference between electron shells and thus of the element from which they are emitted, this allows the elemental composition of the inspected target to be detected and estimated. Energy-peak intensity provides information on the relative percentages of the detected elements.

4.3 Optical characterization

4.3.1 Scanning Electron Microscopy (SEM)

Scanning eletron microscope images the sample surface by scanning it with a high energy electron beam[65]. Electrons interact with the atoms that compose the sample and produce signals that yield information about target surface topography, composition and physical properties such as electrical conductivity. Primary electrons are emitted by thermionic emission from a metallic filament cathode (usually tungsten or lanthanum hexaboride) or by a thermal field emission tip (Schottky emitter) and are accelerated towards an anode. The electron beam, with energy typically from a few hundred eV up to 30 keV, is focused by a system of condenser lenses into a beam with a very fine local spot sized 0.4 nm to 5 mm. The electron beam passes through pairs of scanning coils or pairs of deflector plates in the electron column which deflect the beam horizontally and vertically so that it scans in a raster fashion over a rectangular area of the sample surface. Both the column and the target chamber are under high vacuum ($10^{-6} - 10^{-7}$ mbar) in order to avoid electron scattering by air molecules. When primary electrons interacts with the target, they loss energy by repeated scattering and adsorption within a teardrop-shape volume (interaction volume), which

extends from less than 100 nm to around µm into the surface. The size of the interaction volume depends on the electron energy and atomic number and density of the target. The interaction between primary electrons and sample results in the back-reflection of high-energy electrons by elastic scattering, production of secondary electrons by inelastic scattering and emission of electromagnetic radiation. The most common imaging technique consists in collecting the low-energy secondary electrons ($E < 50\,\mathrm{eV}$). These electrons originate within a few nanometers from the surface and are usually detected by an Everhart-Thornley detector which is a type of scintillator-photomultiplier device. The resulting signal is displayed as a two-dimensional intensity distribution. The brightness of the signal depends on the number of secondary electrons reaching the detector: if the beam enters the sample perpendicularly to the surface, the activated region is uniform around the axis of the beam and a certain number of electrons are emitted. As incidence angle increases, the escape distance of one side of the beam will decrease and more secondary electrons will be emitted. In this way steep surfaces and edges tend to be brighter than flat zones, which results in images with a well-defined, three-dimensional appearance. The spatial resolution depends on the size of the electron spot, which is related to the electron energy and the focusing system and it can be also limited by the size of the interaction volume. In our case, resolutions down to few nanometers can be achieved.

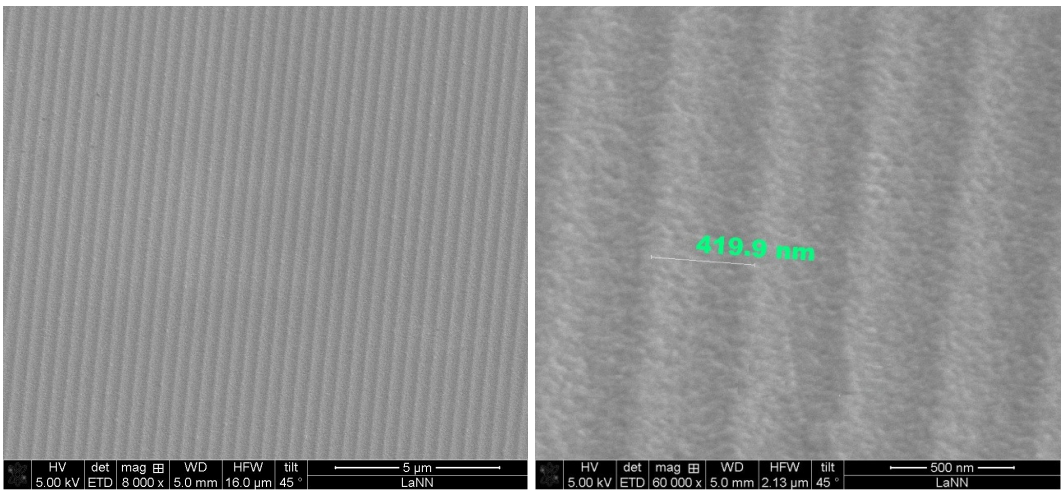

Figure 4-3: SEM inspections of a gold metallic grating, period $\sim$ 420 nm, amplitude $\sim$ 30 nm.

Figure 4-3 refer to SEM analysis of a gold grating with period of about 420 nm and amplitude 30 nm, fabricated by interferential lithography. A considerable homogeneity over μm size is appreciable. Inspections have been performed with the electron column of the dual beam system FEI Nova 600i.

4.3.2 Atomic Force Microscopy (AFM)

Atomic Force Microscopy (AFM) consists in a scanning technique that produces very high resolution 3D images of sample surfaces[64,65]. This technique can be used either in a static or a dynamic mode. In the static mode, the sharp tip at the end of a cantilever is bought in contact with the sample surface. During initial contact, atoms at the end of the tip experience a very weak repulsive force due to orbital overlap with atoms on the sample surface. This force causes a cantilever deflection which is measured by optical detectors. Deflection can be measured to within 0.02 nm, so for typical cantilever spring constant of 10N/m, a force as low as 0.2 nN can be detected. In the dynamic operation mode instead, the tip is bought in close proximity (within a few nms) to and not in contact with the sample. The cantilever is deliberately vibrated either in amplitude modulation (AM) or in frequency modulation (FM) mode. Very weak Van Der Waals attractive forces are present at the tip-sample interface. In the two modes, surface topography is measured by laterally scanning the sample under the tip while simultaneously measuring the cantilever deflection or the shift in resonant frequency/amplitude of the cantilever. Piezo-translators are used to scan the sample or alternatively to scan the tip. A cantilever with extremely slow spring constant is required for high vertical and lateral resolutions at small forces, but at the same time a high resonance frequency is desiderable (from 10 to 100 kHz) in order to minimize the ratio to vibration noise. This requires a tip with extremely low vertical spring constant (typically from 0.05 to 1 N/m) as well as a low mass (in the order of 1 ng). Common cantilevers are fabricated in silicon, silicon oxide or silicon nitride and lateral dimensions are in the order of 100 μm with thickness of about 1 μm. Tip is required to be robust and have a small curvature radius ($\sim 10\,\text{nm}$). The cantilever deflection is measured by means of an optical laser system. The beam is directed onto the back of the cantilever very close to its free end, while the reflected

beam is directed onto a quad-photodetector, i.e. two pairs of photodiodes. The differential signal from the different photodiodes provides information on the cantilever deflection. In the dynamic mode, the cantilever is driven into oscillations near its resonance frequency. When the tip approaches the sample, the oscillation is damped, frequency and phase change. The variation is the feedback signal and topography is given by varying the z-position of the sample in order to keep amplitude oscillations constant or the resonance frequency fixed. Figure 4-4 and Figure 4-5 refer to AFM analysis with VEECO D3100 Nanoscope IV of a bimetallic sinusoidal grating fabricated by interferential lithography. The sharp Fourier spectrum in Figure 4-5 supports the approximation of the grating profile with a perfect sinusoid.

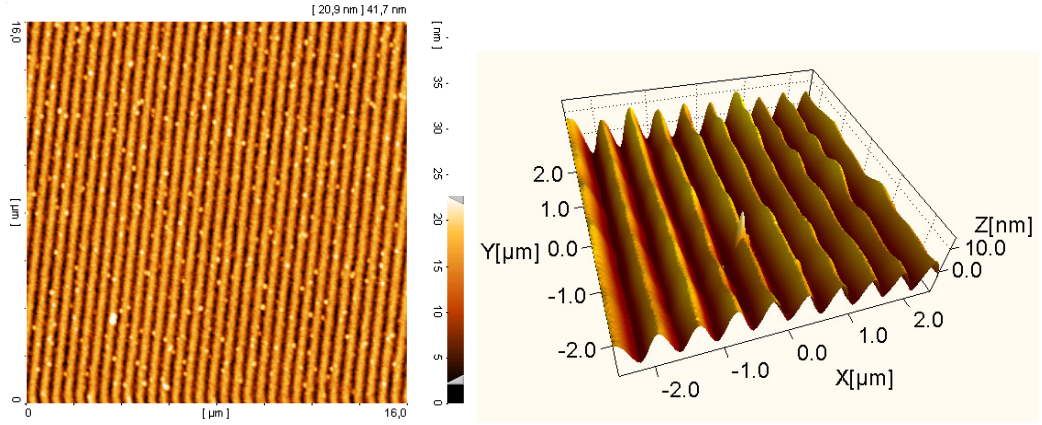

Figure 4-4: AFM analysis of a sinusoidal metallic grating, period $\sim$ 500 nm, and 3D reconstruction.

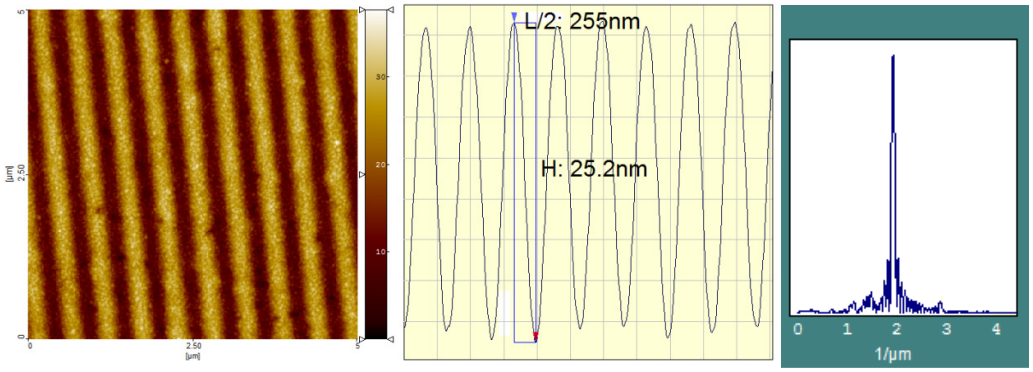

Figure 4-5: AFM analysis, profile and Fourier weights of a periodic gold grating: period $\sim$ 500 nm, amplitude $\sim$ 25 nm, roughness rms $\sim$ 1.2 nm.

4.3.3 Spectroscopic Ellipsometry

Ellipsometry is a useful technique for the study of optical and geometrical properties of thin films[66]. It is a non-destructive optical characterization based on the analysis of the polarization state of light reflected by sample surface. By analyzing the polarization of the reflected beam, information about thickness and refractive index of thin films can be obtained.

In this work spectroscopic measurements have been performed by means of the spectroscopic ellipsometer VASE (J. A. Woollam), with angular and spectroscopic resolution respectively $0.01°$ and $0.3\,\text{nm}$. This setup consists in a Xenon-Neon lamp (75W) as a light source with a monochromator and focusing system that allow selecting wavelengths in the range $270 - 2500\,\text{nm}$. Polarization state is controlled with a first polarizer and the output light that hits the sample is reflected into a detector arm, consisting in a rotating polarizer (analyzer) and a photodiode system for signal conversion and amplification. This instruments performs Rotating-Analyzer Ellipsometry (RAE) analysis. RAE was perfected by Aspnes at al.[67] in 1975. In 1990, a group from the Pennsylvania State University first developed a real-time instrument that utilized a photodiode array as a light detector[68]. In order to overcome the disadvantages of RAE, a compensator was first added by Roseler et al.[69] in 1984.

The typical result of an ellipsometric analysis is expressed in term of the ellipsometric angles ψ and Δ which are defined from the ratio of the amplitude reflection coefficients[70] (Fresnel's coefficients) for *p*- and *s*-polarization:

$$\rho = \frac{r_p}{r_s} = \tan\psi \cdot e^{i\Delta} \tag{4.3.1}$$

Therefore ψ represents the angle between reflected *p*- and *s*-polarizations, while Δ expresses the phase difference:

$$\begin{aligned} \tan\psi &= \frac{\left|r_p\right|}{\left|r_s\right|} \\ \Delta &= \delta_{rp} - \delta_{rs} \end{aligned} \tag{4.3.2}$$

Thus common ranges for ellipsometric angles are $0^\circ \le \psi \le 90^\circ$ and $0^\circ \le \Delta \le 360^\circ$.

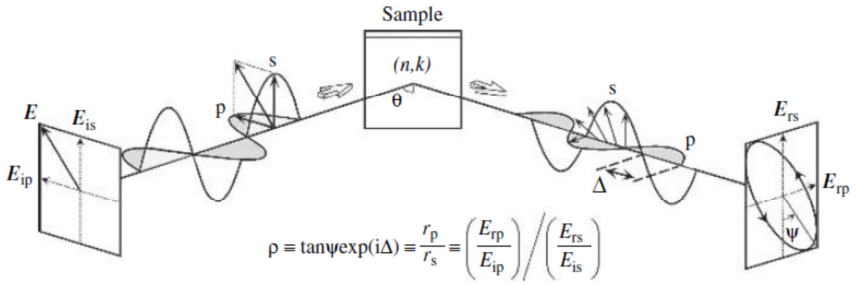

Figure 4-6: measurement principle of spectroscopic ellipsometry.

Ellipsometry measurement can be expressed in terms of Jones matrices of polarization states and polarizer elements[71,72]. By examining the RAE setup using Jones formalism, the ellipsometric instrument with polarizer-sample-analyzer (PSA_R) configuration is expressed as:

$$\boldsymbol{L}_{out} = AR(\alpha)SR(-\beta)P\,\boldsymbol{L}_{in} \tag{4.3.3}$$

where $\boldsymbol{L}_{out}$ represents the Jones vector of the light recorded by the detector and is given by:

$$\boldsymbol{L}_{out} = \begin{bmatrix} E_A \\ 0 \end{bmatrix} \tag{4.3.4}$$

$\boldsymbol{L}_{in}$ represents the normalized Jones vector corresponding to normalized incident light:

$$\boldsymbol{L}_{in} = \begin{bmatrix} 1 \\ 0 \end{bmatrix} \tag{4.3.5}$$

The parameter α of the rotation matrix $R(\alpha)$ represents the rotation angle of the analyzer, while β is the angle of the polarizer. In order to express the light transmission through the polarizer, we first rotate the coordinates so that the transmission axis of the polarizer becomes parallel to the E_{ip} axis. After the light passes through the polarizer (P), the coordinates are rotated again towards the reverse direction to restore the coordintes back into the original position. In Jones matrix formalism, this is expressed by $R(-\beta)PR(\beta)$. Nevertheless, the Jones vector cannot describe unpolarized (natural) light. Thus, with respect

to the light emitted from a light source, only the light transmitted by the polarizer P is taken into account and the rotation matrix $R(\beta)$ can be neglected. Similarly the rotation matrix $R(-\alpha)$ is eliminated from $R(-\alpha)AR(\alpha)$ since light transmitted through the analyzer (A) is detected independently of the coordinate rotation.

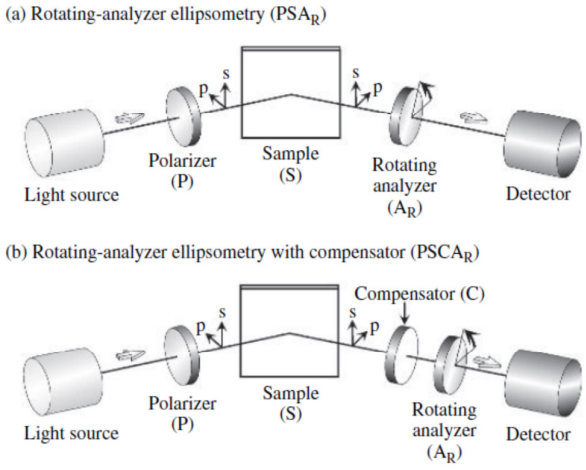

Figure 4-7: optical configuration of ellipsometric instruments in rotating analyzer setup (RAE) with (a) or without (b) a compensator.

In matrix representation, eq. (4.3.3) becomes:

$$\begin{bmatrix} E_A \\ 0 \end{bmatrix} = \begin{bmatrix} 1 & 0 \\ 0 & 0 \end{bmatrix} \begin{bmatrix} \cos\alpha & \sin\alpha \\ -\sin\alpha & \cos\alpha \end{bmatrix} \begin{bmatrix} \sin\psi e^{i\Delta} & 0 \\ 0 & \cos\psi \end{bmatrix} \begin{bmatrix} \cos\beta & -\sin\beta \\ \sin\beta & \cos\beta \end{bmatrix} \begin{bmatrix} 1 & 0 \\ 0 & 0 \end{bmatrix} \begin{bmatrix} 1 \\ 0 \end{bmatrix} \tag{4.3.6}$$

where the Jones matrix S corresponding to light reflection by the sample is given by [iv]:

$$S = \begin{bmatrix} r_p & 0 \\ 0 & r_s \end{bmatrix} = r_s \begin{bmatrix} \rho & 0 \\ 0 & 1 \end{bmatrix} = \frac{r_s}{\cos\psi} \begin{bmatrix} \sin\psi e^{i\Delta} & 0 \\ 0 & \cos\psi \end{bmatrix} \tag{4.3.7}$$

The proportional constant $(r_s / \cos\psi)$ in previous equation can be neglected, since only relative changes are taken into account in ellipsometry measurements. Thus eq. (4.3.6) is reduced to:

$$\begin{bmatrix} E_A \\ 0 \end{bmatrix} = \begin{bmatrix} 1 & 0 \\ 0 & 0 \end{bmatrix} \begin{bmatrix} \cos\alpha & \sin\alpha \\ -\sin\alpha & \cos\alpha \end{bmatrix} \begin{bmatrix} \sin\psi e^{i\Delta}\cos\beta \\ \cos\psi\sin\beta \end{bmatrix} \tag{4.3.8}$$

[iv] The Jones matrix S in eq. (4.3.7) represents the light reflection by an optical isotropic sample. When a sample shows optical anisotropy, such as birifrangence or dicroism, the generalized Jones matrix has non-zero off-diagonal elements r_{ps} and r_{sp}.

By expanding eq. (4.3.8) we get:

$$E_A = \cos\beta\cos\alpha\sin\psi e^{i\Delta} + \sin\beta\sin\alpha\cos\psi \tag{4.3.9}$$

And light intensity measured by the detector results:

$$I = \left|E_A\right|^2 = I_0\left(1 + S_1\cos 2\alpha + S_2\sin 2\alpha\right) \tag{4.3.10}$$

where S_1 and S_2 are given by:

$$\begin{aligned} S_1 &= \frac{\cos 2\beta - \cos 2\psi}{1 - \cos 2\beta\cos 2\psi} \\ S_2 &= \frac{\sin 2\psi\cos\Delta\sin 2\beta}{1 - \cos 2\beta\cos 2\psi} \end{aligned} \tag{4.3.11}$$

Thus light intensity varies as a function of the analyzer angle 2α. In RAE, the Stokes parameters S_1 and S_2 are measured as the Fourier coefficients of the harmonic terms in 2α. If the analyzer rotates continuously with time at a speed of $\alpha = \omega t$, where ω is the angular frequency of the analyzer, we can express the light intensity as a function of time as follows:

$$I(t) = I_0\left(1 + \gamma_1\cos 2\omega t + \gamma_2\sin 2\omega t\right) \tag{4.3.12}$$

By transforming $\cos 2\beta, \sin 2\beta, \cos 2\psi, \sin 2\psi$ using double-angle formulas, we get the well-known forms for the normalized Fourier coefficients:

$$\begin{aligned} \gamma_1 &= \frac{\tan^2\psi - \tan^2\beta}{\tan^2\psi + \tan^2\beta} \\ \gamma_2 &= \frac{2\tan\psi\cos\Delta\tan\beta}{\tan^2\psi + \tan^2\beta} \end{aligned} \tag{4.3.13}$$

Solving for the ellipsometric angles ψ and Δ we finally get the following equations:

$$\begin{aligned} \tan\psi &= \sqrt{\frac{1+\gamma_1}{1-\gamma_1}}\left|\tan\beta\right| \\ \cos\Delta &= \frac{\gamma_2}{\sqrt{1-{\gamma_1}^2}} \end{aligned} \tag{4.3.14}$$

In spectroscopic ellipsometry with RAE configuration, ellipsometric angles (ψ,Δ) are extracted from the Fourier coefficients (γ_1,γ_2) using eq. (4.3.14). In this method therefore, the polarization state of reflected light is determined from a variation of light intensity with the analyzer angle, thus in principle left-circular polarization cannot be distinguished from right-circular polarization since these states exhibit the same light intensity variation versus the analyzer angle. This is the reason why the measurement range for Δ becomes half: $0^\circ \le \Delta \le 180^\circ$. Moreover it can be demonstrated[73] that the measurement error $\delta\Delta$ as a function of the errors of Fourier coefficients $\left(\delta\gamma_1,\delta\gamma_2\right)$, increases drastically at $\Delta \cong 0^\circ,180^\circ$. A solution to overcome this problem consists in the use of a compensator $\left(C\right)$ before (or after) the sample. In terms of optical matrices and vectors, the sequence is described by:

$$\boldsymbol{L}_{out} = AR(\alpha)CSR(-\beta)P\,\boldsymbol{L}_{in} \tag{4.3.15}$$

where C is given by:

$$C = \begin{bmatrix} e^{-i\delta} & 0 \\ 0 & 1 \end{bmatrix} \tag{4.3.16}$$

In previous description the fast axis of the compensator has been chosen in the direction of *s*-polarization, rather than *p*-polarization, and the consequent phase shift δ is a function of wavelength λ. By substituting Jones forms of matrices in eq. (4.3.15), we find out that the compensator introduced into RAE, only shifts the Δ value without any effects on ψ. The compensator does not change the amplitudes of *p*- and *s*-polarizations but changes the relative phase difference between the two. Accordingly, RAE with compensator can be described by simply replacing Δ with $\Delta' = \Delta - \delta$ in the equations previously derived. If we replace Δ with Δ' in eq. (4.3.9), we obtain:

$$I = \left|E_A\right|^2 = I_0\left(1 + S_1\cos 2\alpha + \left(S_2\cos\delta - S_3\sin\delta\right)\sin 2\alpha\right) \tag{4.3.17}$$

By performing at least two measurements with different δ (e.g. rotating the compensator axis), it is possible to obtain the two values S_2 and S_3 separately[74], and Δ can be determined in the whole range $0^\circ - 360^\circ$. Moreover in RAE measurements with

compensator, since the value Δ' can be shift of the quantity δ, we can correct and eliminate the error observed at $\Delta \cong 0°,180°$.

Once ellipsometric measurement on a sample has been completed and angles (ψ,Δ) have been collected, it is necessary to perform data analysis in order to extract physical information such as either optical constants (n,k) or thickness d of the films that constitute the analyzed stack. Thus a model of the dielectric function of the sample is necessary in order to fit experimental data and get an estimation of the optical properties that are left as free parameters.

Following ellipsometric data and fit results (sample 1, 2) refer to the analysis of the typical stacks that constitute the metallic gratings realized by interferential lithography and soft-lithography techniques. A small part of the sample is usually left unpatterned during the process and ellipsometric analysis is finally performed on this flat zone in order to get an estimation of the thicknesses of the several metallic and dielectric layers deposited on the substrate. The optical constants of each material have been measured separately by performing ellipsometric analysis of a single layer deposited over a known substrate. In this way the complex refractive index $n+ik$, or the complex dielectric permettivity $\varepsilon_1+i\varepsilon_2$ equivalently, have been estimated for the employed materials: metals (gold, silver, chromium), resist Shipley1805, NOA61 resin, glass substrate and silicon wafer.

Sample 1. *Silicon substrate*. Metallic grating fabricated by interferential lithography of a resist layer (Shipley1805). Optimized thicknesses of silver and gold have been thermally evaporated over (*nominally* 37 nm Ag coated by 7 nm of Au).

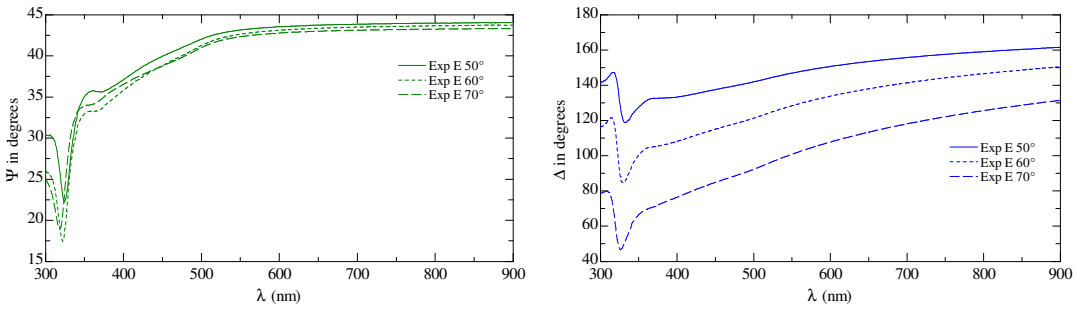

Figure 4-8: ellipsometric angles ψ and Δ of the flat multilayered stack of sample 1: Ag/Au layer over a dielectric film (resist Shipley1805) on a silicon substrate. Experimental data: spectroscopic ellipsometry in the range $300-900$ nm, step size 10 nm, incidence angles $50°-60°-70°$.

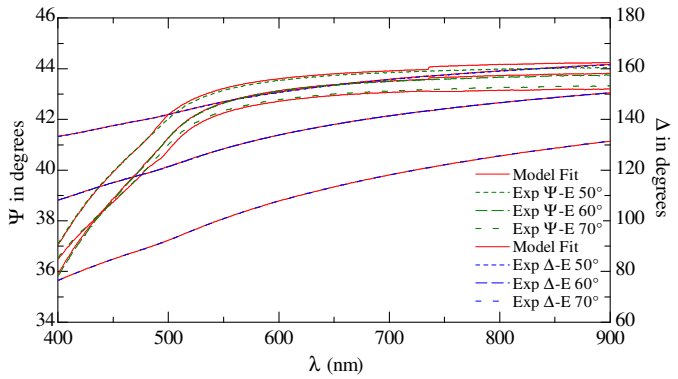

Figure 4-9: ellipsometric angles ψ and Δ of the flat multilayered stack of sample 1: a bimetallic Ag/Au coating over a dielectric film (resist Shipley1805) on a silicon substrate. Experimental data and fit curves (red lines)

Table 4-1: results from fit of ellipsometric data in Figure 4-9, RMSE = 1.8.

roughness	0.58 ± 0.02
Au	5.31 ± 0.09
Ag	38.26 ± 0.24
resist	85.16 ± 0.42
SiO_2	2.12 ± 0.18
substrate (Si)	

Sample 2. *Resin (NOA61) substrate*, over a glass support. Metallic grating fabricated by soft-lithography replica of a pre-fabricated master. An optimized thickness of gold has been thermally evaporated over a thin adhesion film of chromium (*nominally* 40 nm Au, 5 nm of Cr).

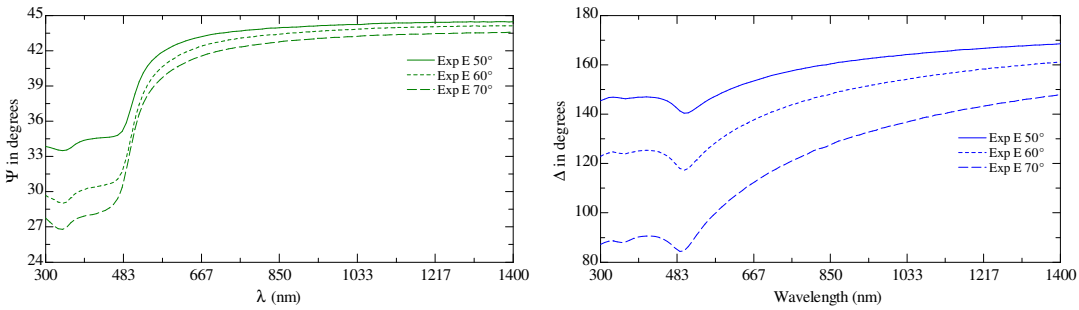

Figure 4-10: ellipsometric angles ψ and Δ of the flat multilayered stack of sample 2: a gold film over a chromium adhesion layer (resist Shipley1805) on a dielectric substrate (NOA61 resin on glass). Experimental data: spectroscopic ellipsometry in the range $300 - 1400$ nm, step size 10 nm, incidence angles $50° - 60° - 70°$.

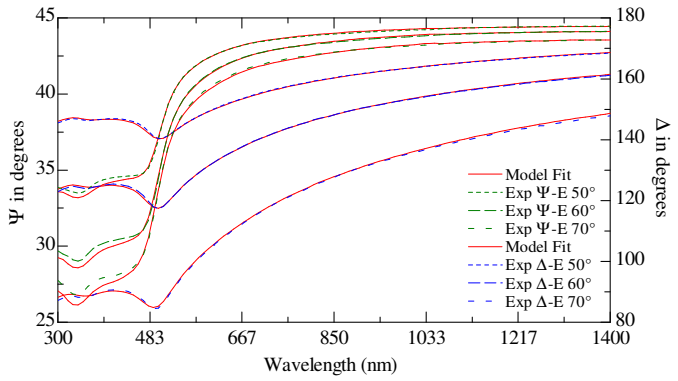

Figure 4-11: ellipsometric angles ψ and Δ of the flat multilayered stack of sample 2: a gold film over a chromium adhesion layer (resist Shipley1805) on a dielectric substrate (NOA61 resin on glass). Experimental data and fit curves (red lines).

Table 4-2: results from fit of ellipsometric data in Figure 4-11, RMSE = 2.1.

roughness	0.70 ± 0.03
Au	38.99 ± 0.16
Cr	3.41 ± 0.09
substrate (NOA61)	

Ellipsometry simulation. An ellipsometry analysis on patterned zones, exhibits the characteristic resonance features related to surface plasmon excitation. Figure 4-12 refer to the sinusoidal grating on sample 2, with period 502 nm, amplitude 27 nm. Simulation curves from the numerical approach with C-method (chapter 3), well fit the experimental data:

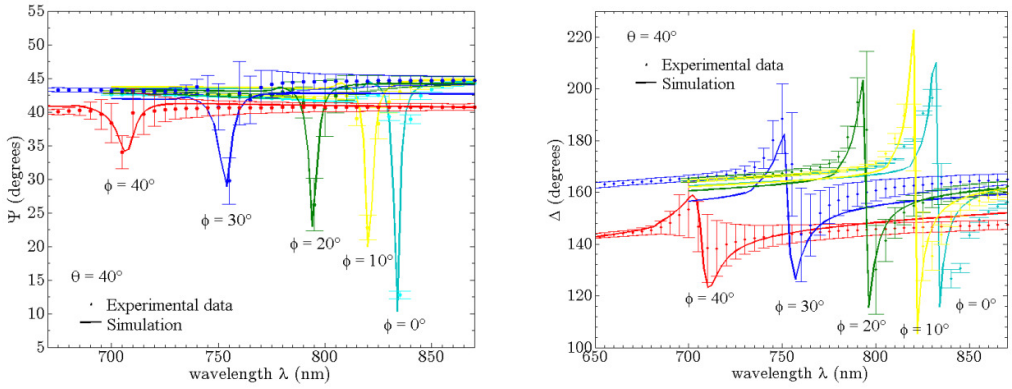

Figure 4-12: ellipsometric angles Ψ and Δ for a sinusoidal bimetallic grating (sample 2). Experimental data and comparison with numerical calculations based on Chandezon's method. Different azimuthal rotation of the grating support are considered: $\varphi = 0°, 10°, 20°, 30°, 40°$.

While in angular scan, the resonance dip shifts towards greater polar angles for increasing azimuth (cfr. Figure 2-3.a), in wavelength scan instead resonances exhibit an opposite behaviour as expected from eq. (2.3.1).

4.4 Microfluidic cell

4.4.1 Cell fabrication

A glass/PDMS microfluidic cell 400 microns deep and 8 mm wide was built as follows: first a two-level relief mold featuring the channel layout was produced on a microscope glass slide by liquid photopolymerization photolithography using NOA61 (Norland Products) optical adhesive according procedures[75] previously described in the soft-lithography section (4.2.2).

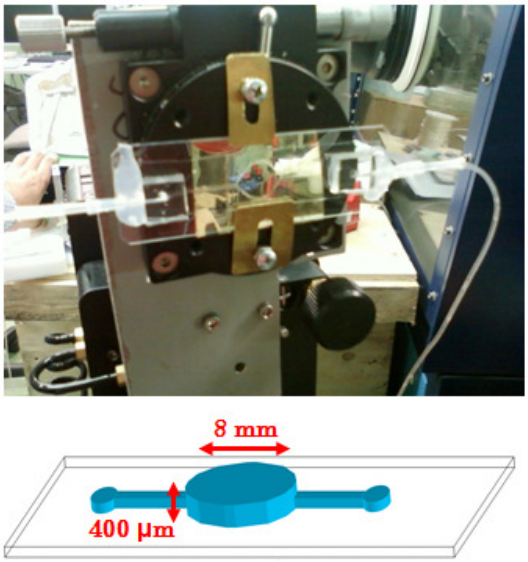

Figure 4-13: picture and scheme of the microfluidic cell.

Polydimethylsiloxane (PDMS) pre-polymer was prepared by mixing GE RTV615 curing agent and base compound in 1:10 ratio. After degassing under vacuum, the pre-polymer was cast onto the mold and a glass slide covered with a polyethilene sheet - acting as an anti-stick layer - was pressed using a weight on top of the PDMS covered mold. Curing was performed on a hotplate at $100°C$ for ca 30 min. The resulting cured PDMS piece represents a rubber gasket with an aperture in the detection zone and inlet ports distant from the

detection zone so that tube connectors can be placed farther apart and do not obstruct the optical path (see Figure 4-13). The PDMS gasket is then oxygen plasma bonded to the glass slide with predrilled inlet/outlet holes. Separately prepared PDMS blocks ($5 \times 5 \times 5\,\mathrm{mm}^3$) with cored tube access holes are plasma bonded on the opposite side of the glass slide in correpondence of the holes in the glass slide. Microbore Tygon tubing (Cole Parmer 0,06" O.D., 0.02" I.D.) is pressure fitted into the holes of the PDMS blocks.

4.4.2 Grating calibration with sodium-chloride solutions

The microfluidic cell was embodied to a fabricated metallic grating and the optical response of the system has been analyzed in reflectivity during the flowing of water solutions with different concentrations of sodium-chloride. Solutions have been prepared by dissolving into 200 ml of water an increasing mass of sodium-chloride up to 50 g, step 10 g.

Reflectivity measurements were collected in a $\theta / 2\theta$ symmetric configuration using ellipsometer VASE monochromatized 75W Xe lamp, for scans of the incidence polar angle with step $0.2°$, fixed wavelength $\lambda = 840\,\mathrm{nm}$. The sample was mounted on a rotation stage for azimuthal rotation with accuracy $0.01°$.

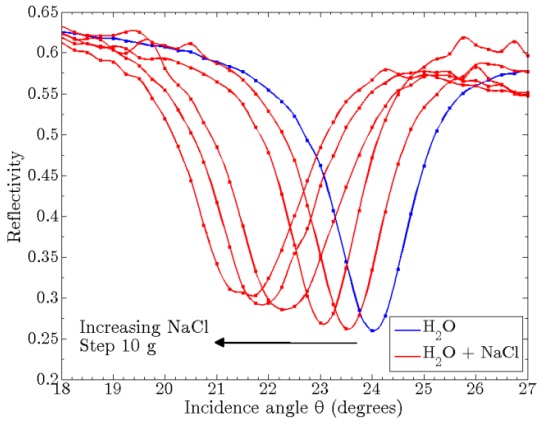

Figure 4-14: Reflectivity in polar angular scan at incident wavelength $\lambda = 840$ nm, null-azimuth, *p*-polarization, for increasing NaCl concentration in water solution: 0-50 g, step 10 g, in 200 ml of water.

A variation in the refractive index n of the medium, results in a change of resonance conditions and thus in a shift of the resonance angle for fixed incident wavelength. Figure 4-14 shows reflectivity spectra in angular scan at the incident wavelength $\lambda = 840\,\mathrm{nm}$ for

increasing concentration of the flowing solution into the cell. Since the refractive index increases for increasing concentration, there is a shift in the resonance dip towards lower angle values, as expected from eq. (2.2.4):

$$\sin\theta_{res} = \frac{\lambda}{\Lambda} - \sqrt{\frac{n^2\varepsilon_m}{n^2+\varepsilon_m}} \cong \frac{\lambda}{\Lambda} - n\sqrt{\frac{\varepsilon_m}{1+\varepsilon_m}} \tag{4.4.1}$$

where we used the approximation $\varepsilon_m \gg n^2$. For each reflectivity curve, resonance angle position has been estimated using a weighted centroid algorithm[27]. Sodium-chloride mass concentration $m\,(\mathrm{g/l})$ in the aqueous solution has been converted in refractive index variation Δn with respect to the initial distilled-water flowing through the cell. The salinity, expressed as grams of salt dissolved in a kilogram of solution, has been converted in refractive index by using tabulated data available in literature[76].

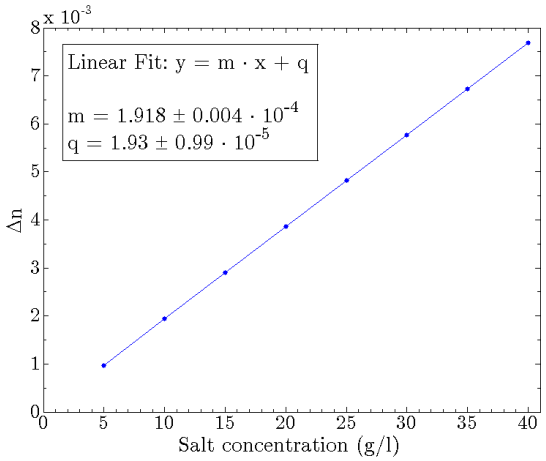

Figure 4-15: refractive index variation as a function of sodium chloride mass concentration in water solution and fit curve (data from Dorsey[76]).

Figure 4-16 exhibits the shift $\Delta\theta$ of the resonance angle as a function of the calculated refractive index variation Δn. A linear fit of the collected data allows estimating the refractive index angular sensitivity $S_{n,\theta}\left[^\circ / RIU\right]$:

$$S_{n,\theta} = \frac{\partial\theta}{\partial n} \tag{4.4.2}$$

The fabricated metallic grating exhibits a sensitivity $S_n = 64.9° / RIU$ for $\lambda = 840$ nm. Sensitivity S_θ can be improved just by an azimuthal rotation of the grating support (see chapter 5, section 5.2.4).

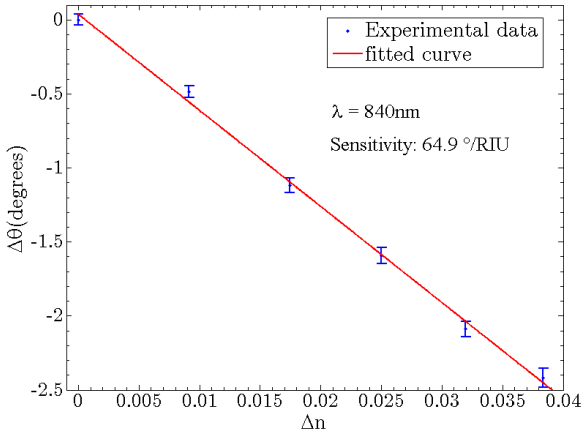

Figure 4-16: Resonance angle shift as a function of refractive index variation of water solution with increasing NaCl concentration, wavelength $\lambda = 840$ nm, null azimuth, *p*-polarization. Linear fit and refractive index sensitivity estimation.

4.5 Functionalization of grating surface

4.5.1 Effective Medium Approximation (EMA) for thin coating films

Once plasmonic gratings have been fabricated with the previously explained techniques, their optical response and refractive index sensitivity have been tested by means of a functionalization of the metal surface with thin self-assembling coating layers. The comparison of reflectivity data before and after functionalization provides information on the change of plasmonic resonances, such as angular $\Delta\theta$ or wavelength $\Delta\lambda$ shifts of dip position. In order to estimate the refractive index sensitivity $S_n = \Delta Y / \Delta n$, where Y could stand for λ or θ, depending on the selected modulation, an estimation of the effective refractive index variation Δn due to a monolayer functionalization is necessary. Once surface plasmon polaritons are excited, the confined electromagnetic field experiences a dielectric medium which is different because of the presence of the adsorbed layer. The

effective permettivity ε_{eff} is calculated by averaging the permettivity $\varepsilon(z)$ over the depth of the whole multilayered structure, always weighting the local refractive index with a factor that takes into account the exponential decay of the field[77]. This average is therefore calculated with the depth integral:

$$\varepsilon_{eff} = \frac{2}{L}\int_0^{+\infty} \varepsilon(z)\cdot e^{-\frac{2z}{L}} dz \tag{4.5.1}$$

where L is the extention length of the excited SPP. From Maxwell's equations we get an analytical expression for the extention length as a function of the exciting wavelength λ and the surrounding media (see eq. (1.2.3) and appendix A for more details):

$$L = \frac{\lambda}{2\pi}\sqrt{-\frac{\varepsilon_{eff}+\varepsilon_m}{\varepsilon_{eff}^2}} \tag{4.5.2}$$

where ε_m is the dielectric permittivity of the metal side. For a single-layer functionalization of thickness d and dielectric permettivity ε_l we find out from eq. (4.5.1):

$$\varepsilon_{eff} = \varepsilon_0 + (\varepsilon_l - \varepsilon_0)\left(1 - e^{-\frac{2d}{L}}\right) \tag{4.5.3}$$

Since the layer thickness is usually much thinner than the SPP extention length in air $(d \,/\, L \sim 10^{-2})$ it is reasonable to approximate:

$$\Delta\varepsilon = \varepsilon_{eff} - \varepsilon_0 \cong (\varepsilon_l - \varepsilon_0)\frac{2d}{L} \tag{4.5.4}$$

After inserting last expression into (4.5.2) and rearranging terms, we get a 3rd degree polynomial equation to be solved in L unknown:

$$\pi^2\varepsilon_0^2 L^3 + \left[4d\pi^2\varepsilon_0(\varepsilon_l - \varepsilon_0) + 4\pi^2(\varepsilon_l - \varepsilon_0)^2 d^2 + \lambda^2(\varepsilon_0 + \varepsilon_M)\right]L^2 + \frac{d}{2}(\varepsilon_l - \varepsilon_0)\lambda^2 = 0 \tag{4.5.5}$$

Once L has been calculated with the condition $L \geq 0$, after putting the value into eq.(4.5.4), we get the following estimation for the effective refractive index change:

$$\Delta n_{eff} = \frac{\partial n}{\partial \varepsilon} \Delta \varepsilon_{eff} \cong \frac{\varepsilon_l - \varepsilon_0}{\sqrt{\varepsilon_0}} \frac{d}{L} \tag{4.5.6}$$

Thus if film thickness and optical properties, in term of complex dielectric permittivity, are known, it is possible to get an estimation of the corresponding variation Δn_{eff} in the effective refractive index which is experienced by the excited surface plasmon polariton at the considered wavelength.

A self-assembled monolayer (SAM) is an organized layer of amphiphilic molecules[78] in which one end of the molecule, the head group, shows a specific affinity for the substrate. SAMs also usually consist of a tail with a functional group at the terminal end. SAMs are created by the chemisorption of the hydrophilic head groups onto the substrate followed by a slow two-dimensional organization of tail groups into the densely packed structure of a single covering monolayer.

4.5.2 Alkanethiol self-assembling monolayers

In the case of noble metal surfaces, alkanethiols are the most commonly used molecules for SAMs. Alkanethiols *r*-$C_nH_{2n+1}S$ ($C_nH_{2n+2}S$ without the tail group -*r*) are molecules with an alkyl chain $\left(C-C\right)^n$ as the back-bone, a tail group -*r*, and a -SH head group. They are used on noble metal substrates because of the great affinity of sulphur for these metals. The sulphur-gold interaction is semi-covalent and has a strength of approximately 45kcal/mol.

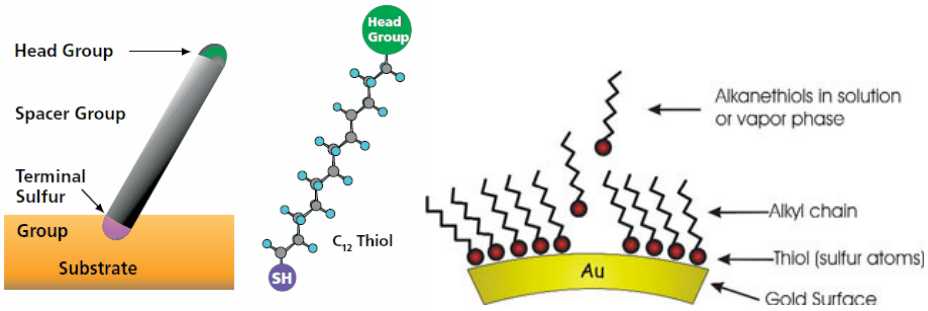

Figure 4-17: scheme of dodecanethiol structure: $CH_3(CH_2)_{11}SH$. Binding onto the gold substrate.

Alkanethiol SAMs produced by adsorption in solution are typically made by immersing a substrate into a diluite solution of alkanethiols in ethanol or methanol for several hours (12-24 hrs). The spontaneous assembly of the molecules is known to form a densely packed and

highly oriented structure on a metallic surface[79]. The monolayer thickness depends obviously on the alkyl chain length. In our cases of interest we functionalized gold surfaces of the fabricated plasmonic platforms with a self-assembled monolayer of dodecanethiol ($C_{12}H_{26}S$, hereafter C12) at room temperature in ethanol.

The substrates were pre-cleaned in a basic peroxide solution (5:1:1 double distilled H_2O, 30% H_2O_2 and 25% NH_4OH) for 10 minutes, rinsed in double distilled water and dried under N_2 flux. The cleaned sample was submerged in 4 mM solution of dodecanethiol in ethanol for about 48 hrs and therefore rinsed thoroughly with ethanol for at least 5 minute, followed by drying under nitrogen stream. C12 has been assumed to form a monolayer 1.46 nm-thick with refractive index $n = 1.458$ [80].

4.5.3 Polyethylene Oxide (PEO) buffer layer

In this contest, a typical SPR biosensor architecture can be simply described as a metal nanostructured substrate (usually gold or silver) onto which is tethered the analyte-specific probe (biorecognizing or sensing element). Due to the expected high sensitivity, the ideal biorecognizing surface should be able to sense the analyte of interest even at very low concentration and reject non-specific interactions with other components of the biological sample, which are often in much larger concentration than the analyte itself. In order to prevent non specific interactions, a non-fouling hydrophilic polymer is generally linked to the sensing surface along with the biorecognizing ligand (generally an antibody or a DNA probe), i.e. between the metal surface and the sensitive element[18].

One possibility is to use poly(ethyleneoxide) (PEO, also called polyethylene glycol – PEG: $C_{2n}H_{4n+2}O_{n+1}$, Figure 4-18), a linear bi-functional amphiphilic polymer, well known for its resistance to nonspecific protein adsorption[81]. Its two ends can be functionalized with different chemical groups according to the envisaged final use.

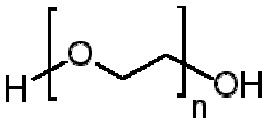

Figure 4-18: poly(ethylene oxide) - PEO structure: $H(\text{-O-}CH_2\text{-}CH_2\text{-})_nOH$.

Within the specific case of SPR application, a thiol group can be attached to one end for gold-polymer binding, while the other end can be used as the biorecognizing element (e.g. a peptide, antibody or nucleic acid probe). Bio-recognizing layers on top of gold surfaces are commonly built up following a multiple step approach, in which a first deposition of a thiolated compound (that forms the first self-assembled monolayer) is later followed by a bioconjugation step through which the biosensing element is covalently linked to the other end of the thiol compound. However, the efficiency of each of these step may vary with some deposition variables (e.g. the degree of thiol oxidation, the pH and concentration of the reagents in covalent coupling) and this can lead to later inter-assay sensing variability. In order to reduce this risk, a standardized deposition strategy is desirable in which the sensitive variables are minimal. This can be achieved by carrying out the deposition through a single step procedure using a thiol derivative with its second-end that already contains both the sensing ligand and the PEO moiety. The PEO compounds synthesized in this work have been tailored under this aim.

Thus a model PEO derivative (mPEO-Cys) was synthesized[82]: at one end a methoxy-group (-CH_3) is contained instead of the biorecognition element, while at the opposite end a cysteine residue is used for gold-polymer binding. Thiol-protected end-functionalized mPEO-Cys (α-methoxy-ω-trt-cys-polyoxyethylene) was synthesized by coupling S-trityl-cysteine to the hydroxyl end of monomethoxy-PEO 5KDa MW ($mPEO_{5000}$-OH). In this reagent (α-methoxy-ω-trt-cys-polyethyleneoxide), the reactive cysteine thiol residue is protected from oxidation by the trityl (Trt) group which can be easily removed by acidic treatment with trifluoroacetic acid (TFA) prior to gold surface incubation. The starting mPEG-OH was dissolved in anhydrous chloroform and activated as N-hydroxy-succinimidylcarbonates by adding two equivalents of di-succinimidylcarbonate (DSC) in the presence of triethylamine (TEA). The reactive intermediate was isolated by diethylether precipitation and later added, under mixing, to a 2 mM trt-Cysteine solution in 0.1 M borate buffer pH 8.5. After 2 hrs at room temperature the final product was extracted with dichloromethane, the organic solution was dried over $MgSO_4$, filtered, and the product was isolated after diethylether precipitation.

Definitive substrates were pre-cleaned in a basic peroxide solution (5:1:1 double distilled H_2O, 30% H_2O_2 and 25% NH_4OH) for 10 minutes, rinsed in double distilled water and dried under N_2 flux.

The trt-protective group was removed just before deposition by dissolving the α-methoxy-ω-trt-cys-poly(ethyleneoxide) powder in the minimum amount of TFA for 20 minutes at room temperature. N_2-saturated double distilled H_2O was then added up to reach 1 mM final thiol concentration. The insoluble trityl residue was removed by centrifugation ($10.000g, 4°C$, 10 min). mPEO-Cys deposition was then carried out in a nitrogen-fluxed incubation chamber by immersing the plasmonic substrate in the surnatant solution varying the incubation time of the substrates in the solution from 1 to 48 hrs. At scheduled times samples were removed and rinsed thoroughly with bi-distilled H_2O in order to remove physisorbed molecules. They were then dried in vacuum (10^{-7} atm) in a desiccator for 90 min. The final surfaces were stored under N_2 atmosphere and far from light.

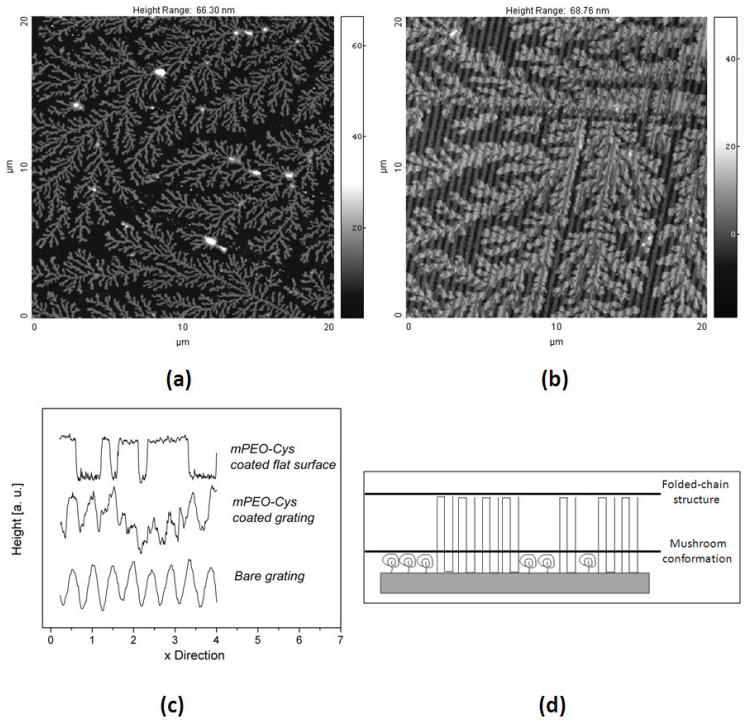

Figure 4-19: AFM images of mPEO-Cys films obtained upon incubation time of 30 hrs onto flat (a) and nanostructured (b) subtrates. Starting from surface profiles after mPEO-Cys deposition (c), the seaweed pattern can be schematized indentifying two different polymer conformations (d): a folded-chain structure and a mushroom-like conformation.

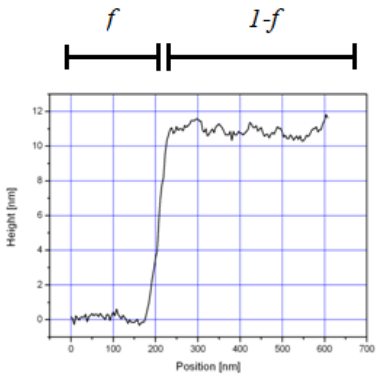

Figure 4-20: AFM profile of a PEO dendrite boundary.

mPEO-Cys film morphology is the starting point for the determination of polymer surface density: from AFM images (Figure 4-19(a) and (b)), both flat and nanostructured surfaces covered by a mPEO-Cys film show a seaweed pattern[83], which is schematized in Figure 4-19(d).

A three-folded chain structure (F) of thickness $d_F = 11\,\text{nm}$ (considering that the whole mPEO-Cys length is approximately $33\,\text{nm}$) and a mushroom conformation (M) of thickness $d_M = 2\,\text{nm}$ are present. We assume that the evolution of polymer molecular conformation is composed by a starting mushroom regime which evolves into a folded regime as molecular surface density increases, thus as incubation time increases.

Starting from these hypotheses, the total number of mPEO-Cys molecules adsorbed onto the surface can be divided into a molecular fraction f which identifies the mushroom-like conformation, and a molecular fraction $1-f$ identifying the folded-chain conformation.

Assuming that the volume-change that may occur passing from a PEO molecule in solution to a PEO molecule adsorbed on the surface is negligible, we can consider the following relationship for an estimation of the area covered by a single molecule in mushroom-like conformation:

$$\frac{4}{3}\pi r_g^3 \approx d_M \pi r_M^2 \tag{4.5.7}$$

where r_g is the tabulated PEO gyration radius in solution, $r_g \sim 2.80\,\text{nm}$, and r_M is the radius of a single PEO molecule in the mushroom-like conformation. From eq. (4.5.7) we get

a value of 3.73 nm for r_M. By assuming an average radius r_F of 0.12 nm for mPEO-Cys chain[84], the area occupied by a single molecule in a three-folded conformation A_F is also calculated. The surface density number N of polymer molecules adsorbed in the mushroom and in the three-folded chain conformations, weighted by the corresponding covering fraction (f and $1-f$ respectively) is given by:

$$N = \frac{f}{A_M} + \frac{1-f}{A_F} \tag{4.5.8}$$

where A_M and A_F are the surface areas occupied respectively by a single molecule in the mushroom and in the three-folded chain regimes, given by $A_M = \pi r_M^2$ and $A_F = 3 \cdot \pi r_F^2$.

The value of f is directly related to the refractive index variation induced by the layer adsorbed onto the metallic grating substrate. The functionalization causes a variation Δn of the effective refractive index and a consequent shift $\Delta\theta$ of the resonance polar angle. By applying an Effective Medium Approximation (EMA) (eq. (4.5.1)), we get the following expression for the refractive index variation as a function of the covering fraction f:

$$\Delta n = \frac{\varepsilon_{PEO} - \varepsilon_0}{\sqrt{\varepsilon_0}} \left[\frac{d_F}{L_F} + f \left(\frac{d_M}{L_M} - \frac{d_F}{L_F} \right) \right] \tag{4.5.9}$$

where ε_0 and ε_{PEO} are respectively the surrounding-medium and mPEO-Cys dielectric permittivies, L_M and L_F are SPP-extention lengths into mPEO-Cys layer in the mushroom-like and in the three-folded zone respectively, and d_M and d_F are the thicknesses of the mPEO-Cys layer in the two different conformations. From the experimental value of the resonance angle shift $\Delta\theta$, it is possibile to get an estimation of the refractive index change Δn:

$$\Delta n = \left(\frac{\partial \theta}{\partial n} \right)^{-1} \Delta\theta \tag{4.5.10}$$

Once the mushroom-like covering fraction f is calculated from previous equation, the resulting surface density units N from eq. (4.5.8) can be converted into mass surface density ($\mathrm{ng/cm^2}$).

SPR analysis of PEO-grafted gratings has been perfomed for increasing time of functionalization process 1-48 hrs (see Figure 4-21). Our experiment gives a mPEO-Cys surface density of $568.1 \pm 66.5\,\mathrm{ng/cm^2}$ after a polymer deposition time of 30 hrs, with $f \sim 0.91$, comparable with the value of 590.7 ± 69.9 obtained after 48 hrs of deposition. Thus we can consider 30 hrs an ideal time for a nanostructured surface saturation, finding the condition needed for the anti-fouling effect of the biosensing layer.

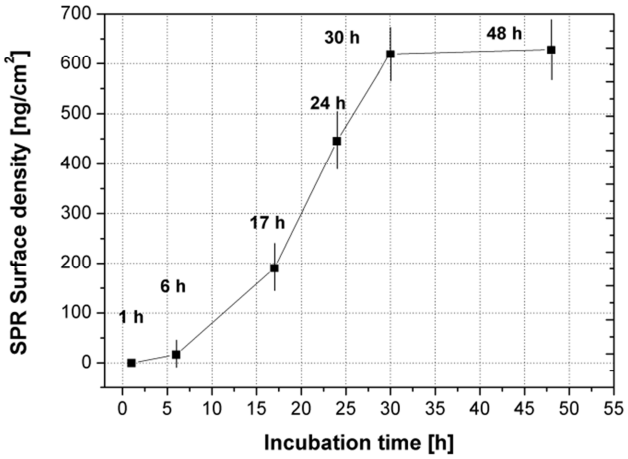

Figure 4-21: estimated PEO density from SPR analysis as a function of the incubation time in solution.

4.6 Nanoporous gold substrates

4.6.1 Nanoporous gold fabrication

Nanoporous gold (NPG) has known a growing interest in last decades due to its potential applications in such areas where the concomitance of a high surface-to-volume ratio and the noble-metal chemistry provides benefits in performance and activity: actuation[85], catalysis[86], supercapacitance[87], sensing[88]. This material exhibits a 3D bicontinous porous structure from few tens to hundreds of nanometers scale, depending on fabrication parameters, which is originated by a spontaneous pattern formation during the selective leaching of the least noble metal from Au alloys[89,90]. This process results in a sponge-like material (see Figure 4-22) with

a large surface-to-volume ratio and a lower free-electron density that exhibits a metallic behavior below the near-infrared range and thus can support excitation and propagation of Surface Plasmon modes.

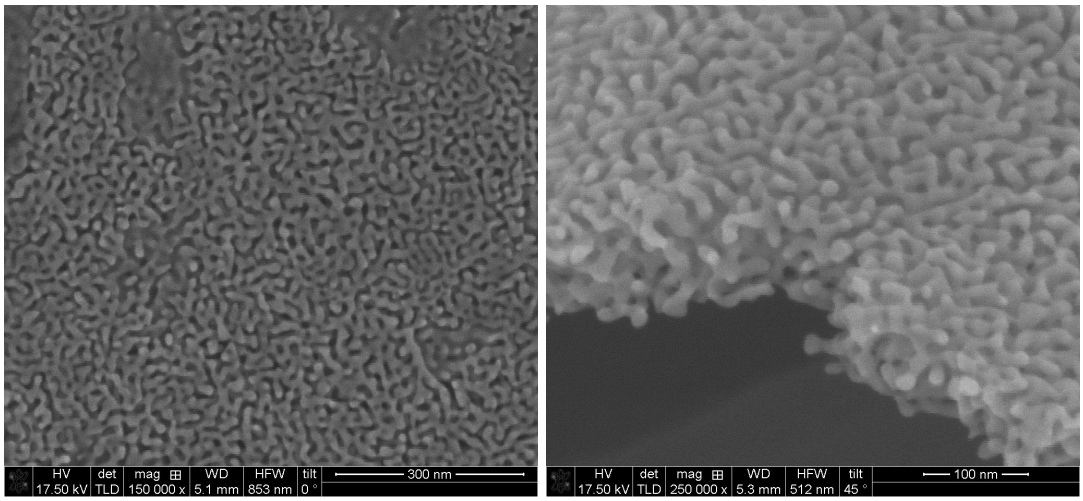

Figure 4-22: top-view and cross-section of a self-standing 100nm thick layer of nanoporous gold, fabricated from chemical dealloying of a $Au_{20}Ag_{80}$ leaf.

Nanoporous gold samples have been fabricated by dealloying of silver-gold alloys in different experimental conditions. Each sample has been observed and characterized with several techniques: scansion electron microscopy (SEM) for pore-size inspection, transmission electron microscopy (TEM) for structure analysis, Electro-Impedance Spectroscopy (EIS) for roughness estimation, Rutherford Back Scattering (RBS) for compositional analysis.

Rectangular glass substrates were accurately degreased in boiling acetone and dried. A 10-nm Cr layer was deposited on glass as an adhesion promoter. Subsequently a Au layer about 100 nm thick was deposited by thermal evaporation over Cr. Finally, a layer about 240nm thick of $Ag_{75}Au_{25}$ alloy was deposited in a DC turbo sputter coater (Emitech K575X, Emitech Ltd., Ashford, Kent, UK), using a silver/gold alloy sputtering target Ag62.3/Au37.7wt%, GoodFellow. The sputtering was performed at room temperature under Ar gas flow at a pressure of $7x10^{-3}$ mbar and a DC sputtering current of 25 mA.

The composition of alloy ($Ag_{75}Au_{25}$) was selected on the basis of literature reports, indicating that: (i) 20 At% Au content is a practical lower limit to warrant a tough porous material[91], whereas at lower Au content the porous structure generated by dealloying tends

to fall apart; (ii) above 26 At% Au the dissolution of Ag atoms is partial and a substantial amount of Ag remains buried, unaffected by dissolution, in the nanoporous structures[92]; (iii) samples with Au content of 28 At% or higher undergo anodic dealloying only upon application of high potentials, inducing oxidation of surface Au atoms and formation of a low-quality, brittle gold layer. Hence, for most purposes the range 22-25 At% Au is optimal, and we selected the upper limit to get the denser final material.

The dealloying process was performed with two alternative procedures: i) *chemical,* exposing the samples to a concentrated HNO_3 solution (65%, Fluka puriss. pro analysis) for 4hrs at $20°C$ (sample C_a) or 1 h at $65°C$ (sample C_b); ii) *electrochemical,* performed anodising the electrodes at the constant potential E = 0.980 V vs a Saturated Calomel Electrode (SCE), in 0.1 M $HClO_4$ (made up from 60% $HClO_4$, Fluka puriss. pro analysi), for 2 hrs at $20°C$ (sample E_a) or 30 min at $65°C$ (sample E_b), using electrochemical cell and tested procedures[93,94]. Each sample was then washed in two steps, first in a fresh 0.1 M $HClO_4$ solution (1 h), then in distilled water (2 hrs), gently dried in a nitrogen stream and stored.

Figure 4-23.a shows examples of the chronoamperometric curves recorded in electrochemical experiments, using a logarithmic time scale to better show phenomena occurring soon after closing the circuit. The current evolution suggests an intuitive division of the dissolution process in three main steps: rapid Ag dissolution from the outermost alloy layers; progress of dissolution towards deeper regions of fresh alloy, until reaching the back gold substrate; slow dissolution of residual Ag from the depleted alloy.

Comparison of experiments at $20°C$ and at $65°C$ shows that the latter conditions give larger current in the first minute, and a more rapid decay at longer times. The integrated dissolution charge, reported as a function of time in Figure 4-23.b, shows for the process performed at higher temperature larger intermediate and final values, indicating more rapid and more exhaustive Ag dissolution: anodization at $65°C$ actually involves a total charge somewhat above the theoretical value of 175-180 mC cm^{-2}, possibly due to some oxidation of the Au surface.

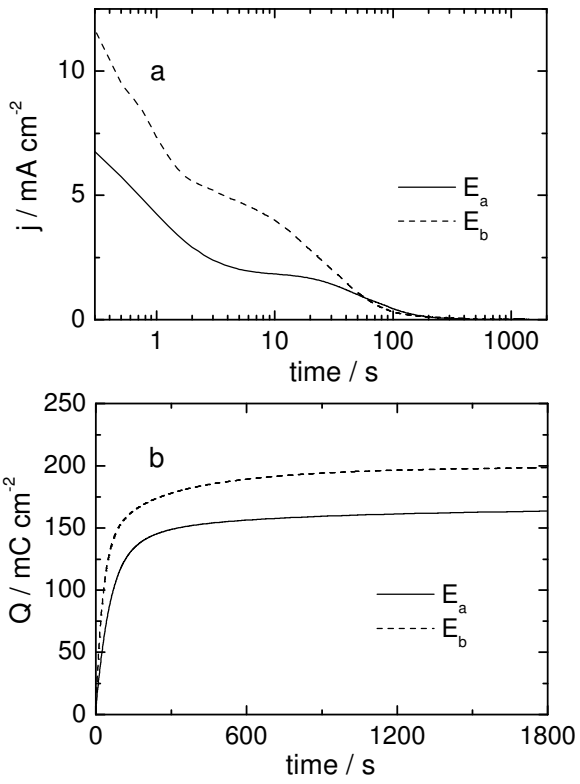

Figure 4-23: Time evolution of (a) current density j and (b) integrated charge Q during anodic treatment of $Ag_{75}Au_{25}$ alloy in 0.1 M $HClO_4$, at E = 0.98 V vs SCE, $T = 20°C$ (sample E_a) and $T = 65°C$ (sample E_b).

For each sample the porosity has been evaluated with Electrochemical Impedance Spectroscopy (EIS) by estimating the roughness factor, namely the ratio $f_r = A_r / A_g$ between the measured surface area A_r and the corresponding geometric area A_g of an ideally flat sample, assumed equal to the ratio between the respective capacities in the low frequency domain $(f_r \cong C_r / C_g)$. EIS measurements were taken using a Solartron 1254 Frequency Response Analyzer and a Solartron 1286 Electrochemical interface, both controlled by a ZPlot-ZView commercial software. The frequency range 20 kHz to 0.1 Hz was explored with 8 points per decade. The double layer capacitance is estimated as the value of the quantity $\left[2\pi f Z''\right]^{-1}$ at $f = 8.4\,\text{Hz}$, in the frequency range typically extending from 50 Hz to 0.2 Hz in which the imaginary impedance $-Z''$ shows an almost ideal dependence on frequency (slope close to -1.0 in the log-log plot), and compared with the capacity of a smooth gold surface. The roughness factor f_r thereby obtained is reported in the 2nd row of table 4.3.

The dealloying process entails a significant volume contraction, estimated at about 20% for bulky samples[95] and thin films[96] of composition similar to ours. Using this value, the effective density of the NPG is estimated as 0.25/0.80 ≅ 0.31 relative to the density of bulk gold, corresponding to a void fraction v_f of about 0.69. This value may be compared with the values in table 4.3, estimated from Rutherford Back-Scattering (RBS) spectrometry: the agreement is good (void fraction ca. 0.68) for the sample E_b, showing little residual Ag, whereas for the other samples the decrease of void fraction is qualitatively consistent with the increase of residual silver.

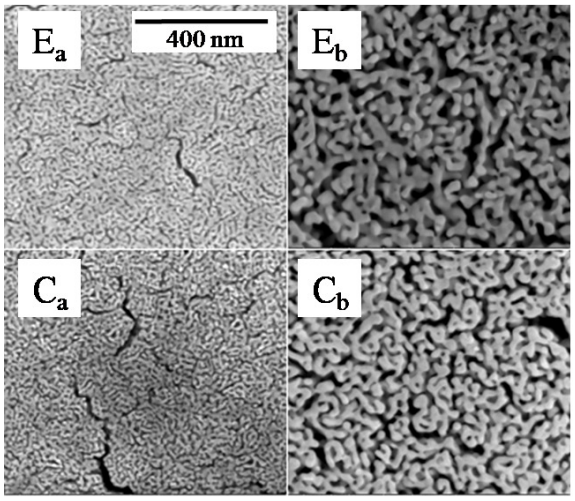

Figure 4-24: SEM micrographs of nanoporous gold surface: chemical sample C_a and C_b, electrochemical samples E_a and E_b .

SEM micrographs were performed, with the semi-in-lens cold cathode field emission scanning electron microscope source of the dual beam FEI Nova 600i instrument. Micrographs were taken at about 5 kV accelerating voltage, using in-lens detector in pure secondary electron signal mode. SEM analysis has been used to get estimations of average pore size and film thickness. In samples fabricated at room temperature the diameter of gold ligaments is around 12 nm for chemical (C_a) and 15 nm for electrochemical dealloying (E_a). Samples fabricated at higher temperature present a greater porosity and ligament size rises up to 36 nm and 41 nm for chemical (C_b) and electrochemical (E_b) samples, respectively (table 4.3). In fact the high temperature is supposed to increase Au atoms mobility during

dealloying process and to promote gold ligaments growth. The factor f_r correlates with the pore size: the bigger the pore the lower the increment of area with respect of that of a non-porous layer.

HRTEM measurements have been done on a Jeol JEM3010 instrument operated at 300kV, LaB_6 cathode, resolution at Scherzer defocus 0.17 nm.

Digital HRTEM images were recorded with a Gatan Multiscan CCD camera MSC794 (1024 x 1024 pixels, pixel size 24 x 24 microns, gain corrected and antiblooming enabled). Speciments for TEM analysis were prepared using mechanical polishing, dimpling and low-angle Ar-ion milling. Inspection of sample E_b is reported in Figure 4-25.

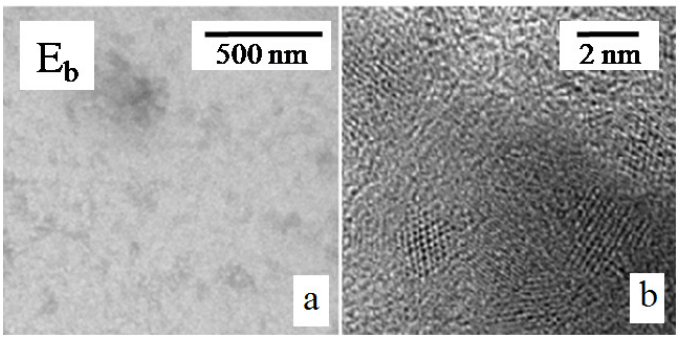

Figure 4-25: TEM analysis of gold ligaments structure of sample E_b.

RBS spectra were recorded with a 2MeV α beam with a scattering angle of $170°$. Analysis were performed by means of an homemade simulation code implementing standard equations for RBS spectra calculation. In order to distinguish between the gold signal coming from the NPG and that coming from the above Au layer, spectra where collected on the bare Au-Cr-Glass substrates. The simulations of these spectra were used as a fixed starting point to simulate the full sample. Analyses of RBS measurements allow estimating the Au and Ag atomic areal density in the porous layer D_{Au} and D_{Ag}. There are two contributions to the total measured dose associated to gold atoms: the gold in the ligaments of the porous structure and the bulk gold beneath in the substrate. Once the contributions are distinguished, from the knowledge of the thickness of the two layers it is possible to evaluate the gold fraction in the nanoporous layer. Assuming a volume density of the bulk fraction of the NPG layer equal to the Au volume density (N_{Au}) and considering the real thickness of

the layer as estimated by SEM t_{SEM} images, it is possible to evaluate the fraction of void v_f in the NPG according to the relation:

$$v_f = 1 - \frac{D_{Au} + D_{Ag}}{N_{Au} \cdot t_{SEM}} \tag{4.6.1}$$

This formula is a good approximation considering the very small difference in atomic density between AuAg alloy and Au.

The result is reported in the 3rd row of table 4.3. As can be noted the data are about 0.64 in good agreement with what expected on the basis of the above considerations and quite independent on the NPG production procedure. Moreover $D_{Ag} / (D_{Au} + D_{Ag})$ quantifies the residual concentration of Ag that is reported in the last row of the table. As can be noted from these data, the high temperature promotes silver dissolution while at room temperature chemical dealloying seems to be more efficient than electrochemical technique in silver etching.

Table 4-3: Properties of samples: roughness factor f_r from capacity evaluation by EIS; average pore size from SEM inspections; void fraction v_f and residual silver fraction from RBS analysis.

	C_a	C_b	E_a	E_b
Pore size (nm)	12	36	15	41
f_r	35.9	11.6	28.5	13.3
$v_f\,(\pm 5\%)$	0.61	0.64	0.61	0.68
Ag %	11	7	16	2

4.6.2 Optical analysis

Spectroscopic ellipsometry between 300 and 2400 nm (10 nm step) was recorded with VASE Spectroscopic Ellipsometer (J.A. Woollam). The goniometer controlled optical bench was set for three different angles of incidence on the sample ($50°$,$60°$,$70°$) and ellipsometric angles ψ and Δ were recorded in the rotating polarizer analysis setup (RAE). Data were analyzed with W-VASE software (J. A. Woollam). A comparative ellipsometric analysis of

bare Au-Cr-Glass substrate and nanoporous gold samples allows extrapolating the complex permittivity $\varepsilon_1 + i\varepsilon_2$ and thus the complex refractive index $n + ik$ of nanoporous gold.

Fully dense gold films exhibit a negative dielectric constant in the optical range for wavelengths above 550 nm (cfr. Figure 1-3). The result is the yellow colour and plasmonic properties in the visible range. In contrast, nanoporous gold films do not become plasmonic at visible wavelengths but rather in the near IR, depending on void content and structure, i.e. pore size. Results of ellipsometric analysis highlight different optical properties for samples prepared with different dealloying processes and temperatures (Figure 4-26).

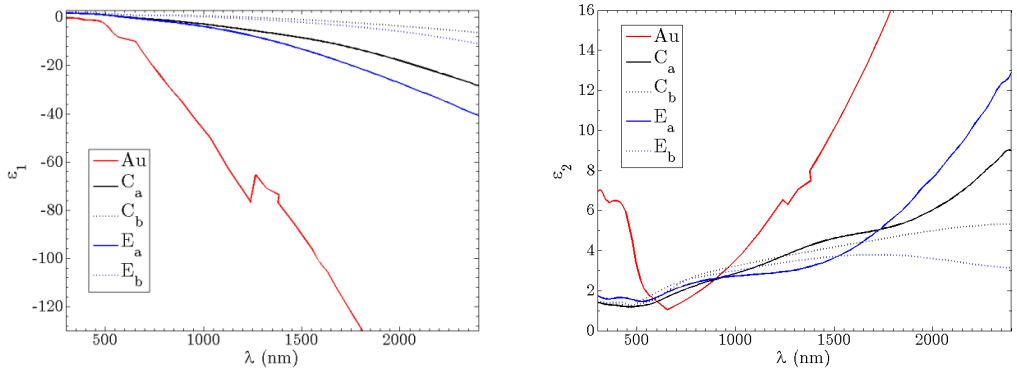

Figure 4-26: Dielectric permittivity real ε_1 and imaginary ε_2 parts. Comparison between evaporated gold (data from Palik[13]) and nanoporous-gold chemical (C_a - C_b) and electrochemical samples (E_a - E_b)

To understand how the plasmonic response changes with the preparation technique, we examine the effective frequency-dependent dielectric function $\varepsilon(\omega)$. In the range from near-UV to near-IR, the permittivity is well described with a Lorentz-Drude model, eq. (1.3.5):

$$\varepsilon(\omega) = \varepsilon_\infty + \varepsilon_{UV}(\omega) + \varepsilon_D(\omega) + \varepsilon_{IR}(\omega)$$

$$\varepsilon(\omega) = \varepsilon_\infty - \frac{A_{UV}}{\omega^2 - \omega_{UV}^2 + i\omega\omega_{\tau,UV}} - \frac{\omega_p^2}{\omega^2 + i\omega\omega_\tau} - \frac{A_{IR}}{\omega^2 - \omega_{IR}^2 + i\omega\omega_{\tau,IR}} \quad (4.6.2)$$

where ε_∞ takes into account the constant contribution to polarization due to d band electrons close to the Fermi surface. ε_{UV} is a Lorentz oscillator that describes the $3d$ energy band-to-Fermi Level interband transition centered at a frequency ω_{UV} in the UV range with a band-width $\omega_{\tau,UV}$. ε_D represents the Drude contribution due to free s-electrons. The

Lorentz contribution ε_{IR} is added in order to describe the behavior of the dielectric response in the near IR range. This extra term enables excellent fits to dielectric constant of nanoporous films and is associated to the excitation of localized surface plasmons[97].

For each sample the permittivity values calculated from ellipsometric analysis have been fitted with the oscillator model (4.6.2) in order to get an estimation of the fitting parameters. Results are collected in Table 4-4. In nanoporous gold the intraband absorption term in the UV range is weaker than in bulk gold: inside gold ligaments each Au atom interacts with much fewer atoms than in bulk metal and this results in a discretization of dipole transitions between sp electron eigenstates and so in the weakening or disappearance of the transition of d electrons to the conduction band[101]. The reorganization of gold atoms also affects the relaxation time τ of free carriers in the Drude term which is shorter than for bulk gold, since it is related to the scattering processes in the material.

The effective density N_{NPG} of free carriers in nanoporous gold can be estimated from plasma frequency ω_p (see eq. (1.3.4)):

$$\omega_p = \sqrt{\frac{e^2 N_{NPG}}{m\varepsilon_0}} \tag{4.6.3}$$

where e and m are electron charge and mass and ε_0 is the void permittivity.

As expected, free-charge density is lower in nanoporous gold samples than in bulk gold obviously because of the lower metal fraction. Despite the void fraction v_f is almost the same for all samples and around the value 2/3 (see table 4.3), the effective free-charge density is up to one order lower than the expected fraction. In sample C_b for example, fabricated by chemical dealloying at $T = 65°C$, the free-electron density is 5% of bulk gold value N_{Au} and it is about half the density for sample C_a, fabricated at room temperature with the same process. The resulting free-charge density is lower than the expected 66% of bulk gold and moreover it results quite different in samples fabricated at different working temperatures.

Table 4-4: fitting parameters using eq. (4.6.2)

	C_a	C_b	E_a	E_b	Bulk
ε_∞	2.04	1.69	2.11	1.63	5.92
$\omega_p(eV)$	3.04	1.96	3.59	2.26	8.36
$\tau\left(fs\right)$	6.05	4.32	4.86	3.46	10.05
$A_{IR}\left(eV^2\right)$	4.63	7.23	1.95	6.73	Abs
$\omega_{IR}(eV)$	1.25	1.32	1.50	1.55	Abs
$\omega_{\tau,IR}(eV)$	1.66	2.09	0.93	2.06	Abs
$A_{UV}\left(eV^2\right)$	24.95	28.18	45.73	28.50	86.65
$\omega_{UV}(eV)$	4.79	5.18	5.01	5.11	4.71
$\omega_{\tau,UV}(eV)$	4.49	3.51	6.52	3.82	3.15

A Maxwell-Garnett (MG) approach can be employed to model the effective dielectric constant of nanoporous layer by assuming the medium as a system of void inclusions into a continuous gold matrix[98]. Typically associated with the MG model[99], the geometric effect is taken into account with a corrective parameter L, the effective depolarization factor, that describes the optical response of the inclusions and depends on their shape and structure (e.g. $L = 1/3$ in the case of spherical inclusions). The resulting relation between the effective free electron density N_{NPG} in nanoporous gold and the free charge density N_{Au} of bulk gold is given by:

$$\frac{N_{NPG}}{N_{Au}} = \mu = 1 - \frac{v_f}{1 - L\left(1 - v_f\right)} \tag{4.6.4}$$

where v_f is the void fraction. By inserting into eq. (4.6.4) the values of void fraction from RBS measurements and the free-charge density ratio μ calculated from the previous optical analysis, it is possible to get an estimation of the depolarization factor L for each sample (see Table 4-5).

Samples fabricated at the same working temperature, although with different dealloying processes, exhibit similar depolarization values. The average factor is $L \sim 0.9$ for samples fabricated at higher temperature and results higher than the average value $L \sim 0.7$ for the same dealloying processes at room temperature. As expected from eq. (4.6.4), the free-charge

density ratio μ decreases for increasing depolarization L, at fixed void fraction v_f. In fact the free-carrier density N_{NPG}, and consequently the plasma frequency ω_p, is lower for samples fabricated at greater temperature, i.e. with greater pore size, although gold density is almost the same.

Clearly gold ligament size and shape affect the effective free-electron density and this results in different optical response and metallic behaviour.

Table 4-5: fitting parameters.

	C_a	C_b	E_a	E_b	Bulk
$N(10^{21} cm^{-3})$	6.73	2.79	9.35	3.70	50.78
μ	0.13	0.05	0.18	0.07	1
v_f	0.61	0.64	0.61	0.68	0
L	0.75	0.89	0.65	0.85	-

4.6.3 Plasmonic properties

Plasmonic properties of nanoporous gold films have been previously shown in recent papers. For example, Yu et al.[100] demonstrated excitation of both propagating and localized surface plasmon resonances in NPG membranes. Dixon et al.[101] reported surface plasmon resonances in ultra-thin films of supported nanoporous Au, and Maaroof et al.[102] showed that the plasmonic behavior of nanoporous gold films can be tuned by controlling the porosity through the initial gold fraction in the selected alloy.

In those papers however, Surface Plasmon Polariton (SPP) excitation was performed in the Kretschmann's configuration where a prism is employed in order to couple illuminating radiation with surface plasmon modes. The cumbersome prism presence and the related alignment problems can be overcome with a periodic patterning of the metallic surface that couple diffracted light and offer a solution more suitable to miniaturization and embodiment.

In this work the surface of nanoporous gold substrates has been patterned in order to support SPPs excitation and propagation on the structure. FIB lithography was performed by means of the ion source of the dual beam system using 30 KeV of accelerating voltage and a beam probe current of 280 pA. Digital grating arrays over an area $640\mu m \times 640\mu m$ large

were fabricated with a single exposure. The geometry of the grating (duty cycle, period and thickness of the walls) was fixed in order to obtain a plasmonic resonance in the near infrared (near-IR) spectral range. When a metallic grating is designed in order to support propagating plasmonic modes, pattern period should be of the same order of the illuminating exciting wavelength: typical grating period is about 500 nm for an evaporated gold surface (cfr chapters 2, 3). Since nanoporous gold exhibits a redshift of metallic behavior, pattern period must be properly dimensioned. Taking into account nanoporous gold plasmonic properties, gratings 50 nm thick with a period of 1000 nm (duty cycle 0.5) have been patterned (see Figure 4-27).

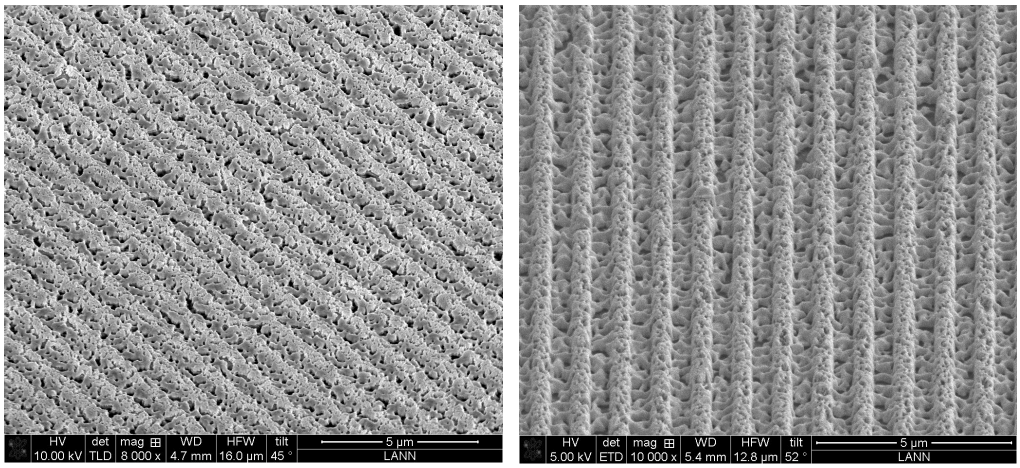

Figure 4-27: SEM micrographs of sample E_b patterned area.

Reflectivity measurements have been collected on the patterned zone in a $\theta / 2\theta$ symmetric configuration, using ellipsometer VASE Xe lamp (75 W), with wavelength λ scanned from 1250 to 1530 nm with step size of 5 nm, at fixed incident angle $\theta = 20°$ (see Figure 4-28).

In the considered wavelength range, resonance broadening and position seem to be mainly affected by sample porosity. Samples fabricated at higher temperature (C_b - E_b) exhibit a broader resonance with respect to samples fabricated at room temperature (C_a - E_a). Comparing samples at room temperature, sample E_a shows a lower width than sample C_a, possibly because of the greater percentage in residual silver (16% versus 11%). The resonance broadening in samples X_b (where X stands for E or C) is mainly related to the increasing in

pore size: a greater porosity results in an increase of dissipation sources and in a consequent decrease of surface plasmons life-time. In samples X_a resonance wavelength λ_{res} is around 1380 nm and it is shorter than in samples X_b where it is near 1410 nm. Dip position seems to mainly depend on fabrication temperature rather than on the dealloying technique. For each sample, reflectivity spectra have been collected with different incident wavelengths λ in the range 1350-1650 nm, step size 50 nm, for angle interrogation from $15°$ to $40°$, step $0.1°$.

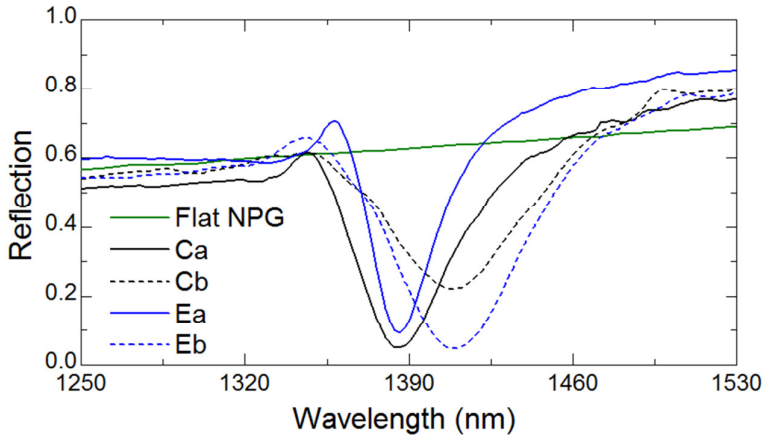

Figure 4-28: Reflectivity for wavelength scan in the range 1250-1530 nm with step size 5 nm for incidence angle $20°$.

Resonance polar angle θ_{res} shifts toward greater values for increasing wavelength and it is possible to reconstruct SPP dispersion curve $\omega - k$ (energy VS wavevector) from eq. (2.2.5). For each incident wavelength λ, SPP momentum k_{SPP} has been calculated from resonance position by applying the equation for grating coupling.

In Figure 4-29 experimental data points of SPP dispersion curve are plotted for each sample. NPG curves differ from the dispersion relation of bulk gold and curves for samples with the same dealloying temperature overlap. This results, as expected, in a dependence on porosity and thus on the fabrication temperature, rather than on the dealloying technique. For a given energy, SPP momentum decreases with increasing porosity, i.e. fabrication temperature.

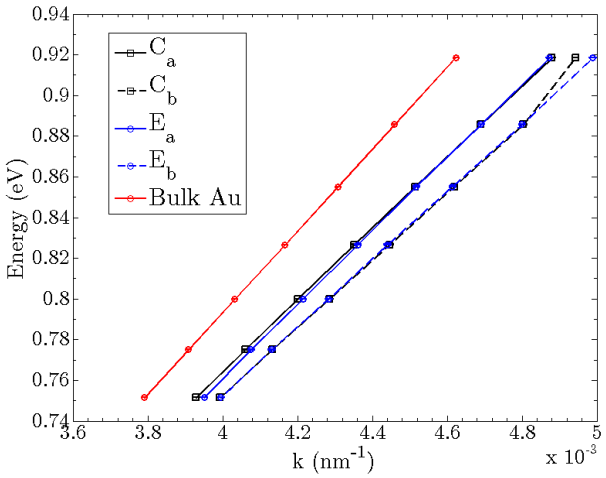

Figure 4-29: Dispersion curve E(eV) - k(nm^{-1}) for Surface Plasmons Polaritons on nanoporous gratings and comparison with a bulk gold grating.

4.7 Conclusions

In this chapter the nanofabrication and characterization techniques for metallic gratings production have been exposed with the support of experimental references to the fabricated samples.

The plasmonic platforms considered in this thesis are sinusoidal metallic gratings fabricated by interferential lithography in the Lloyd's mirror configuration. This technique provides 1D sinusoidal patterns with great coherence over large areas. The developed surface (master) can be directly coated by metals or in turn replicated by soft-lithography process in order to obtain several copies (replica) of the same structure.

Microscopy techniques (SEM-AFM) provide a quality-check of the patterned surface. AFM in particular gives a nanometric inspection of grating geometry and provides precise estimations of period, amplitude and harmonic contributions to the profile function. Spectroscopic ellipsometry is essential for the characterization of the grating stack in terms of thickness and refractive index of each constitutive layer. If the permittivity of each material is known, an estimation of layer thickness can be obtained with angstrom-precision in order

to model and simulate the optical response or to compare the real thicknesses with the nominal values given by fabrication.

Functionalization processes with simple organic thiolate molecules such as dodecanethiol (C12) and polyethileonxide (PEO) have been performed. Dodecanethiol is a simple way to coat the metal surface and analyze the optical response to grating functionalization. PEO can be used as a test-layer as well, but at the same time it represents a fundamental buffer layer for the realization of plasmonic platforms for sensing purposes based on grating-coupling. Thanks to its anti-fouling property, it is used in fact in order to prevent non-specific interactions with non-analyte molecules and reduce signal-to-noise ratio and the overall resolution.

In last sections, the nanofabrication and characterization of nanoporous gold substrates are introduced and described. Experimental results reveal nanoporous gold as a promising material for plasmonic devices, thanks to its enhanced surface-to-volume ratio and the concomitance with a tunable metallic behavior in the near-infrared. In the next chapter the exploitation of patterned substrates of nanoporous gold for the detection of surface functionalization will be performed and discussed.

5 Improving the performance of Grating-Coupled SPR

5.1 Introduction

In our recent works[42,43,103] we experimentally and theoretically described the effects of grating azimuthal rotation on surface plasmon excitation and propagation. More SPPs can be supported with the same illuminating wavelength and a sensitivity up to 1000°/RIU is achievable for the second dip, which is one order of magnitude greater than that in a conventional configurations. Moreover the symmetry breaking with grating rotation makes polarization have a fundamental role on surface plasmon polaritons excitation, and polarization must be tuned after grating rotation in order to perform measurements under the best coupling conditions.

In next section we report the most important results of this research on improving grating-coupled SPR (GCSPR) performance with azimuthal rotation. Sensitivity enhancement has been experimentally tested with self-assembling monolayer functionalization of PEO and C12 and with sodium-chloride solutions flowing through an embodied microfluidic cell.

These results led to the design of an innovative GCSPR setup based on polarization modulation in the conical mounting: with respect to other SPR configurations, the system is left fixed during the analysis and just a polarization scan is performed. This setup offers promising performance in sensitivity and resolution and opens the route to the realization of a new class of more compact, faster and cheaper SPR sensing devices.

Finally, performance of nanoporous gold gratings combined with an azimuthal rotation of the structure are shown and described. Thanks to the concomitance of plasmonic behavior and enhanced surface-to-volume ratio, nanoporous gold seems to guarantee a greater sensitivity than bulk gold gratings and thus reveals an interesting and useful material for the realization of plasmonic platform for sensing devices.

5.2 Sensitivity enhancement by azimuthal rotation

5.2.1 Theory of sensitivity enhancement with azimuthal rotation

The analysis of the wavevector components allows a description of double SPP excitation using the schematic shown in Figure 5-1 and Figure 5-2. The excitation of SPPs on a grating is achieved when the on-plane component of the incident light wavevector and the diffracted SPP wavevector $\boldsymbol{k}_{SPP}$ satisfy the momentum conservation condition (see eq. (1.4.4)):

$$\boldsymbol{k}_{SPP} = \frac{2\pi}{\lambda}\sin\theta_{res}\cdot(1,0) - \frac{2\pi}{\Lambda}(\cos\varphi,\sin\varphi) \tag{5.2.1}$$

where θ_{res} is the resonance polar angle, φ is the azimuth angle, Λ is the grating pitch, λ is the illuminating wavelength. Only the first diffraction order ($n=-1$) is used because in our cases of interest, grating momentum $\boldsymbol{G}$ is always greater than $\boldsymbol{k}_{SPP}$. All quadrants of the circle in Figure 5-1 can be explored for SPP excitation as long as eq. (5.2.1) is satisfied. For symmetry reason, only k_y positive half space is considered.

The largest circle in the k space represents equi-magnitude $\boldsymbol{G}$ vectors at different azimuthal orientation. The two smaller circles represent all possible $\boldsymbol{k}_{SPP}$ vectors with equal magnitude respectively before and after surface functionalization and whose modulus, for shallow gratings, can be approximated by (see eq. (1.2.2)):

$$k_{SPP} = \frac{2\pi}{\lambda}M(\lambda) = \frac{2\pi}{\lambda}\sqrt{\frac{\varepsilon_m\varepsilon_{eff}}{\varepsilon_m+\varepsilon_{eff}}} \tag{5.2.2}$$

where ε_m and ε_{eff} are the dielectric permittivity of the metal and the dielectric side respectively. After functionalization, SPP modulus increases because of the small increase in ε_{eff} due to the surface coating.

The dashed line at the tip of the circle of radius $\boldsymbol{G}$ represents the *x*-component of the photon wave-vector $\boldsymbol{k}_{\parallel}^{(in)}$, the only component that participates in SPP excitation. The line is scaled linearly in $\sin\theta_{in}$ so that the full length of the line at the incident angle θ_{in} of 90° corresponds to the maximum value of $\boldsymbol{k}_{\parallel}^{(in)}$.

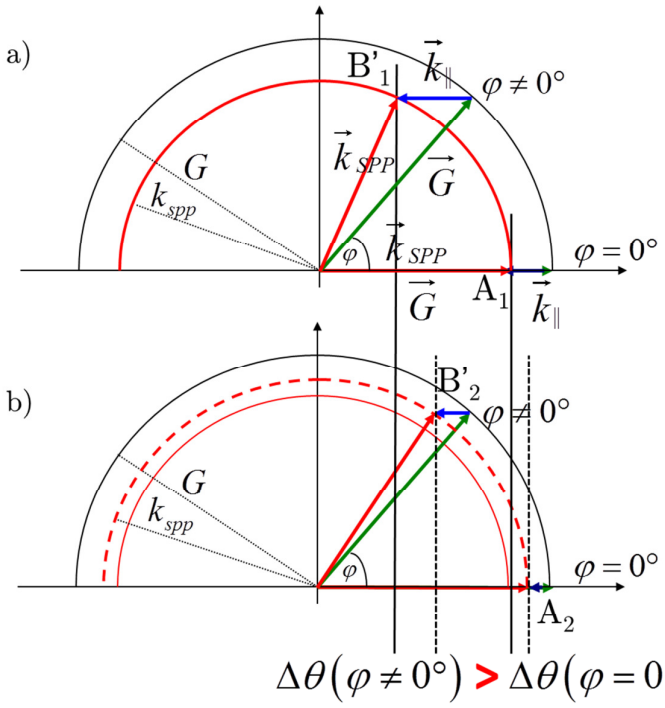

Figure 5-1: Schematic picture of wave-vector combination. The large circle represents equi-magnitude $\boldsymbol{G}$ vectors. The smaller circles represent equi-magnitude vectors $\boldsymbol{k}_{SPP}$ before (a), and after (b) surface functionalization. The blue arrows represent a photon wavevector and the red arrows represent the SPP propagation direction. The letters A and B represent the vector with azimuthal rotation $\varphi = 0°$ and $\varphi \neq 0°$ respectively.

The intersections of the $\boldsymbol{k}_{\parallel}^{(in)}$ dashed horizontal line with the smaller $\boldsymbol{k}_{SPP}$ circle determine the conditions for which eq. (5.2.1) is satisfied and allows the identification of both incident angle θ_{res} for SPP resonance excitation and SPP propagation direction, β. We consider first the case of the uncoated sample - the smallest of the semicircles. For example, point B on the $\boldsymbol{G}$ circle is identified by the azimuthal angle φ and allows the excitation of SPP at two possible conditions: $B_1^{'}$ and $B_1^{''}$, with β^{-} and β^{+} respectively. Within the double SPP range (point B), a small increment in wavelength makes the points $B_1^{'}$ and $B_1^{''}$ merge to form a very broad resonance as shown by wavelength dependence of the reflectivity spectra (Figure 5-5.b). On the contrary, at $\varphi = 0°$ (point A_1) it is clear that the photon wave-vector can intersect the SPP circle only in the first quadrant but not the second, thus exciting only a single SPP for each wavelength (Figure 5-5.a).

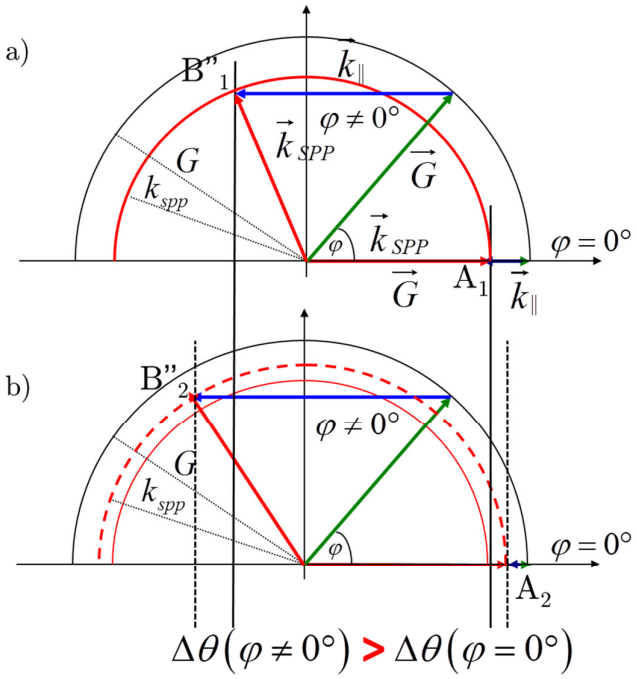

Figure 5-2: Schematic picture of wavevector combination for the 2nd SPP excitation. The large circle represents equi-magnitude $\boldsymbol{G}$ vectors. The smaller circles represent equi-magnitude vectors $\boldsymbol{k}_{SPP}$ before (a), and after (b) surface functionalization. The blue arrows represent a photon wavevector and the red arrows represent the SPP propagation direction. The letters A and B represent the vector with azimuthal rotation $\varphi = 0°$ and $\varphi \neq 0°$ respectively.

The same argument is applicable for light exciting SPP on the functionalized sample. Due to the larger k_{SPP}, different excitation condition is expected. The intersection points changes from $B_1^{'}$ and $B_1^{''}$ to $B_2^{'}$ and $B_2^{''}$ and from A_1 to A_2. The sensitivity of the GCSPP is higher at high azimuthal angles because the condition for double SPP excitation around the circumference of the k_{SPP} circle generates a shifts in k-space between points $B_1^{'}$ and $B_2^{'}$, which is much larger than that between points A_1 and A_2 provided by a single SPP excitation condition for $\varphi = 0°$.

The estimated refractive index sensitivity S of this configuration can be defined as:

$$S = \frac{\partial \theta}{\partial n} = \frac{\partial \theta}{\partial k_{||}} \frac{\partial k_{||}}{\partial k_{SPP}} \frac{\partial k_{SPP}}{\partial n} \tag{5.2.3}$$

In order to calculate S, we assumed the rippling amplitude A of the grating is so shallow ($A / \Lambda \sim 0.05$ in our case) that the dispersion curve of SPP traveling at the metal-dielectric

interface of a grating can be approximated by the case of a flat sample as described by eq. (5.2.2). The analytical expression for the sensitivity in angular interrogation can be found as:

$$S = -\frac{1}{\cos\theta_{res}}\left(\frac{M}{n_0}\right)^3 \frac{\sqrt{\frac{1}{\Lambda^2} + \frac{\sin^2\theta_{res}}{\lambda^2} - \frac{2\cos\varphi\sin\theta}{\Lambda\lambda}}}{\frac{\cos\varphi}{\Lambda} - \frac{\sin\theta}{\lambda}} \tag{5.2.4}$$

where M is defined in eq. (5.2.2), n_0 is the refractive index of the surrounding dielectric medium, the resonance angle θ_{res} is given by eq. (2.3.1) for fixed λ.

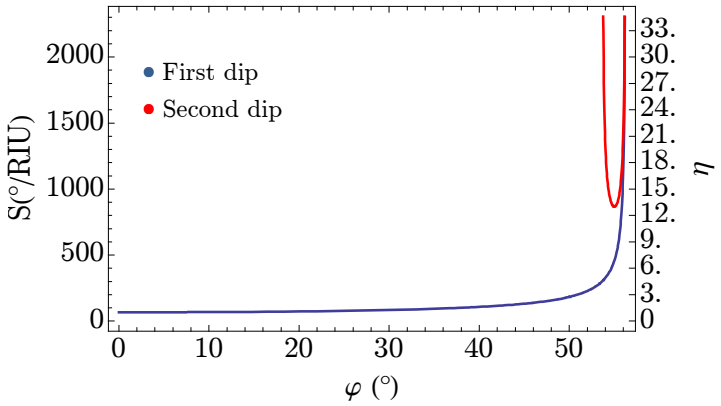

Figure 5-3: Sensitivity S as a function of grating azimuthal angle φ for the two dips in SPR sensor with angular interrogation. The right y-scale refers to sensitivity values normalized to the first dip sensitivity at $\varphi = 0°$: $\eta = S(\varphi) / S(\varphi = 0°)$.

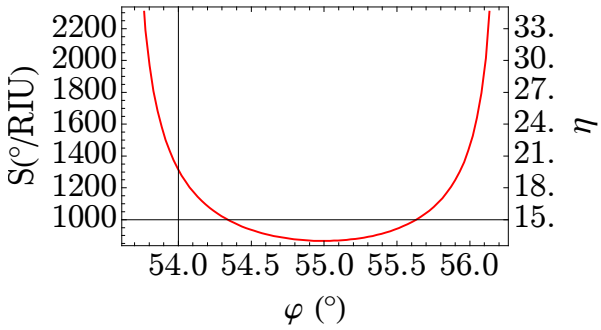

Figure 5-4: Sensitivity S as a function of grating azimuthal angle φ for the second dip in SPR sensor with angular interrogation. The right y-scale refers to sensitivity values normalized to the first dip sensitivity at $\varphi = 0°$ $\eta = S(\varphi) / S(\varphi = 0°)$.

The functional behavior of sensitivity for the first and second SPP dip is shown in Figure 5-3 for a typical wavelength of $\lambda = 606$ nm. Both sensitivities diverge when φ approaches its

critical value φ_{MAX}, i.e. the maximum φ angle that supports SPP resonances. In this configuration, incident photon momentum is tangential to the k_{SPP} circle and its length equals to the k_x - component of the grating momentum so that the denominator in eq. (5.2.4) becomes null. Another condition for second dip sensitivity singularity is when the φ approaches the critical azimuthal angle, φ_c, necessary to excite double SPP resonances, namely when the full length of the incident photon momentum is required to intersect the edge of the k_{SPP} circle. Since the incident angle $\theta_{in} = 90°$, $\cos\theta$ in the denominator of the first term eq. (5.2.4) approaches 0 and S diverges.

Although azimuth φ values close to the critical values provides a great enhancement in S (up to $2400°$/RIU, 35 times higher than $\varphi = 0°$), these configurations should be avoided because of experimental limits. For $\varphi \cong \varphi_c$, θ_{res} becomes large $\theta \geq 70° - 80°$ and broad, becoming impossible to resolve the SPP minimum. In addition, when $\varphi \cong \varphi_{\max}$ the two resonance dips merge into a single broad dip which makes the two minima hardly distinguishable. Thus only limited parts of the azimuthal angular range are suitable for enhancing sensitivity significantly. The best conditions correspond to the middle of the "U-shape" of second dip functional behavior (Figure 5-4) where the sensitivity ranges from $900°$ /RIU to $1100°$/RIU, about 15 times higher than $\varphi = 0°$ whose value is $67°$/RIU. The sensitivity computed for the first SPP dip is smaller all over this range but it still provides values of the order of $500°$/RIU.

5.2.2 Test of sensitivity enhancement with dodecanethiol functionalization

Sensitivity enhancement with azimuthal rotation has been tested with a C12-functionalization of a bimetallic (37Ag/7Au) grating, period 487 nm, amplitude 25 nm. Reflectivity analyses performed before and after C12-coating are collected in Figure 5-5.a-b. The figure shows the experimental evidence of the azimuth rotation, where reflectivity spectra are reported at different wavelengths. As a reference Figure 5-5.a reports the reflectivity spectra using the conventional GCSPR configuration with $\varphi = 0°$. In this configuration, the difference in the reflectivity minima resonance angle $\Delta\theta$ before and after C12 is typically less than $0.05°$. On the contrary after an azimuthal rotation of the grating

to an angle φ of about $60°$, larger angular differences can be observed between the reflectivity dips (Figure 5-5.b). The resonance shift can reach values up to $3.1°$ as for the incident wavelength $\lambda = 618\,\text{nm}$. By increasing wavelength from 606 to 618 nm, the two resonance dips in the reflectivity spectra get closer while resonance shift increases from $1.8°$ to $3.1°$, until the two resonances merge together into a single broad dip at 620 nm.

The experimental determinations of the wavevector $k_{||}^{(in)}$ of the incoming light necessary for the SPP excitation have been successfully fitted with the help of eq.(2.3.1), using as fitting parameters only the effective index of refraction and azimuthal angle (see Figure 5-6.a). After surface functionalization we have determined a total increment in index of refraction equal to $\Delta n = 0.00357 \pm 0.00007$ RIU. This is a value that agrees with the estimation of $\Delta n = 0.0038\,\text{RIU}$ performed for effective refractive index change generated by a full surface coverage of close-packed self assembled C12 molecules, considering their length 1.46 nm with dielectric constant $\varepsilon_{C12} = 2.12$. Also the theoretical sensitivity determination (cfr. Figure 5-3) is in good agreement with the experimental determination obtained as a ratio between $\Delta\theta$, the angular differences before and after C12 coating and the Δn determination. The average experimental sensitivity is of the order of $520°/\text{RIU}$ for the first dip and reaches maximum values of $857°/\text{RIU}$ for the second dip.

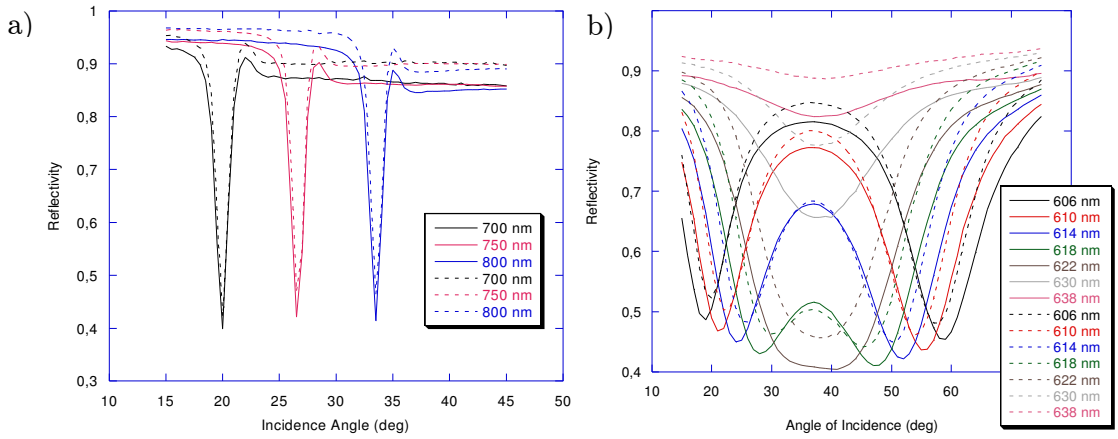

Figure 5-5: Comparison of SPR between uncoated (dashed line) and C12-coated (solid line) Au grating. (a) Grating with $\varphi = 0°$, where different line colors correspond to different incident wavelengths; and (b) $\varphi = 61.6°$ (2 SPPs by single wavelength excitation condition)

The final error of the refractive index determination has been estimated on the basis of chi-square minimization based on *a priori* determination of the SPP angular position. The reflectivity minima of this preliminary data set have been determined with a typical uncertainty of $0.07°$. However the *a posteriori* determination of the SPP angular average deviation with respect to the dispersion curve best fit is much smaller, on the order of $0.015°$, as can be confirmed by a simple graphical inspection (Figure 5-6.a). Taking into account this more realistic value for the final evaluation of the uncertainty, the value of $\sigma_n \sim 10^{-5}$ RIU. However, because our experimental system has an instrumental resolution of $0.001°$, we believe it will be possible to greatly decrease the present angular uncertainty by increasing the statistical signal-to-noise ratio and using appropriate algorithms for data analysis. We expect that experimental uncertainties of Δn on the order of $5 \cdot 10^{-7}$ RIU is achievable. In order to better describe the detection improvement given by azimuthal rotation, we have also measured the typical figure of merit for angular and yield interrogation respectively defined as:

$$FOM_\theta = \frac{S_\theta}{\Delta\theta_{FWHM}} \tag{5.2.5}$$

$$FOM_Y = \frac{Y_{coat} - Y_{uncoat}}{Y_{uncoat}} \tag{5.2.6}$$

where $\Delta\theta_{FWHM}$ is the angular full width at half maximum of the reflectivity minima, whereas Y_{coat} and Y_{uncoat} are the minimum yield of the reflectivity spectra collected before and after C12 functionalization at SPR resonances.

Figure 5-6.b shows the angular and yield FOM at zero and after the azimuthal rotation for all the reflectivity spectra. It clearly appears an enhancement of both the figures of merit after the azimuthal rotation that amounts up to a factor 4 and 10 for the angular and yield FOM respectively. This means that the distance between two dips, before and after the functionalization, scales with a factor greater than the enlargement of the reflectivity dip width. Moreover, it is noted that the reflectivity yield is even more sensitive than the angular position. It clearly appears from the reflectivity spectra of Figure 5-5 that whereas

the minimum yield between coated and uncoated are almost the same for zero azimuth, it changes dramatically after azimuthal rotation. Finally, we note that both the angular and the yield FOM have similar functional behavior: they increase approaching the condition of two dips merging when $\beta_+ = \beta_- = 90°$.

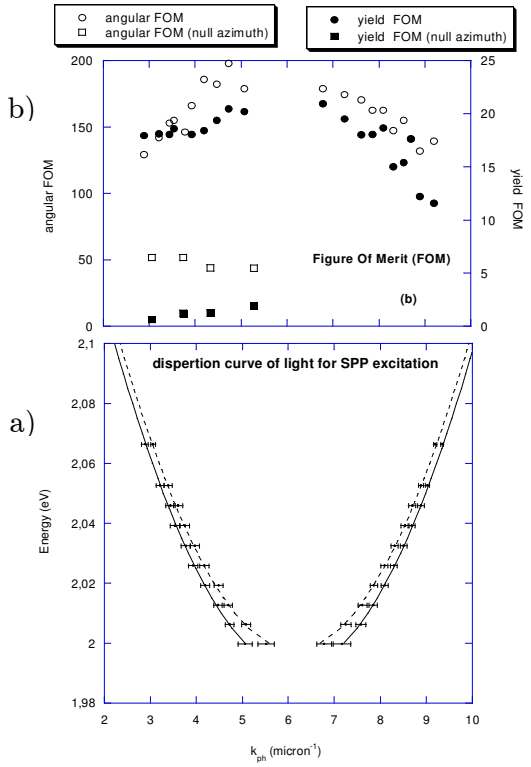

Figure 5-6: a) Energy dispersion curve for the $k_{||}$ necessary for SPP excitation before (solid line) and after (dashed line) C12 SAM functionalization. The experimental data obtained by the reflectivity minima of Figure 5-5 have been fitted using eq. (5.2.1). b) Figure of merit for angular (•,■) and yield (o, □) interrogation of the SPR reflectivity minima.

Although resonance dip becomes broader for increasing azimuth rotation, resonance angle shift increses with a factor which is greater than the broadening rate, thus the angular figure of merit FOM_θ increases and sensing performance improvement is preserved and guaranteed. In fact from eq. (5.2.5) we have:

$$\Phi(\varphi) = \frac{FOM_\theta(\varphi \neq 0°)}{FOM_\theta(\varphi = 0°)} = \frac{S_\theta(\varphi)}{S_\theta(0°)} \frac{\Delta\theta_{FWHM}(0°)}{\Delta\theta_{FWHM}(\varphi)} \tag{5.2.7}$$

where the angular broadening $\Delta\theta$ can be expressed in term of the wavevector uncertainty Δk (eq. (2.3.5)):

$$\Delta\theta_{FWHM}(\varphi) \cong \frac{\lambda}{2\pi}\frac{\Delta k(\varphi)}{\cos\theta_{res}} = \frac{\lambda}{2\pi}\frac{1}{\cos\theta_{res}}\frac{\Delta k(0^\circ)}{\cos\varphi} \tag{5.2.8}$$

Putting last equation into the previous one (eq. (5.2.7)) we get the normalized figure of merit Φ :

$$\Phi(\varphi) = \frac{S_\theta(\varphi)}{S_\theta(0^\circ)}\frac{\cos\theta_{res}(\varphi)}{\cos\theta_{res}(0^\circ)}\cos\varphi \tag{5.2.9}$$

which is an increasing function of the azimuthal angle φ (cfr Figure 5-7).

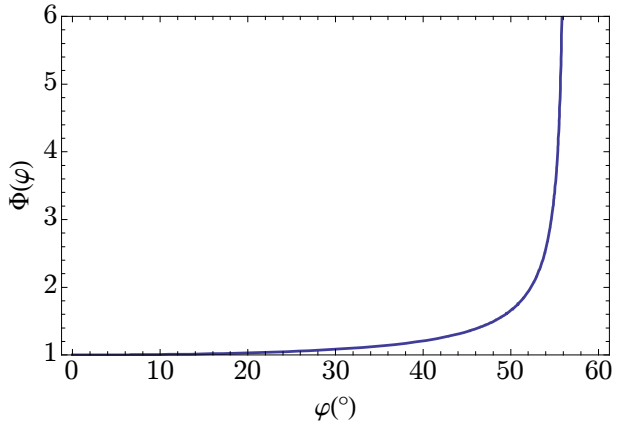

Figure 5-7: normalized figure of merit Φ for the first dip as a function of the azimuth angle φ .

5.2.3 Test of sensitivity enhancement with PEO functionalization

We analysed the plasmonic response of a sinusoidal gold grating with period 505 nm an amplitude 26 nm. All SPR measurements were performed in the $\theta/2\theta$ symmetric configuration with incidence angle scan by a step of 0.1° at the incident wavelength $\lambda = 675$ nm. Reflectivity data were collected before and after PEO-functionalization (after 48 hrs exposition in PEO solution) for increasing value φ of grating rotation in the range from 0° to 46°. In the rotated configuration case, since coupling strength and thus resonance

depth, strictly depends on the incidence polarization angle α, polarization has been properly tuned in order to optimize reflectivity dips. As it was previously demonstrated, resonance-angle shift increases with azimuth (see Figure 5-8): at the limit azimuth $\varphi = 46°$ we get a shift $\Delta\theta(\varphi = 46°) = 8.36°$ which is almost 16 times the response in the non-rotated case $\Delta\theta(\varphi = 0°) = 0.53°$ (Figure 5-8.b). Figure 5-8.a shows reflectivity curves before and after PEO-coating in the classical non-rotated configuration ($\varphi = 0°$) and in the case of $\varphi = 45°$. While in the former the grating is illuminated with *p*-polarization ($\alpha = 0°$), in the latter configuration the polarization has been set to $120°$ in order to optimize resonance depth. By applying an EMA model (eq. (4.5.9)), we can estimate that the excited SPPs experience a change in the effective refractive index $\Delta n = 8.4 \cdot 10^{-3}$ and the resulting sensitivity rises from $S_\theta = 63.1°/\text{RIU}$ for null azimuth, up to $S_\theta = 995.2°/\text{RIU}$ for the rotated case with $\varphi = 46°$.

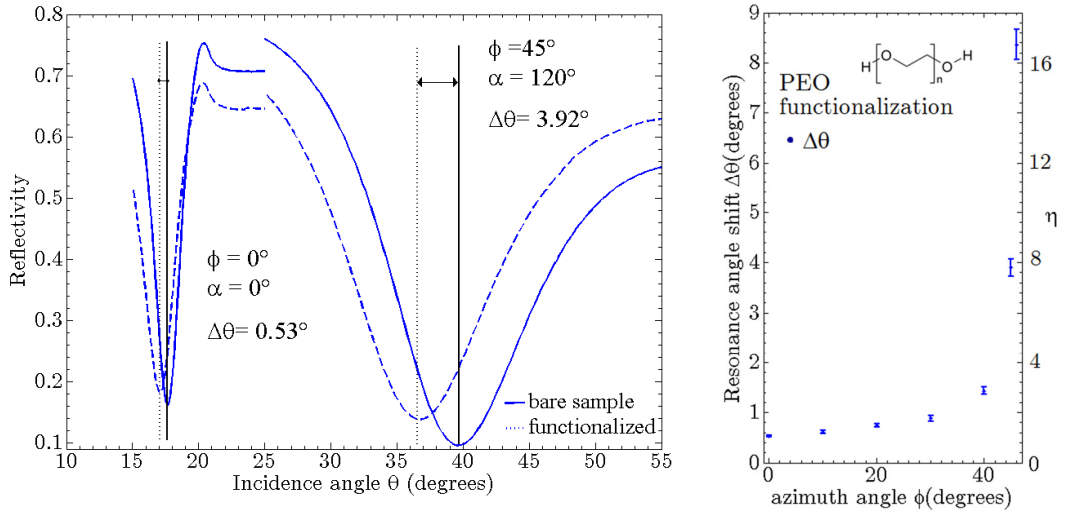

Figure 5-8: reflectivity dips before (solid line) and after (dashed line) grating functionalization with mPEO-Cys SAM for incident wavelength $\lambda = 675\,\text{nm}$, at null azimuth (*p*-polarization, $\alpha = 0°$) and $\varphi = 45°(\alpha = 120°)$. Resonance angle shift and sensitivity enhancement $\eta = S(\varphi) / S(\varphi = 0°)$ as a function of the azimuth angle rotation.

5.2.4 Test of sensitivity enhancement with microfluidic cell

The fabricated metallic gratings exhibits a sensitivity $S_\theta(\varphi = 0°) = 64.9°/\text{RIU}$ for $\lambda = 840\,\text{nm}$ (cfr Figure 4-16). Sensitivity S_θ can be improved just with an azimuthal rotation of the grating plane. For the same fixed concentration of 10g(Nacl) in 200ml(water),

corresponding to a refractive index variation with respect to distilled water $\Delta n = 9.6 \cdot 10^{-3}$, reflectivity spectra have been collected for increasing azimuth angle φ up to $43°$ at the same incident wavelength. As Figure 5-9 shows, resonance angle shift increases monotonically in modulus with increasing azimuth angle from $\Delta\theta(\varphi = 0°) = 0.59°$ to $\Delta\theta(\varphi = 43°) = 5.57°$ corresponding to a sensitivity enhancement $\Delta\theta(43°) \,/\, \Delta\theta(0°) = 9.5$ of almost one order of magnitude: $S_\theta(43°) = 616.8°$ /RIU.

This sensitivity-enhancement technique with azimuthal rotation has been exploited to reveal a lower sodium-chloride concentration than previous ones. A mass of 0.56 g has been dissolved into 200 ml of water and the resulting refractive index change is $\Delta n = 5.4 \cdot 10^{-4}$. With this solution flowing through the microfluidic cell, reflectivity measurements have been performed for increasing grating rotation.

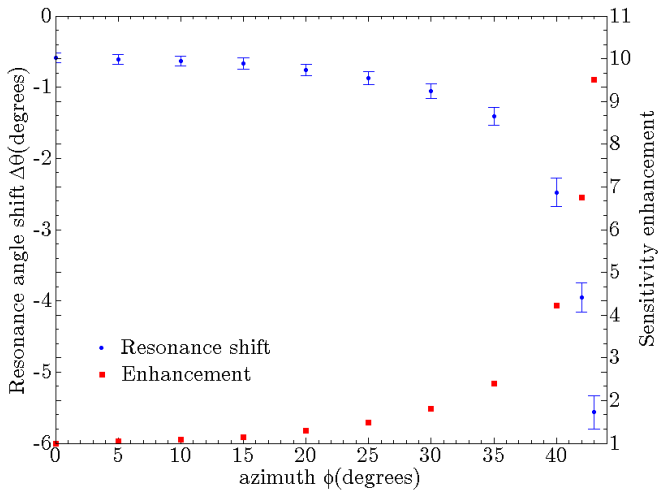

Figure 5-9: Resonance angle shift and sensitivity enhancement as a function of azimuth angle in the range $\varphi = 0° - 43°$. Incident wavelength $\lambda = 840$ nm. NaCl concentration: 10g in 200ml of water ($\Delta n = 9.6 \cdot 10^{-3}$).

The inset picture in Figure 5-10 shows the reflectivity spectra before and after salt dissolution for null azimuth and after grating rotation up to $43°$. While in the classical mounting, i.e. null azimuth, this variation is not detectable within the experimental error, in the conical mounting instead a grating azimuthal rotation increases SPR sensitivity and thus the system allows revealing the resonance angle shift.

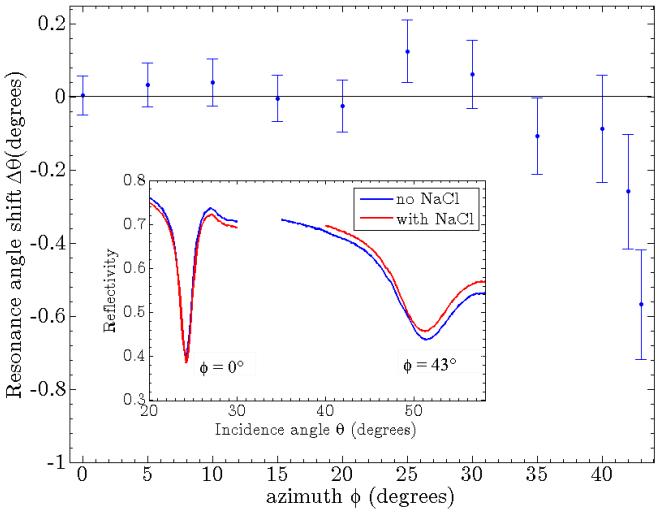

Figure 5-10: Resonance angle shift as a function of azimuth angle in the range $\varphi = 0° - 43°$. Incident wavelength $\lambda = 840\,\text{nm}$. Sodium-chloride concentration: 0.56g/200ml(water), $\Delta n = 5.4 \cdot 10^{-4}$. In the inset graph: reflectivity curve before (blue) and after (red) NaCl dissolution into water, angular scan for azimuth values $0°$ and $43°$.

Resonance dips become broader when azimuthal angle increases, however the resonance angle shift $\Delta\theta$ scales with a factor greater than the enlargement of the dip full width half maximum $\Delta\theta_{FWHM}$. Thus the angular figure of merit FOM_θ increases and the detection improvement by azimuthal rotation is preserved. In this case we have $FOM_\theta(43°) \,/\, FOM_\theta(0°) \cong 4.3$.

5.3 Polarization modulation

In previous sections we experimentally and theoretically described the effects of grating azimuthal rotation on surface plasmon excitation and propagation. More SPPs can be supported with the same illuminating wavelength and a sensitivity enhancement of al least one order of magnitude is achievable than that in the conventional configurations. Moreover the symmetry breaking with grating rotation makes polarization have a fundamental role on surface plasmon polaritons excitation.

As decribed in section 2.4, the minimum of reflectivity $R_{\min}$ exhibits a harmonic dependency on the incidence polarization α with a periodicity of $180°$ (see (2.4.1)):

$$R_{\min} = f_0 - f_1 \cos\left(2\alpha + \alpha_0\right) \tag{5.3.1}$$

where f_0, f_1 and α_0 are fitting parameters that depend on the incidence angles (θ,φ), incident wavelength λ and on the optical properties of the stack (thickness and dielectric permittivity of each layer). By assuming that only the electric field component lying on the grating symmetry plane is effective for SPP excitation, we obtained an analytical expression for the optimal polarization $\alpha_{\min}$ as a function of the azimuth angle φ and the resonance angle θ_{res} (eq. (2.4.6)):

$$\tan\alpha_{\min} = \tan\varphi \cdot \cos\theta_{res} \tag{5.3.2}$$

If the grating surface is functionalized, the effective refractive index n of the dielectric medium changes and resonance conditions are different. As a consequence of the shift in the resonance angle θ_{res} for a fixed azimuth φ, there is a shift $\Delta\alpha_0$ in the phase term α_0:

$$\Delta\alpha_0 = \frac{\partial\alpha_0}{\partial n}\Delta n \tag{5.3.3}$$

This result opens the route to a new GCSPR-configuration with polarization interrogation[104]. In this setup the grating is rotated of an azimuthal angle φ which is kept fixed. The illuminating wavelength λ is fixed and the incoming light impinges on the grating at the resonance angle θ_{res}. A rotating polarizer between source and sample-holder allows changing the polarization incident on the grating. Reflectivity data collected during a polarization scan can be fitted using eq. (5.3.1) and a variation of fitting parameters, e.g. amplitude f_1 or phase α_0, can be used in order to detect grating functionalization or for solution-concentration analysis, once the system has been properly calibrated.

The sinusoidal grating used in this study, with a period of 505 nm and amplitude of 26nm, was fabricated by interferential lithography (IL). The resulting grating has an almost perfect sinusoidal profile with a local roughness of the order of 1.5 nm rms. Subsequently the metallic grating was formed by thermally evaporating a gold (40 nm) metallic layer over 5 nm of chromium adhesion layer. Optical measurements have been performed in $\theta/2\theta$ symmetric reflectivity configuration, using the 75W Xe lamp of VASE Ellipsometer (J.

A. Woollam). A self-assembled monolayer of dodecanethiol was deposited on the gold coated grating surfaces at room temperature.

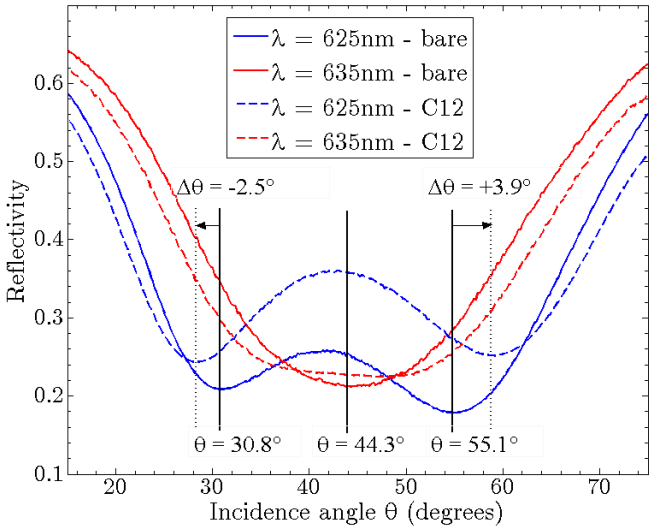

Figure 5-11: Reflectivity for angular scan in the range $15° - 75°$, step size $0.2°$, at incident $\lambda = 625\,\text{nm}$ (blue line), $\lambda = 635\,\text{nm}$ (red line) and azimuth $\varphi = 57.8°$ for incident polarization $\alpha = 140°$, before (solid line) and after (dashed line) functionalization with C12.

First of all, reflectivity spectra have been collected in angular scan to identify the resonance angle position with a weighted centroid algorithm. In order to exploit the shift enhancement, grating was azimuthally rotated and kept fixed at the value $\varphi = 57.8°$ wherein double SPP excitation is supported for the selected wavelength $\lambda = 625\,\text{nm}$ (Figure 5-11). In correspondence of the resonance angles, respectively $\theta_- = 30.8°$ and $\theta_+ = 55.1°$ for the first and second dip, a polarization scan has been collected in the range $\alpha = 0° - 180°$, step $10°$, before and after C12 functionalization (Figure 5-12). The same analysis has been performed at the wavelength $\lambda = 635\,\text{nm}$, for the same azimuth, when the two dips merge into a single broad one centered in $\theta = 44.3°$ (see Figure 5-11).

Reflectivity data as a function of polarization have been fitted with a least square algorithm[105] using eq. (5.3.1): the phase shifts $\Delta\alpha_0$ with their errors σ_α have been estimated. In order to performe a least square study, eq. (5.3.1) has been linearized in a new system of variables $\left(X_i, Y_i\right) = \left(\cos 2\alpha_i, \sin 2\alpha_i\right)$:

$$y_i = f_0 - f_1 \cos\left(2\alpha_i + \alpha_0\right) = f_0 - f_1 \cos 2\alpha_i \cos\alpha_0 + f_1 \sin 2\alpha_i \sin\alpha_0 = \\ = f_0 + A_1 X_i + A_2 Y_i \tag{5.3.4}$$

where $A_1 = -f_1 \cos\alpha_0$ and $A_2 = f_1 \sin\alpha_0$. Thus by applying the least square method to eq. (5.3.4) we get an estimation of parameters (f_0, A_1, A_2) from the experimental N couples $\left(X_i, Y_i\right)$ and we manage to calculate the corresponding values of f_1 and α_0:

$$f_1 = \sqrt{A_1^2 + A_2^2} \\ \cos\alpha_0 = \gamma = -\frac{A_1}{\sqrt{A_1^2 + A_2^2}} \tag{5.3.5}$$

The error on α_0 is given by:

$$\sigma_\alpha = \frac{1}{\sqrt{1-\gamma^2}} \left[\left(\frac{\partial\gamma}{\partial A_1} \right)^2 \sum_{i=1}^{N} \left(\frac{\partial A_1}{\partial y_i} \right)^2 \sigma_i^2 + \left(\frac{\partial\gamma}{\partial A_2} \right)^2 \sum_{i=1}^{N} \left(\frac{\partial A_2}{\partial y_i} \right)^2 \sigma_i^2 \right] \tag{5.3.6}$$

where σ_i is the error on the respective y_i. Results are collected in Table 5-1.

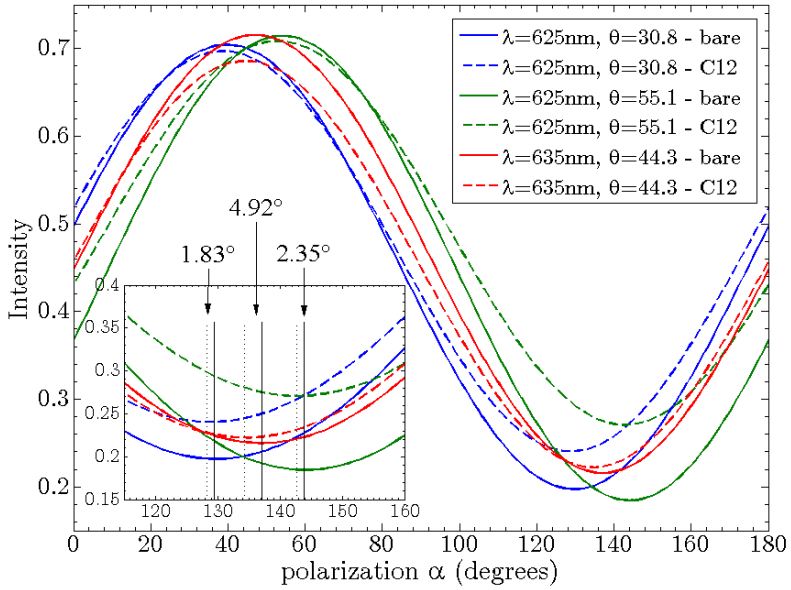

Figure 5-12: Reflectivity minima at incident $\lambda = 625$ nm (blue line: I dip, green line: II dip), $\lambda = 635$ nm (red line), fixed azimuth $\varphi = 57.8°$, resonance polar angles $\theta = 30.8°$ (625 nm, I dip), $55.1°$ (625 nm, II dip), $44.3°$ (635 nm, merged dips): polarization scan before (solid line) and after (dashed line) functionalization with C12. In the inset picture: phase shift $\Delta\alpha_0$.

By modelling the effective refractive index change Δn_{eff} with an effective medium approximation, it is possible to estimate the corresponding phase sensitivity S_α and moreover to calculate the refractive index resolution:

$$\sigma_{n,\alpha} = \frac{\sigma_\alpha}{S_\alpha} \tag{5.3.7}$$

C12 has been assumed to form a monolayer 1.46 nm-thick with refractive index $n = 1.458$ and results in $\Delta n_{eff}\,(625\,\text{nm}) = 50.5 \cdot 10^{-4}$ and $\Delta n_{eff}\,(635\,\text{nm}) = 48.1 \cdot 10^{-4}$. In the case of double SPP excitation ($\lambda = 625\,\text{nm}$), the phase shifts result $\Delta\alpha_0(I) = 1.834 \pm 0.001°$ (first dip) and $\Delta\alpha_0(II) = 2.353 \pm 0.001°$ (second dip), corresponding respectively to sensitivity values $S_\alpha(I) = 363.2°/\text{RIU}$ and $S_\alpha(II) = 465.9°/\text{RIU}$, refractive index resolutions $\sigma_{n,\alpha}(I) = 2.7 \cdot 10^{-6}\,\text{RIU}$ and $\sigma_{n,\alpha}(II) = 2.1 \cdot 10^{-6}\,\text{RIU}$. For $\lambda = 635\,\text{nm}$, we get $\Delta\alpha_0 = 4.919 \pm 0.002°$, $S_\alpha = 1022.7°/\text{RIU}$ and $\sigma_{n,\alpha} = 2.0 \cdot 10^{-6}\,\text{RIU}$.

Table 5-1: . Comparison between angular and polarization interrogation GCSPR with the considered setup. Estimated sensitivity and resolution.

dips	I	II	merged
$\lambda(nm)$	625	625	635
Δn	$5.1 \cdot 10^{-3}$	$5.1 \cdot 10^{-3}$	$4.8 \cdot 10^{-3}$
$\Delta\theta(°)$	2.51 ± 0.14	3.92 ± 0.15	--
$\Delta\alpha_0(°)$	1.884 ± 0.001	2.353 ± 0.001	4.919 ± 0.002
$S_\theta(°\ /\ RIU)$	492.2	768.6	--
$S_\alpha(°\ /\ RIU)$	363.2	465.9	1022.7
$\sigma_{n,\theta}(RIU)$	$2.8 \cdot 10^{-4}$	$1.9 \cdot 10^{-4}$	--
$\sigma_{n,\alpha}(RIU)$	$2.7 \cdot 10^{-6}$	$2.1 \cdot 10^{-6}$	$2.0 \cdot 10^{-6}$

Thus refractive index changes of order 10^{-6} RIU are easily detectable and the resolution can be further improved to $10^{-7} - 10^{-8}$ by reducing output noise σ_I (i.e. the errors σ_i on y_i) or by increasing the number N of the collected points during the polarization scan, since we can assume that:

$$\sigma_\alpha \propto \frac{\sigma_I}{\sqrt{N}} \tag{5.3.8}$$

Furthermore this technique provides a resolution at least two order greater than polar angle modulation with the same setup, which results around $\sigma_{n,\theta} \sim 10^{-4}$, since angle accuracy decreases when azimuth increases because of dip broadening. Moreover, while angle-modulation SPR becomes difficult near the merging dip condition, since dip position is hardly detectable, in the polarization-modulation case the analysis is still valid and it assures a greater sensitivity.

Thus we experimentally demonstrated a new GCSPR technique based on polarization interrogation in a fixed conical mounting setup. Since the output trend is a well-known function of polarization, this method assures a great accuracy on fitting parameters and their dependence on grating surface conditions provides a solution to detect and quantify surface functionalization or solution concentration. This method assures a competitive resolution down to 10^{-8} and limits the mechanical degrees of freedom just to the polarization control. The option of using an electronic modulator instead of a rotating polarizer, further assures the possibility to realize very compact, fast and low-cost high-resolution plasmonic sensors.

5.4 Nanoporous gold substrate

The nanoporous gold substrate of sample C_b, fabricated by chemical dealloying of a $Ag_{75}Au_{25}$ alloy (see section 4.6.1), has been patterned by FIB lithography. Focused Ion Beam (FIB) lithography was performed by means of the ion source of the dual beam FEI system using 30 kV of accelerating voltage and a beam probe current of 280 pA. Taking into account the lower plasma frequency of NPG and the resulting shift of metallic behavior in the IR range, a grating about 50 nm thick with a period of 1000 nm (duty cycle 0.5) has been patterned (Figure 5-13.a) over an area $640\mu m \times 640\mu m$. A cross section of the grating pattern shows that the typical amplitude of the grating is confined within the first 70 nm of the surface NPG (Figure 5-13.b). For comparison with the gold NPG case, a grating with

period of about 400 nm was patterned on a typical gold bulk film of 80 nm thickness evaporated over a silicon substrate.

A self-assembled monolayer (SAM) of benzenethiol (Thiophenol, C_6H_5SH) was deposited on the gold coated grating surfaces at room temperature. The substrates were submerged in a 3-mM solution of benzenethiol in methanol for about 48 hrs, then rinsed thoroughly with ethanol for at least 5 minutes and dried in a nitrogen stream[106]. Measurements on gold gratings were performed in air environment in a $\theta/2\theta$ symmetric reflectivity configuration, with θ scanned with step size of $0.2°$, using ellipsometer 75 W Xe lamp, monochromatized at $\lambda = 1400$ nm for NPG grating and at $\lambda = 600$ nm for the evaporated gold (EVG) grating.

Reflectivity data for increasing azimuth angles have been collected before and after benzenethiol-functionalization from the patterned NPG surface[107]. We previously demonstrated how the azimuthal rotation of the grating can enhance sensing capability up to at least one order of magnitude. Furthermore, after grating azimuthal rotation, *p*-polarization is no longer the most effective for SPP excitation and incident polarization must be tuned to the optimal value in order to enforce coupling strength and optimize resonance depth.

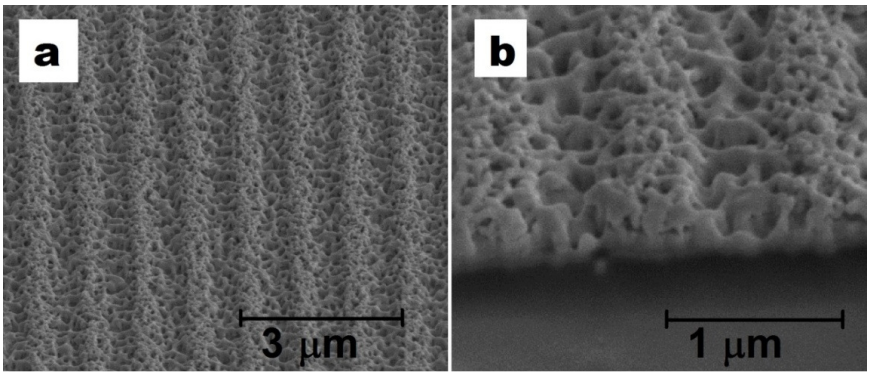

Figure 5-13: SEM micrographs of the FIB pattern on the nanoporous gold surface (a) and cross-section (b).

Data points in Figure 5-14 show the increasing of resonance angle shift with azimuth rotation for the optimized polarization α of light ($\alpha = 0°$ for *p*-polarization, i.e. the electric field lies on the scattering plane). At the limit azimuth value of $45°$ and polarization

$\alpha = 140°$, a shift $\Delta\theta_{NPG}(\varphi = 45°) = 4.05°$ is measured, which is almost 65 times grater than the shift for null azimuth and *p*-polarization $\Delta\theta_{NPG}(\varphi = 45°) = 0.06°$ ($\alpha = 0°$).

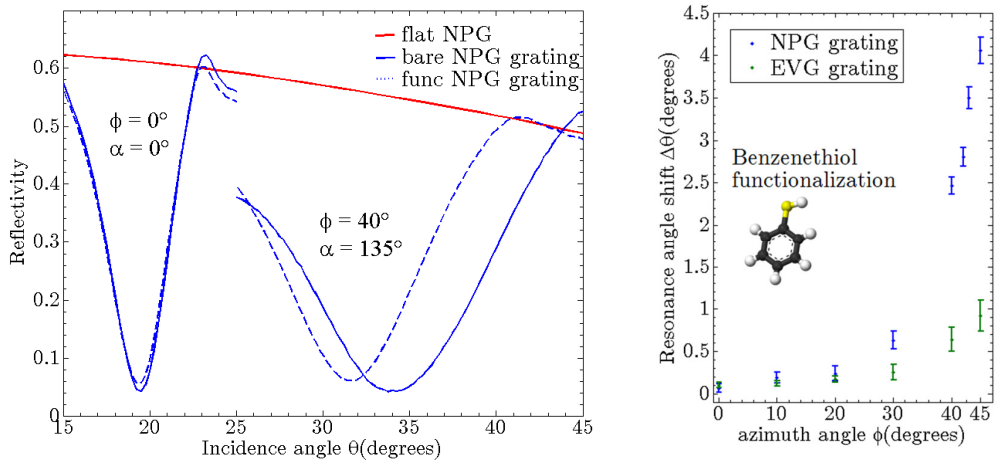

Figure 5-14: a) Reflectivity for NPG grating before (solid line) and after (dashed line) functionalization at null azimuth and *p*-polarization, and at azimuth $\varphi = 40°$ $(\alpha = 140°)$. Red solid line: reflectivity data for non-patterned NPG surface. b) Resonance angle shift $\Delta\theta$ as a function of azimuthal rotation after functionalization: experimental data of functionalized NPG grating (period $\Lambda = 1000$ nm, incident wavelength $\lambda = 1400$ nm – blue points) are compared with shifts for an evaporated-gold (EVG) grating ($\Lambda = 400$ nm, $\lambda = 600$ nm – green points).

Resonance dips become broader for increasing azimuth value, however the resonance angle shift $\Delta\theta$ scales with a factor greater than the enlargement of the dip full width half maximum $\Delta\theta_{FWHM}$. Thus the angular figure of merit FOM_θ increases and the detection improvement by azimuthal rotation is preserved. In our case $FOM_\theta(\varphi = 45°) = 0.277$ that is 18.5 times greater than $FOM_\theta(\varphi = 0°) = 0.015$.

In order to compare the sensitivity of the plasmonic gratings, reflectivity data have been also compared with the optical response of an evaporated gold (EVG) grating after the same functionalization process. EVG surface has been patterned with a period $\Lambda = 400$ nm in order to excite SPPs in the visible range, where the angular response for EVG is greater since the sensitivity to a thin coating layer decreases with wavelength. For incident $\lambda = 600$ nm and azimuth $\varphi = 45°$ ($\alpha = 135°$) we measure a shift $\Delta\theta_{EVG}(\varphi = 45°) = 0.82°$.

The choice of evaluating the EVG and NPG gratings at different wavelengths has been motivated to compare them at the respective maximum of sensibility. The greater dip shift in the case of patterned NPG is explained by the enhanced binding surface per unit area of the nanopores. Analyte molecules in fact, not merely bind in the form of a thin coating layer on the outer surface, but, in the case of NPG, penetrate into the pores and bind to the inner surface, inducing a greater change of the effective index of the plasmonic support.

5.5 Conclusions

Azimuthal rotation of the plasmonic support has been demonstrated to considerably increase grating sensitivity to refractive index change. A sensitivity up to one order greater than that in the classical mounting with null azimuth can be achieved just with a rotation of the sensing platform. Experimental results with C12/PEO functionalization and measurements in cell support this improvement and confirm the benefits of azimuthal control for sensing purposes.

The setup of a grating-based sensing configuration with polarization modulation has been tested with C12 functionalization and results confirm the promising possibilities that are opened up by this invention.

The concurrent exploitation of azimuthal rotation and enhanced surface in nanoporous gold gratings, has been demonstrated to provide a further possibility of improving sensitivity performance in plasmonics application for sensing devices.

Conclusions

Plasmonic gratings have been demonstrated to assure a high-sensitive optical response to surface functionalization and to represent a promising and irreplaceable component for the realization of label-free devices for sensing purposes with considerable performance in refractive index sensitivity and resolution. The problem of designing and realizing metallic gratings for sensing applications has been studied and analysed through each step of the process-chain: simulation - nanofabrication - characterization.

A numerical algorithm, based on Chandezon's method, has been implemented in order to provide such a complete analysis of the diffraction problem of a multi-layered patterned surface that overcomes limitations of simpler and less rigorous analyses like the vectorial model. However both methods reveal benefits and usefulness in the realization of a grating-coupled surface plasmon resonance device. The numerical code provides a precise estimation of grating reflectivity and is an essential tool to design, for given geometry and material choice, the optimal profile that optimizes the coupling strength of incident light with surface plasmon polaritons. Thus simulation is useful for providing to nanofabrication the proper windows of process for the production of optimized supports. Moreover simulation supplies a near-field analysis of the plasmonic fields on gratign surface, which experimental techniques could hardly give.

As regards the nanofabrication of these components, interferential lithography is the preferred method for fabricating periodic pattern with a spatial coherence over large areas, while grating-replica process by soft-lithography assures the possibility of a fast and cheap throughput of perfectly replicated gratings. With respect to prism-coupling, grating nanofabrication technology assures the possibility to miniaturize and integrate the sensing components without a considerable increase of the total expenditure. Moreover, our results further highlight grating-coupling advantages rather than prism-coupling thanks to the sensitivity enhancement with azimuthal rotation. An enhancement at least one order greater than the conventional mounting has been theoretically and experimentally demonstrated. If the azimuthal rotation of the grating support increases refractive index sensitivity, on the

other hand incident polarization must be tuned in order to best couple incident light and optimize the optical response. The vectorial model provides an analytical expression of the optimal polarization that can be easily estimated from the incidence angles without the use of complex numerical algorithms.

The dependence of polarization angle on the resonance conditions, suggests the exploitation of a new SPR configuration based on polarization modulation in the conical mounting. The phase term of a polarization scan, which is proportional to the optimal polarization, has been experimentally demonstrated to be a sensitive parameter for surface functionalization analysis. Moreover, this sensing configuration hugely simplifies the mechanical complexity of the device by limiting the degrees of freedom just to the rotating polarizer. The option of using an electronic modulator instead of a rotating polarizer, might further assure the possibility of realizing very compact, fast and low-cost high-resolution plasmonic sensors based on polarization modulation. This innovative sensing configuration, that exploits both azimuthal-rotation and polarization-scan for high-resolution sensing, led to the registration of a US and European patent.

Further research is needed in order to completely understand phase-term shift dependence on refractive index changes. The analysis of the phase shift for increasing sodium-chloride concentration of water solution flowing through the microfluidic system could provide useful information on its behaviour and moreover give an estimation of the linearity range.

The first prototype of a grating-coupled SPR device that exploits this innovative configuration has been recently assembled and is under testing right now.

The research on nanoporous-gold led to the design of promising plasmonic structures for sensing which combines the greatly enhanced surface-to-volume ratio with the plasmonic features of this material in the near-infrared. The tunability of the plasma frequency and the greater sensitivity to functionalization, reveals nanoporous gold as an interesting and powerful material for the realization of nanopatterned platforms for sensing purposes.

Acknowledgements

This work would not have been possible without the collaboration and the contribution of several groups and expertises. A particular thank to Gabriele Zacco for his essential activity of interferential lithography and to Denis Garoli for the assistance in FIB lithography of nanoporous gold grating and SEM analyses, but moreover for the daily interesting and challenging scientific discussions in the laboratory. I wish to thank Sandro Cattarin for his precious and fruitful contribution in the realization of the nanoporous gold substrates and Davide De Salvador for RBS analysis of the samples. Thanks also to Marco Natali for his very useful training in soft-lithography processes for microfluidics. An acknowledgement to Agnese Sonato for his contribution in grafting of gold surfaces with polyethylenoxide and to Marta Carli for AFM assistance.

I would like to take this opportunity to thank my supervisor Filippo Romanato, for giving me the change to grow up in the research group of LaNN and to mould my research attitude inside a young, blooming, challenging background. Among his most precious advice, besides hard-working and interdisciplinary team-working as essential ingredients of a successful research, the exhortation to keep always in mind that Physics has never to lose the contact with reality, as he is used to say by paraphrasing G. Galilei's famous quote:

"Io stimo piu' il trovar un vero,
benche' di cosa leggera,
che 'l disputar lungamente
delle massime questioni
senza conseguir verita' nissuna (G. Galilei)"

Moreover I would like to thank the other colleagues of LaNN laboratory who have daily accompanied my research activity: Tommaso Ongarello, Giuseppe Parisi, Pierfrancesco Zilio, Michele Massari, Enrico Gazzola, Simone Brusa and Gioia della Giustina. Because friendship makes research much better.

Appendix A

Surface Plasmon Polaritons as propagating localized solutions of Maxwell's equations

We consider a trasverse-magnetic (TM) plane-wave which propagates in the positive x-direction along the interface between two media A and B. Since we are looking for localized electromagnetic waves, the magnetic field $\boldsymbol{H}$ should exhibit the following form:

$$\begin{aligned} z > 0 \qquad & \boldsymbol{H}(x,z,t) = \left(0, H_A, 0\right) e^{ik_{A,x}x - k_{A,z}z} e^{-iw_A t} \\ z < 0 \qquad & \boldsymbol{H}(x,z,t) = \left(0, H_B, 0\right) e^{ik_{B,x}x + k_{B,z}z} e^{-iw_B t} \end{aligned} \tag{A.1}$$

where $k_{A,z}$ and $k_{B,z}$ must be positive in order to describe an electromagnetic wave localized at the interface $z = 0$. From the continuity condition of magnetic field components at $z = 0, \forall(x,t)$, it follows that $\omega_A = \omega_B = \omega$, $H_A = H_B = H$ and $k_{A,x} = k_{B,x} = k_x$:

$$\begin{aligned} z > 0 \qquad & \boldsymbol{H}(x,z,t) = \left(0, H, 0\right) e^{ik_x x - k_{A,z}z} e^{-iwt} \\ z < 0 \qquad & \boldsymbol{H}(x,z,t) = \left(0, H, 0\right) e^{ik_x x + k_{B,z}z} e^{-iwt} \end{aligned} \tag{A.2}$$

Calculating the curl of $\boldsymbol{H}$ and applying Maxwell equations we get the following expressions for the electric field components:

$$\begin{aligned} z > 0 \qquad & \boldsymbol{E}(x,z,t) = \left(\frac{Hk_{Az}}{\omega\varepsilon_A}, 0, \frac{Hik_x}{\omega\varepsilon_A}\right) e^{ik_x x - k_{A,z}z} e^{-iwt} \\ z < 0 \qquad & \boldsymbol{E}(x,z,t) = \left(-\frac{Hk_{Bz}}{\omega\varepsilon_B}, 0, \frac{Hik_x}{\omega\varepsilon_B}\right) e^{ik_x x + k_{B,z}z} e^{-iwt} \end{aligned} \tag{A.3}$$

The boundary conditions on the electric field components imposes that $E_{A,x} = E_{B,x}$ at $z = 0$, thus we get:

$$\frac{k_{A,z}}{\varepsilon_A} + \frac{k_{B,z}}{\varepsilon_B} = 0 \tag{A.4}$$

Since $k_{A,z}$ and $k_{B,z}$ must be real and positive, it follows that:

$$\varepsilon_A \cdot \varepsilon_B < 0 \tag{A.5}$$

It is worth noting that if the former medium A is a dielectric, the latter medium B has to exhibit $\varepsilon_B < 0$ for this surface waves to exist. Using eq. A.4 and the definition of $k_{i,z}$ obtained substituting the solution into the wave equation:

$$k_{i,z} = \sqrt{k_x^2 - \varepsilon_i \left(\frac{\omega}{c}\right)^2} \tag{A.6}$$

we obtain an explicit expression for the wavevector k_x of surface plasmon polaritons as a function of frequency ω:

$$k_x = k_{SPP} = \frac{\omega}{c}\sqrt{\frac{\varepsilon_A \varepsilon_B}{\varepsilon_A + \varepsilon_B}} \tag{A.7}$$

If we consider instead a trasverse-electric (TE) plane-wave propagating along the same structure and we look for a solution of Maxwell equations which is localized at the interface between the two media, as in the previous case fields have to exhibit the following form:

$$\begin{aligned} z > 0 \qquad & \boldsymbol{E}(x,z,t) = \left(0,E,0\right) e^{ik_x x - k_{A,z} z} e^{-iwt} \\ z < 0 \qquad & \boldsymbol{E}(x,z,t) = \left(0,E,0\right) e^{ik_x x + k_{B,z} z} e^{-iwt} \end{aligned} \tag{A.8}$$

$$\begin{aligned} z > 0 \qquad & \boldsymbol{H}(x,z,t) = \left(\frac{-icEk_{Az}}{\omega}, 0, \frac{cEk_x}{\omega}\right) e^{ik_x x - k_{A,z} z} e^{-iwt} \\ z < 0 \qquad & \boldsymbol{H}(x,z,t) = \left(\frac{icEk_{Bz}}{\omega}, 0, \frac{cEk_x}{\omega}\right) e^{ik_x x + k_{B,z} z} e^{-iwt} \end{aligned} \tag{A.9}$$

The continuity of the tangential components at $z = 0$ gives the following condition:

$$\left(k_{A,z} + k_{B,z}\right) E = 0 \tag{A.10}$$

However since the real parts of $k_{A,z}$ and $k_{B,z}$ must be positive in order to describe a localized wave, the only possible solution is $E = 0$. Thus an *s*-polarized SPP cannot propagate along a planar metal-dielectric interface.

As we mentioned above, surface plasmon polaritons are surface waves localized at the interface between a metal and a dielectric medium. Field amplitude decays exponentially, in the direction perpendicular to the surface, as $\exp(-\left|k_{i,z} z\right|)$. The value of the distance at which field intensity falls to $1 / e$ is:

$$l_i = \frac{1}{\left|k_{i,z}\right|} \tag{A.11}$$

Inserting eq. (A.7) into (A.6) we get:

$$\begin{aligned} z > 0 \qquad & l_A = \frac{\lambda}{2\pi}\sqrt{-\frac{\varepsilon_A + \varepsilon_1}{\varepsilon_A^2}} \\ z < 0 \qquad & l_B = \frac{\lambda}{2\pi}\sqrt{-\frac{\varepsilon_A + \varepsilon_1}{\varepsilon_B^2}} \end{aligned} \tag{A.12}$$

where ε_1 is the real part of metal dielectric permittivity.

From dispersion relation (A.7), if the dielectric function of the metal is complex $\varepsilon_B = \varepsilon_1 + i\varepsilon_2$, obviously SPP wavevector is complex. In the approximation $\varepsilon_2 \ll \varepsilon_1$, we have:

$$\begin{aligned} k_{SPP} &= \frac{\omega}{c}\sqrt{\frac{\varepsilon_A\left(\varepsilon_1 + i\varepsilon_2\right)}{\varepsilon_A + \varepsilon_1 + i\varepsilon_2}} = \frac{\omega}{c}\sqrt{\frac{\varepsilon_A\left(\varepsilon_1 + i\varepsilon_2\right)\left(\varepsilon_A + \varepsilon_1 - i\varepsilon_2\right)}{\left(\varepsilon_A + \varepsilon_1\right)^2 + \varepsilon_2^2}} \cong \\ &= \frac{\omega}{c}\sqrt{\frac{\varepsilon_A^2\varepsilon_1 + \varepsilon_A\varepsilon_1^2 + i\varepsilon_A^2\varepsilon_2}{\left(\varepsilon_A + \varepsilon_1\right)^2}} = \frac{\omega}{c}\sqrt{\frac{\varepsilon_A\varepsilon_1}{\varepsilon_A + \varepsilon_1}\left(1 + i\frac{\varepsilon_A\varepsilon_1}{\varepsilon_A + \varepsilon_1}\frac{\varepsilon_2}{\varepsilon_1^2}\right)} = \\ &= \frac{2\pi}{\lambda}\sqrt{\frac{\varepsilon_A\varepsilon_1}{\varepsilon_A + \varepsilon_1}} + i\frac{2\pi}{\lambda}\left(\frac{\varepsilon_A\varepsilon_1}{\varepsilon_A + \varepsilon_1}\right)^{\frac{3}{2}}\frac{\varepsilon_2}{2\varepsilon_1^2} \end{aligned} \tag{A.13}$$

Thus the real and imaginary parts of SPP wavevector are given by:

$$\Re\left[k_{SPP}\right] = \frac{2\pi}{\lambda}\sqrt{\frac{\varepsilon_A\varepsilon_1}{\varepsilon_A+\varepsilon_1}}$$
$$\Im[k_{SPP}] = \frac{2\pi}{\lambda}\left(\frac{\varepsilon_A\varepsilon_1}{\varepsilon_A+\varepsilon_1}\right)^{\frac{3}{2}}\frac{\varepsilon_2}{2\varepsilon_1^2} \tag{A.14}$$

The intensity of a surface plasmon wave decreases exponentially in the propagation direction as $\exp\left(-2x\Im\left[k_{SPP}\right]\right)$. The propagation length at which intensity decreases to $1/e$ is:

$$L_{SPP} = \frac{1}{2\Im\left[k_{SPP}\right]} \tag{A.15}$$

Table A collects propagation and extinction lengths for SPPs at the interface between air/water and noble metals (gold/silver), for $\lambda = 632\,\text{nm}$ ($\varepsilon_{Au} = -12.1 + 1.3i$, $\varepsilon_{Ag} = -17.0 + 0.7i$, $\varepsilon_{Air} = 1$, $\varepsilon_{Water} = 1.78$).

Table A: propagation and extinction lengths of SPPs propagating at dielectric/metal interfaces.

Stack ($\lambda = 632\,\text{nm}$)	$L_{SPP}\,(\mu\text{m})$	$l_A\,(\text{nm})$	$l_B\,(\text{nm})$
Air/Au	10.0	335.6	27.8
Air/Ag	38.0	403.0	23.7
Water/Au	3.8	180.9	26.8
Water/Ag	14.8	220.8	23.1

Appendix B

Dielectric function of metals: the Drude model

Optical properties of metals can be coarsely described by the *Plasma Model*, where a gas of free independent electrons of density number n moves in a background of fixed positive ion cores. This simple model, also known as the *Drude Model*, does not take into account details of the lattice potential, nevertheless it provides a valid description of metal optical behaviour over a wide frequency range, up to the ultraviolet for alkali metals, whereas in noble metals interband transitions occur at visible frequencies limiting the validity of this approach.

Under the presence of an external electric field $\boldsymbol{E}$, the motion $\boldsymbol{x}(t)$ of an electron in the plasma sea is given by the solution of:

$$m\frac{d^2\,\boldsymbol{x}}{dt^2} = -m\gamma\frac{d\,\boldsymbol{x}}{dt} - e\,\boldsymbol{E} \tag{B.1}$$

where $\gamma = 1\,/\,\tau$, $m = 9.11\cdot 10^{-31}\,\mathrm{kg}$ is the electron mass and $e = 1.6\cdot 10^{-19}\,\mathrm{C}$ is the electron charge. In Drude theory τ is the relaxation time of the electron sea and it is usually around the order $10^{-14}\,\mathrm{s}$. If we assume a harmonic time dependence with frequency ω for the driving field, a particular solution is given by $\boldsymbol{x}(t) = \boldsymbol{x}_0\,e^{-i\omega t}$. Substituting this expression into eq. (B.1), after rearranging terms we obtain:

$$\boldsymbol{x}(t) = \frac{e}{m\left(\omega^2 + i\omega\gamma\right)}\boldsymbol{E}(t) \tag{B.2}$$

Electrons displacement gives rise to a macroscopic polarization $\boldsymbol{P}$:

$$\boldsymbol{P} = -en\,\boldsymbol{x} = -\frac{ne^2}{m\left(\omega^2 + i\omega\gamma\right)}\boldsymbol{E} \tag{B.3}$$

where n is the free electron density. From the constitutive relation $\boldsymbol{P} = \varepsilon_0\left(\varepsilon_r - 1\right)\boldsymbol{E}$, we obtain an explicit form for the relative dielectric function of the metal in plasma approximation:

$$\varepsilon_r(\omega) = 1 - \frac{\omega_p^2}{w^2 + i\omega\gamma} \tag{B.4}$$

where

$$\omega_p = \sqrt{\frac{ne^2}{m\varepsilon_0}} \tag{B.5}$$

is the so called *plasma frequency* of the free electron gas. This is the frequency of a free collective longitudinal oscillation of the electron gas (*volume plasmons*). Due to the longitudinal nature of these excitations, volume plasmons do not couple to trasverse electromagnetic waves and can only be excited by particle impacts.

For $\omega \gg \gamma$, the imaginary part in eq. (B.4) is negligible and the dielectric function is reduced to:

$$\varepsilon_r(\omega) = 1 - \frac{\omega_p^2}{\omega^2} \tag{B.6}$$

that is a good approximation in the near-UV and UV range.

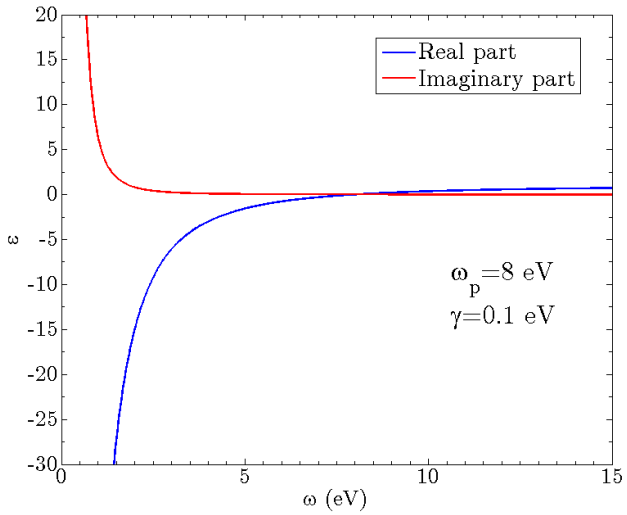

Figure A- 1: dielectric function real (blue line) and imaginary (red line) parts according to Drude model in the case $\omega_p = 8eV$, $\gamma = 0.1eV$.

Appendix C

Bloch-Floquet's theorem

Bloch-Floquet's theorem prescribes the mathematical form for the solutions of the wave-equation in a periodic dielectric medium. In the original formulation it deals with Maxwell equations solution in 1D photonic crystals and it is very similar in its statements and corollaries to Bloch's theorem for electrons in periodic potentials.

If we consider the two curl Maxwell equations and we look for harmonic time-dependent modes with frequency ω, we have:

$$\begin{aligned} \nabla \times \boldsymbol{E}(\boldsymbol{x}) &= i\omega\mu_0 \boldsymbol{H}(\boldsymbol{x}) \\ \nabla \times \boldsymbol{H}(\boldsymbol{x}) &= -i\omega\varepsilon_0\varepsilon(\boldsymbol{x})\boldsymbol{E}(\boldsymbol{x}) \end{aligned} \tag{C.1}$$

We can decouple these two equations by dividing the second equation by $\varepsilon(\boldsymbol{x})$ and then taking the curl. Thereafter by using the first equation to eliminate the electric field, we get an equation entirely in the magnetic field $\boldsymbol{H}$, the *wave-equation*:

$$\nabla \times \left(\frac{1}{\varepsilon(\boldsymbol{x})} \nabla \times \boldsymbol{H}(\boldsymbol{x}) \right) = \frac{\omega^2}{c^2} \boldsymbol{H}(\boldsymbol{x}) \tag{C.2}$$

which, with the divergence equation $\nabla \cdot \boldsymbol{H} = 0$, completely describes the magnetic field.

Wave equation (C.2) assumes the form of an eigenvalue problem, once we define with $\widehat{L}$ the operator on the left side:

$$\widehat{L}[\boldsymbol{H}(\boldsymbol{x})] = \frac{\omega^2}{c^2} \boldsymbol{H}(\boldsymbol{x}) \tag{C.3}$$

Thus the problem leads to determine the modes $\boldsymbol{H}(\boldsymbol{x})$ that are eigenfunctions of the given operator with respect to the eigenvalue ω^2 / c^2. It can be demonstrated that the considered operator is linear and hermitian with respect to the inner product of vector fields:

$$(\boldsymbol{F}, \boldsymbol{G}) = \int d\boldsymbol{x}\ \boldsymbol{F}(\boldsymbol{x})^* \cdot \boldsymbol{G}(\boldsymbol{x}) \tag{C.4}$$

Bloch-Floquet's theorem prescribes the form of solutions for eq. (C.2) in such configurations where the dielectric function $\varepsilon(\boldsymbol{x})$ is a periodic function and describes the structure of a photonic crystal:

$$\varepsilon(\boldsymbol{x}) = \varepsilon(\boldsymbol{x} + \boldsymbol{R}) \tag{C.5}$$

where $\boldsymbol{R}$ is any lattice vector in the form $\boldsymbol{R} = n_1 \boldsymbol{a}_1 + n_2 \boldsymbol{a}_2 + n_3 \boldsymbol{a}_3$, with n_i integer numbers and $\boldsymbol{a}_i$ a proper lattice vector basis. A useful construction is represented by the reciprocal lattice, i.e. the set of such points $\boldsymbol{G} = m_1 \boldsymbol{b}_1 + m_2 \boldsymbol{b}_2 + m_3 \boldsymbol{b}_3$, with m_i integer numbers, that:

$$\boldsymbol{G} \cdot \boldsymbol{R} = 2\pi p \tag{C.6}$$

for any vectors $\boldsymbol{G}$ and $\boldsymbol{R}$ belonging respectively to the reciprocal and direct lattices and p an integer number.

We consider a 1D photonic crystal, i.e. a structure that is periodic in only one direction. If we orient the *x*-axis in the crystal direction, the lattice is completely described by the lattice vector $\mathbf{a} = (a, 0, 0)$, where a is the linear dimension of the unit cell. Reciprocal lattice is one dimensional too and it is fully described by the lattice vector $\mathbf{b} = (2\pi / a, 0, 0)$. In this configuration, the theorem states that solutions of eq. (C.2) have the following form[108]:

$$\boldsymbol{H}_k(\boldsymbol{x}) = e^{i\boldsymbol{k}\cdot\boldsymbol{x}} \boldsymbol{h}_k(\boldsymbol{x}) \tag{C.7}$$

where $\boldsymbol{h}_k$ is a function that preserves the crystal periodicity:

$$\boldsymbol{h}_k(\boldsymbol{x} + n\,\boldsymbol{a}) = \boldsymbol{h}_k(\boldsymbol{x}) \tag{C.8}$$

Since the dielectric function is periodic in the lattice vector direction, the hermitian operator $\widehat{L}$ commutes with the discrete translational operator $\widehat{T}_n$:

$$\widehat{T}_n f(\boldsymbol{x}) = f(\boldsymbol{x} + n\,\boldsymbol{a}) \tag{C.9}$$

$$\left[\widehat{T}_n, \widehat{L}\right] = 0 \tag{C.10}$$

Thus the two operators admit a system of common eigenfunctions[109] and the eigenfunctions of $\widehat{L}$ can be expressed as a linear superposition of $\widehat{T}_n$ eigenfunctions. These modes assume the simple form of plane waves and can be classified by specifying $\boldsymbol{k}$:

$$\widehat{T}_n e^{i\,\boldsymbol{k}\cdot\boldsymbol{x}} = e^{i\,\boldsymbol{k}\cdot\left(\boldsymbol{x}+n\,\boldsymbol{a}\right)} = e^{i\,\boldsymbol{k}\cdot\boldsymbol{x}} e^{in\,\boldsymbol{k}\cdot\boldsymbol{a}} \tag{C.11}$$

However not all values of $\boldsymbol{k}$ yield different eigenvalues. If $\boldsymbol{k}$ is incremented by an integer multiple of the reciprocal vector $\boldsymbol{b}$, the same state is left unchanged, since:

$$e^{i\left(m\,\boldsymbol{b}\cdot n\,\boldsymbol{a}\right)} = e^{2\pi ip} = 1 \tag{C.12}$$

because of reciprocal vector definition (eq. C.6). Thus:

$$\widehat{T}_n e^{i\,\boldsymbol{k}\cdot\boldsymbol{x}} = \widehat{T}_n e^{i\left(\boldsymbol{k}+m\,\boldsymbol{b}\right)\cdot\boldsymbol{x}} = e^{i\,\boldsymbol{k}\cdot\boldsymbol{x}} e^{i\,\boldsymbol{k}\cdot\boldsymbol{a}} \tag{C.13}$$

Since any linear combination of the degenerate eigenfunctions is itself an eigenfunction with the same eigenvector, we can consider linear combinations and put them in the form:

$$\boldsymbol{H}_k\left(\boldsymbol{x}\right) = \sum_m \boldsymbol{c}_{k,m}\left(y,z\right) e^{i\left(\boldsymbol{k}+m\,\boldsymbol{b}\right)\cdot\boldsymbol{x}} = e^{i\,\boldsymbol{k}\cdot\boldsymbol{x}}\,\boldsymbol{h}_k\left(\boldsymbol{x}\right) \tag{C.14}$$

where $\boldsymbol{h}_k\left(\boldsymbol{x}+n\,\boldsymbol{a}\right) = \boldsymbol{h}_k\left(\boldsymbol{x}\right)$.

In this way the discrete periodicity in the *x*-direction leads to a *x*-dependence for a generic solution that is simply expressed by the product of a plane wave $e^{i\,\boldsymbol{k}\cdot\boldsymbol{x}}$ modulated by a *x*-periodic function $\boldsymbol{h}_k\left(\boldsymbol{x}\right)$.

At fixed k_y and k_z, the Bloch state with wavevector k_x and the one with wavevector $k_x + mb$ are identical. Since the k_x-state that differs by integer multiples of b are not different from a physical point of view, also the mode frequency must be periodic in k_x:

$$\omega\left(\boldsymbol{k}\right) = \omega\left(\boldsymbol{k}+m\,\boldsymbol{b}\right) \tag{C.15}$$

Thus we only need to consider k_x in the range $-\pi/a \le k_x \le \pi/a$, values that define the *First Brillouin zone*.

An important consequence of Bloch-Floquet's theorem is that, as a continuous translational symmetry leads to the conservation of the wavevector in that direction, as a consequence of the

disceret translational symmetry the $\boldsymbol{k}$ vector is a conserved quantity, modulus the addition of a reciprocal lattice vector $\boldsymbol{G}$:

$$\boldsymbol{k}_i = \boldsymbol{k}_f + \boldsymbol{G} \tag{C.16}$$

where in the case of a 1D crystal we have $\left|\vec{G}\right| = 2\pi m / a$. Since the operator $\widehat{L}$ has not complete translational invariance in the presence of a non-uniform medium, its eigenstates will not be simultaneous eigenstates of the momentum operator, that is to say of the continuous translational operator. Nevertheless $\boldsymbol{k}$ is a natural extention of the momentum to the case of a photonic crystal and it is usually known as the crystal momentum, to emphasize this similarity, however it should not be confused with an effective momentum, but considered as a set of numbers that classify the state of the system.

Appendix D

Chandezon's method - Addendum.

Incident field

The incident magnetic field with wavevector (3.2.7), in the new coordinate frame (3.2.1), leaving out time dependence, is given by:

$$\boldsymbol{H}^{(i)} = \left(H_x^i, H_y^i, H_z^i\right) e^{i\left(\alpha_0 x+\gamma z\right)} e^{-i\beta_0\left(u+s\left(x\right)\right)} \tag{D.1}$$

A generic incident plane-wave can be described as the superposition of a *TM*-mode and of a *TE*-mode. Thus the electromagnetic fields in the *z*-direction, according to the reference frame in Figure 3-1, are given by:

$$\begin{aligned} H_z^i &= H_{TM}\cos\varphi - H_{TE}\cos\theta\sin\varphi \\ E_z^i &= E_{TE}\cos\varphi + E_{TM}\cos\theta\sin\varphi \end{aligned} \tag{D.2}$$

and using Fourier series we get:

$$\begin{aligned} H_z &= H_z^i e^{-i\beta_0 u} e^{i\gamma z} \sum_m L_m\left(\beta_0\right) e^{i\alpha_m x} \\ E_z &= E_z^i e^{-i\beta_0 u} e^{i\gamma z} \sum_m L_m\left(\beta_0\right) e^{i\alpha_m x} \end{aligned} \tag{D.3}$$

where α_m is given by eq. (3.2.8) and

$$L_m\left(t\right) = \frac{1}{\Lambda}\int_0^\Lambda e^{-i\left(s\left(x\right)t+mGx\right)} dx \tag{D.4}$$

For the *x*-components, inserting eq. (D.3) into Maxwell equations we find out:

$$\begin{aligned} H_x &= e^{-i\beta_0 u} e^{i\gamma z} \frac{1}{\omega\mu - \dfrac{\gamma^2}{\omega\varepsilon}} \sum_m \left(-\beta_0 E_z^i + \frac{\alpha_0}{\beta_0} mGE_z^i - \frac{\gamma}{\omega\varepsilon}\alpha_m H_z^i \right) L_m\left(\beta_0\right) e^{i\alpha_m x} \\ H_x &= e^{-i\beta_0 u} e^{i\gamma z} \frac{1}{\dfrac{\gamma^2}{\omega\mu} - \omega\varepsilon} \sum_m \left(-\beta_0 H_z^i + \frac{\alpha_0}{\beta_0} mGH_z^i + \frac{\gamma}{\omega\mu}\alpha_m E_z^i \right) L_m\left(\beta_0\right) e^{i\alpha_m x} \end{aligned} \tag{D.5}$$

where we used the relation $\alpha_0 \,/\, \beta_0 = s'$.

Asymptotic diffracted fields

The outgoing diffracted field is a superposition of those diffracted orders that satisfy the following conditions:

$$\Im\left[\beta_n\right] = 0 \qquad\qquad \Re\left[\beta_n\right] > 0 \tag{D.6}$$

where β_n is given by eq. (3.2.8). We define U the set of the P values that satisfies previous conditions. Fourier developrments in the *x*-direction become:

$$\begin{aligned} H_z^{as} &= e^{i\gamma z} \sum_{n\in U} \sum_m H_z^{as,n} e^{i\beta_n u} L_{m-n}\left(-\beta_n\right) e^{i\alpha_m x} \\ E_z^{as} &= e^{i\gamma z} \sum_{n\in U} \sum_m E_z^{as,n} e^{i\beta_n u} L_{m-n}\left(-\beta_n\right) e^{i\alpha_m x} \end{aligned} \tag{D.7}$$

After substituting last expressions into Maxwell's equations, we find out the expressions for the diffracted order *x*-components:

$$\begin{aligned} H_x^{as} &= e^{i\gamma z} \frac{1}{\omega\mu - \dfrac{\gamma^2}{\omega\varepsilon}} \sum_{n\in U} \sum_m \left(\beta_n E_z^{as,n} + \frac{\alpha_n}{\beta_n}\left(n-m\right) G E_z^{as,n} - \frac{\gamma}{\omega\varepsilon}\alpha_m H_z^{as,n} \right) L_{m-n}\left(-\beta_n\right) e^{i\left(\alpha_m x + \beta_n u\right)} \\ E_x^{as} &= e^{i\gamma z} \frac{1}{\dfrac{\gamma^2}{\omega\mu} - \omega\varepsilon} \sum_{n\in U} \sum_m \left(\beta_n H_z^{as,n} + \frac{\alpha_n}{\beta_n}\left(n-m\right) G H_z^{as,n} + \frac{\gamma}{\omega\mu}\alpha_m E_z^{as,n} \right) L_{m-n}\left(-\beta_n\right) e^{i\left(\alpha_m x + \beta_n u\right)} \end{aligned} \tag{D.8}$$

where we used the following identity: $\alpha_n \,/\, \beta_n = s'$.

Continuity boundary conditions

Solutions of the eingenvalue problem for the matrix T in the *j*-medium (eq. (3.2.19)) is given by eq. (3.2.25) which can be expressed in vectorial form by:

$$\boldsymbol{w}^j(u) = M^j \Phi^j(u)\, \boldsymbol{b}^j \tag{D.9}$$

where $\boldsymbol{b}^j$ is a vector with components b_q^j, Φ^j is a diagonal matrix with elements $\Phi_{mn}^j = \delta_{mn} e^{i\lambda_m^j u}$, M is a matrix whose columns are the eigenvectors $\boldsymbol{V}_q^j$. Thus the problems lies in the determination of the coefficients b_q^j in each medium. Tangential-field components must be continuous at the media interfaces. The continuity of $\boldsymbol{w}$ at each interface u_j imposes that:

$$M^j \Phi^j(u_j)\,\boldsymbol{b}^j \;=\; M^{j+1}\Phi^{j+1}(u_j)\,\boldsymbol{b}^{j+1} \tag{D.10}$$

from this condition and noting that

$$\begin{aligned} &\Phi^j(u_j)\Big[\Phi^j(u_{j-1})\Big]^{-1} = \Phi^j\left(u_j - u_{j-1}\right) = \Phi^j\left(d_j\right) \\ &\Phi^{M+1}(u_M) = \Phi^{M+1}(0) = 1 \end{aligned} \tag{D.11}$$

we finally get the relation between $\boldsymbol{b}^0$ and $\boldsymbol{b}^{M+1}$:

$$\Theta\,\boldsymbol{b}^0 \;=\; M^{M+1}\,\boldsymbol{b}^{M+1} \tag{D.12}$$

where

$$\Theta = M^M \Phi^M\left(d_M\right)\Big[M^M\Big]^{-1} \cdot \ldots \cdot M^j \Phi^j\left(d_j\right)\Big[M^j\Big]^{-1} \cdot \ldots \cdot M^1 \Phi^1\left(d_1\right)\Big[M^1\Big]^{-1} M^0 \Phi^0\left(-d\right) \tag{D.13}$$

where d_j is the thickness of the j-layer, d is the total thickness of the whole stack. Since we are interested in determining the asymptotic diffracted field, i.e. the calculation of the efficiencies of the diffracted orders, the problem is to determine the coefficients $\boldsymbol{b}^{M+1}$.

Outgoing-wave conditions

Outgoing-wave conditions impose strict restrictions for the solutions in the first and last media. In the substrate, we can keep only the componets b_q^0 whose λ_q^0 corresponds to waves with amplitude decreasing for $y \longrightarrow -\infty$ or which are propagating downward. Since the u dependence is given by $\exp\left(i\lambda_q^0 u\right)$, we must keep such λ_q^0 that:

$$\Im\left[\lambda_q^0\right] < 0 \qquad or \qquad \Im\left[\lambda_q^0\right] = 0 \qquad and \qquad \Re\left[\lambda_q^0\right] < 0 \tag{D.14}$$

In the first medium instead, the situation is much more complicated since we have to distinguish between the incident field, the asymptotic field and the evanescent field contribution:

$$\boldsymbol{w}^{M+1}(u) = M^{M+1}\Phi^{M+1}(u)\,\boldsymbol{b}^{M+1} + e^{-i\beta_0 u}\,\boldsymbol{L} + M'\Phi'(u)\,\boldsymbol{B} \tag{D.15}$$

where $\boldsymbol{L}$ is a $4(2N+1)$-vector given, from eq. (D.3) and (D.5), by:

$$\boldsymbol{L} = \begin{pmatrix} H_x^m \\ E_z^m \\ H_z^m \\ E_x^m \end{pmatrix} = \begin{pmatrix} \dfrac{1}{\omega\mu - \dfrac{\gamma^2}{\omega\varepsilon}}\left(-\beta_0 + \dfrac{\alpha_0}{\beta_0} mG\right) L_m(\beta_0) & -\dfrac{1}{\omega\mu - \dfrac{\gamma^2}{\omega\varepsilon}}\left(\dfrac{\gamma}{\omega\varepsilon}\alpha_m\right) L_m(\beta_0) \\ L_m(\beta_0) & 0 \\ 0 & L_m(\beta_0) \\ -\dfrac{1}{\omega\varepsilon - \dfrac{\gamma^2}{\omega\mu}}\left(\dfrac{\gamma}{\omega\mu}\alpha_m\right) L_m(\beta_0) & -\dfrac{1}{\omega\varepsilon - \dfrac{\gamma^2}{\omega\mu}}\left(-\beta_0 + \dfrac{\alpha_0}{\beta_0} mG\right) L_m(\beta_0) \end{pmatrix} \begin{pmatrix} E_z^i \\ H_z^i \end{pmatrix} \tag{D.16}$$

with m assuming values from $-N$ to N.

M' is a $4(2N+1)\times 2P$ matrix and $\boldsymbol{B}$ is a $2P$ vector:

$$M' = \begin{pmatrix} \dfrac{1}{\omega\mu - \dfrac{\gamma^2}{\omega\varepsilon}}\left(\beta_n + \dfrac{\alpha_n}{\beta_n}(n-m)G\right) L_{m-n}(-\beta_n) & -\dfrac{1}{\omega\mu - \dfrac{\gamma^2}{\omega\varepsilon}}\left(\dfrac{\gamma}{\omega\varepsilon}\alpha_m\right) L_{m-n}(-\beta_n) \\ L_{m-n}(-\beta_n) & 0 \\ 0 & L_{m-n}(-\beta_n) \\ -\dfrac{1}{\omega\varepsilon - \dfrac{\gamma^2}{\omega\mu}}\left(\dfrac{\gamma}{\omega\mu}\alpha_m\right) L_{m-n}(-\beta_n) & -\dfrac{1}{\omega\varepsilon - \dfrac{\gamma^2}{\omega\mu}}\left(\beta_n + \dfrac{\alpha_n}{\beta_n}(n-m)G\right) L_{m-n}(-\beta_n) \end{pmatrix} \tag{D.17}$$

$$\boldsymbol{B} = \begin{pmatrix} E_z^{as,n} \\ H_z^{as,n} \end{pmatrix} \tag{D.18}$$

with m assuming values from $-N$ to N, $n \in U$.

The outgoing-wave condition in the first medium imposes that we must keep only such components b_q^{M+1} whose λ_q^{M+1} satisfies:

$$\Im\left[\lambda_q^{M+1}\right] > 0 \tag{D.19}$$

Truncation

After truncation to order N, matrix T has a size $4(2N+1)$ and we have to solve in each medium its eigenvalue problems in order to determine the matrices M^j and Φ^j. From the form of T it can be demonstrated[44] that the number of values λ_q^0 that satisfies conditions (D.14) is equal to $2(2N+1)$ and the number of unkown components b_q^0 is exactly $2(2N+1)$. In the same way the number of values λ_q^{M+1} satisfying eq. (D.19) is $2(2N+1-P)$, so the number of unknown components in $\boldsymbol{b}^{M+1}$ is $2(2N+1-P)$. Moreover $\boldsymbol{B}$ has $2P$ components to be determined. In this way eq. (D.12) is a linear system of $4(2N+1)$ equations with $4(2N+1)$ unknowns. By using the classical theory of determinants of finite order[56], it can be shown that the solutions of an eigenvalue problem with truncated matrices tends to the exact solution for increasing truncation order.

Application to sinusoidal gratings

In this work we implemented Chandezon's method for the solution of the diffraction problem of multi-layered sinusoidal gratings with profiles described by the function $s(x)$:

$$y = s(x) = A\sin Gx \tag{D.20}$$

where A is grating amplitude and $G = 2\pi / \Lambda$ grating momentum, Λ being the period. Fourier coefficients C_m and D_m of profile functions $C(x)$ and $D(x)$ in eq. (3.2.15) to (3.2.18) are given by:

$$\begin{aligned}
C(x) &= \frac{1}{1+s'(x)^2} \\
&= \frac{1}{1+\left(AG\cos Gx\right)^2} \\
&= \sum_{n=0}^{+\infty}\frac{1}{n!}\left[\prod_{i=0}^{n-1}(-1-i)\right]\left(AG\cos Gx\right)^{2n} \\
&= \sum_{n=0}^{+\infty}\frac{1}{n!}\left[\prod_{i=0}^{n-1}(-1-i)\right]\left(\frac{AG}{2}\right)^{2n}\sum_{p=0}^{2n}\frac{2n!}{p!(2n-p)!}e^{2iGx(p-n)} \\
&= \sum_{m=-\infty}^{+\infty}\left\{\sum_{n\geq|m|/2}^{+\infty}\frac{1}{n!}\left[\prod_{i=0}^{n-1}(-1-i)\right]\left(\frac{AG}{2}\right)^{2n}\frac{2n!}{\left(n+\frac{m}{2}\right)!\left(n-\frac{m}{2}\right)!}\right\}e^{imGx}
\end{aligned} \tag{D.21}$$

with the position $m = p - n$ and m even values. We applied Euler's definitions of trigonometric functions and the binomial series. From previous development we get the following form for Fourier coefficients C_m :

$$\begin{aligned}
&\Big(even \quad m\Big) \qquad C_m = \sum_{n \geq |m|/2}^{+\infty} \frac{1}{n!}\left[\prod_{i=0}^{n-1}(-1-i)\right]\left(\frac{AG}{2}\right)^{2n} \frac{2n!}{\left(n+\frac{m}{2}\right)!\left(n-\frac{m}{2}\right)!} \\
&\Big(odd \quad m\Big) \qquad C_m = 0
\end{aligned} \tag{D.22}$$

$$\begin{aligned}
D(x) &= \frac{s'(x)}{1+s'(x)^2} \\
&= \frac{AG\cos Gx}{1+\big(AG\cos Gx\big)^2} \\
&= \sum_{n=0}^{+\infty}\frac{1}{n!}\left[\prod_{i=0}^{n-1}(-1-i)\right]\big(AG\cos Gx\big)^{2n+1} \\
&= \sum_{n=0}^{+\infty}\frac{1}{n!}\left[\prod_{i=0}^{n-1}(-1-i)\right]\left(\frac{AG}{2}\right)^{2n+1}\sum_{p=0}^{2n+1}\frac{\big(2n+1\big)!}{p!\big(2n+1-p\big)!}e^{2iGx(p-n-\frac{1}{2})} \\
&= \sum_{m=-\infty}^{+\infty}\left\{\sum_{n\geq\frac{|m|+1}{2}}^{+\infty}\frac{1}{n!}\left[\prod_{i=0}^{n-1}(-1-i)\right]\left(\frac{AG}{2}\right)^{2n+1}\frac{\big(2n+1\big)!}{\left(n+\frac{m}{2}+\frac{1}{2}\right)!\left(n-\frac{m}{2}-\frac{1}{2}\right)!}\right\}e^{imGx}
\end{aligned} \tag{D.22}$$

with the position $m = 2p - 2n - 1$ and m odd values. From previous development we get the following form for Fourier coefficients D_m :

$$\begin{aligned}
&\Big(even \quad m\Big) \qquad D_m = 0 \\
&\Big(odd \quad m\Big) \qquad D_m = \sum_{n\geq(|m|+1)/2}^{+\infty}\frac{1}{n!}\left[\prod_{i=0}^{n-1}(-1-i)\right]\left(\frac{AG}{2}\right)^{2n+1}\frac{\big(2n+1\big)!}{\left(n+\frac{m}{2}+\frac{1}{2}\right)!\left(n-\frac{m}{2}-\frac{1}{2}\right)!}
\end{aligned} \tag{D.23}$$

As regards the coefficients $L_m(t)$ in the expansion of the incident (D.16) and propagating fields (D.17), they describe the Fourier weights of the function $e^{-its(x)}$. From the definition D.4 we have:

$$
\begin{aligned}
e^{-its(x)} &= e^{-itA\sin Gx} = e^{-itA\frac{e^{iGx}-e^{-iGx}}{2i}} = e^{-\frac{At}{2}e^{iGx}}\, e^{\frac{At}{2}e^{-iGx}} \\
&= \left[\sum_{n=0}^{+\infty}\frac{1}{n!}\left(-\frac{At}{2}\right)^{n} e^{inGx}\right]\left[\sum_{p=0}^{+\infty}\frac{1}{p!}\left(\frac{At}{2}\right)^{p} e^{-ipGx}\right] \\
&= \sum_{n,p=0}^{+\infty}\left(-1\right)^{n}\frac{1}{n!\,p!}\left(\frac{At}{2}\right)^{n+p} e^{i(n-p)Gx} \\
&= \sum_{m=-\infty}^{+\infty}\left[\sum_{p=-m}^{+\infty}\left(-1\right)^{m+p}\frac{1}{\left(m+p\right)!\,p!}\left(\frac{At}{2}\right)^{2p+m}\right] e^{imGx}
\end{aligned}
\tag{D.24}
$$

where we substituted $n - p = m$. Thus we obtain the following expression:

$$
L_m\left(t\right) = \left(-1\right)^{m}\left(\frac{At}{2}\right)^{m}\sum_{p=-m}^{+\infty}\left(-1\right)^{p}\frac{1}{\left(p+m\right)!\,p!}\left(\frac{At}{2}\right)^{2p} \tag{D.25}
$$

Previous calculations may result useful in order to get an approximated expression of the coefficients C_m and D_m in case of shallow gratings ($A / \Lambda \sim 0.01 \div 0.10$) without losing too much in accuracy. For example, by approximating to the fifth order in the ratio $\rho = A / \Lambda$ we have:

Order	C_n	D_n
0	$1 - 2\left(\pi\rho\right)^2 + 6\left(\pi\rho\right)^4$	0
±1	0	$\pi\rho - 3\left(\pi\rho\right)^3 + 10\left(\pi\rho\right)^5$
±2	$-\left(\pi\rho\right)^2 + 4\left(\pi\rho\right)^4$	0
±3	0	$-\left(\pi\rho\right)^3 + 5\left(\pi\rho\right)^5$
±4	$\left(\pi\rho\right)^4$	0
±5	0	$\left(\pi\rho\right)^5$
$\left\|n\right\| > 5$	0	0

Other modal methods for diffraction gratings

At the time Chandezon introduced his method, another modal method, the Rigorous Coupled-Wave Analysis[110,111] (RCWA) was widely used. This method consists in eliminating the *y*-dependency of the complex permittivity so that it is possible to write the solution inside the grooves as a Fourier expansion, since only a dependency on the periodic coordinate *x* is present. The way RCWA

accomplishes this, is by slicing up the grating domain so that inside each slice, the permittivity only depends on x. At the boundaries between two slices, the tangential components of the electromagnetic fields are continuous. In this way, the unknown reflection and transmission coefficients of the upper and lower halfspace can be connected to each other and determined as in Chandezon's method. Introducing the Fourier expansion gives an eigenvalue problem of size $2N+1$ for both TE and TM polarization for every slice. Comparing RCWA and the C-method we have that:

- There is one eigenvalue problem per layer of size $2N+1$ for RCWA instead of one per medium of size $4N+2$ for the C method.
- RCWA solves one eigenvalue system for each polarization state, while the C method solves one eigenvalue system for both TE and TM polarization simultaneously.
- RCWA approximates the grating interface, while the C-method does not.
- RCWA can handle all types of diffraction gratings, including overhanging gratings, while the C-method is restricted to interfaces which can be described by a regular function of the periodicity coordinate.

It can be shown that the number of layers needed to approximate the grating and obtain an accurate result, is the most important criterium and not the number of harmonics. Secondly, for general grating profiles the C-method will obtain the answer with less computational efforts in terms of truncation order.

Thus the C-method is the most suitable and efficient method in case of periodic gratings described by a regular function, since no approximation of the profile is required with respect to RCWA. On the other hand RCWA represents the best choice in the case of a digital grating stack.

Ringraziamenti

Un grazie ai miei genitori, che mi hanno supportato durante questi ennesimi 3 anni di studio e senza i quali non sarei arrivato fino a questo traguardo.

Un augurio a mio fratello Enrico affinche' abbia successo nei suoi studi appena iniziati e possa sempre nella vita avere la possibilita' di fare cio' che piu' gli piace.

Un grazie di cuore a Diana, per avermi regalato la serenita'.

Un grazie ad Enrico Francesco Nicolo' Stefano Francesco e Manuel. Perche' non importa se vicino o lontano, nella vita un amico c'e' e ci sara' sempre.

Un grazie a tutti i ragazzi di Realta' Veneta, per avermi insegnato che la 'P'olitica non e' nulla senza la passione e l'amicizia.

Un grazie alle associazioni e ai gruppi parrocchiali del paese, per avermi fatto scoprire che del tempo donato agli altri vale ben piu' di quello dedicato solamente a se stessi.

Un grazie particolare alla mia nonna, che con le sue candele accese mi e' stata sempre vicina durante gli studi e i miei viaggi intorno al mondo.

Bibliography

[1] S. A. Maier, Plasmonics: Fundamentals and Applications, Springer (2007).

[2] R. W. Wood, "On a remarkable case of uneven distribution of light in a diffraction grating spectrum", *Philos. Mag.* **4**, 396-402 (1902).

[3] U. J. Fano, "The Theory of Anomalous Diffraction Gratings and of Quasi-Stationary Waves on Metallic Surfaces (Sommerfeld's Waves)", *Opt. Soc. Am.* **31**, 213-222 (1941).

[4] A. Otto, "Excitation of nonradiative Surface Plasma Waves in Silver by the Method of Frustrated Total Reflection", *Z. Phys.* **216**, 398-410 (1968).

[5] E. Kretschmann, H. Z. Raether, "Radiative decay of non-radiative surface plasmons excited by light", *Naturforsch* **23**, 2135-2136 (1968).

[6] J. J. Cowan, E. T. Arakawa, "Dispersion of surface plasmons in dielectric-metal coatings on concave diffraction gratings", *Zeitschrift fur Physik* **235**, 97 (1970).

[7] D. Habauzit, J. Chopineau, B. Roig, "SPR based Biosensor: a biodetection tool for hormonal compounds detection", *Anal. Bioanal. Chem.* **387**, 1215-1223 (2007).

[8] R. L. Rich, D. G. Myszka, "Survey of the 1999 surface plasmon resonance biosensor literature", *J. Mol. Recognit.* **13**, 388-407 (2000).

[9] B. Pejcic, R. De Marco, G. Parkinson, "The role of biosensors in the detection of emerging infectious deseases", *Analyst* **131**, 1079-1090 (2006).

[10] K. V. Gobi, H. Tanaka, Y. Shoyama, N. Miura, "Continuous flow immunosensor for highly selective and real-time detection of sub-ppb levels of 2-hydroxybiphenyl by using surface plasmon resonance imaging", *Biosens. Bioelectron.* **20**, 350-357 (2004).

[11] P. M. Fratamico, T. P. Strobaugh, M. B. Medina, A. G. Gehring, "Detection of Escherichia coli O157:H7 using a surface plasmon resonance biosensor", *Biotechnol. Tech.* **12**, 571-576 (1998).

[12] J. D. Jackson, *Classical Electrodynamics*, *3rd edition,* Hamilton Printing Company (1998).

[13] E. D. Palik, *Handbook of Optical Constants of Solids*. Academic Press, Orlando, Florida (1991).

[14] N. W. Ashcroft, N. D. Mermin, *Solid State Physics*, Thomson Brookes – Cole (1976).

[15] H. Raether, *Surface plasmons on smooth and rough surfaces and on gratings*, Springer-Verlag (1980).

[16] E. Kretschmann, *Z. Phys.* **241**, 313-324 (1971).

[17] J. Homola, S. S. Yee, G. Gauglitz, "Surface Plasmon resonance sensors: review", *Sensors and*

Actuators B **54**: 3-15 (1999).

[18] J. Homola, "Surface Plamon Resonance Sensors for Detection of Chemical and Biological Species", *Chem. Rev.* **108**, 462-493 (2008).

[19] K. Matsubara, S. Kawata, S. Minami, "A compact Surface Plasmon Resonance Sensor for Measurement of Water in Process", *Appl. Spectrosc.* **42**, 1375-1379 (1988).

[20] L. M. Zhang, D. Uttamchandam, "Optical chemical sensing employing surface plasmon resonance", *Electron. Lett.* **24**, 1469 (1988).

[21] C. Nylander, B. Liedberg, T. Lind, "Gas detection by means of surface plasmon resonance", *Sens. Actuators* **3**, 79-88 (1982).

[22] J. M. Brockman, B. P. Nelson, R. M. Corn, "Surface plasmon resonance imaging measurements of ultrathin organic films", *Annu. Rev. Phys. Chem.* **51**, 41-63 (2000).

[23] J. Homola, *Surface Plasmon Resonance Based Sensors*, Springer (2006).

[24] K. Kukanskis, J. Elkind, J. Melendez, T. Murphy, G. Miller, H. Garner, "Detection of DNA hybridization using the TISPR-1 surface plasmon resonance biosensor", *Anal. Biochem.* **274**, 7-17 (1999).

[25] S. Sjolander, C. Urbanitzky, "Integrated fluid handling system for biomolecular interaction analysis", *Anal. Chem.* **63**, 2338-2345 (1991).

[26] T. M. Chinowsky, L. S. Jung, S. S. Yee, "Optimal linear data analysis for surface plasmon resonance biosensors", *Sens. Actuators B* **54**, 89-97 (1999).

[27] K. Johansen, R. Stalberg, I. Lundstrom, B. Liedberg, "Surface Plasmon Resonance: Instrumental Resolution using Photo Diode Arrays", *Meas. Sci. Tech.* 11, 1630-1638 (2000).

[28] V. Thomsen, D. Schatzlein, D. Mercuro, "Limits of detection in spectroscopy", *Spectroscopy* **18**, 112-114 (2003).

[29] B. Sepulveda, A. Calle, L. M. Lechuga, G. Ermelles, "Highly sensitive detection of biomolecules with the magneto-optic surface-plasmon-resonance sensor", *Opt. Lett.* **31**, 1085-1087 (2006).

[30] M. Piliarik, H. Vaisocherova, J. Homola, "A new surface plasmon resonance sensor for high-throughput screening applications", *J. Biosens. Bioelectron.* **20**, 2104-2110 (2005).

[31] R. Karlsson, R. Stahlberg, "Surface plasmon resonance detection and multispot sensing for direct monitoring of interactions involving low-molecular-weight analytes and for determination of low affinities", *Anal. Biochem.* **228**, 274-280 (1995)

[32] J. Homola, I. Koudela, S. S. Yee, "Surface plasmon resonance sensor based on diffraction gratings

and prism couplers: sensitivity comparison", *Sens. Actuators B* **54**, 16-24 (1999).

[33] J. Homola, J. Dostalek, S. F. Chen, A. Rasooly, S. Y. Jiang, S. S. Yee, "Spectral Surface Plasmon Resonance Biosensor for Detection of Staphylococcal Enterotoxin B (SEB) in milk", *Int. J. Food Microbiol.* **75**, 61 (2002).

[34] G. G. Nenninger, P. Tobiska, J. Homola, S. S. Yee, "Long-range surface plasmons for high-resolution surface plasmon resonance sensors", *Sens. Actuators B* **74**, 145-151 (2001).

[35] R. Slavik, J. Homola, "Ultrahigh resolution long range surface plasmon-based sensor", *Sens Actuators B* **123**, 10-12 (2007).

[36] X. D. Hoa, A. G. Kirk, and M. Tabrizian, "Towards integrated and sensitive surface plasmon resonance biosensors: a review of recent progress", *Biosens. Bioelectron.* **23**, 151-160 (2007).

[37] K. H. Yoon, M. L. Shuler, and S. J. Kim, "Design and optimization of nano-grating surface plasmon resonance sensors", *Opt. Express* **14**, 4842-4249 (2006).

[38] D. W. Unfricht, S. L. Colpitts, S. M. Fernandez and M. A. Lynes, "Grating-coupled surface plasmon resonance: a cell and protein microarray platform", *Proteomics* **5**, 4432-4442 (2005).

[39] J. Dostalek, J. Homola, M. Miler, "Rich information format surface plasmon resonance biosensor based on array of diffraction gratings", *Sens. Actuators B* **107**, 154-161 (2005).

[40] C. J. Alleyne, A. G. Kirk, R. C. McPhedran, N. A. P. Nicorovici, and D. Maystre, "Enhanced SPR sensitivity using periodic metallic nanostructures", *Opt. Express* **15**, 8163-8169 (2007).

[41] O. Telezhnikova, J. Homola, "New approach to spectroscopy of surface plasmons", *Opt. Lett.* **31**, 3339-3341 (2006).

[42] F. Romanato, K. H. Lee, H. K. Kang, C. C. Wong, Y. Zong and W. Knoll, "Azimuthal dispersion and energy mode condensation of grating-coupled surface plasmon polaritons", *Phys. Rev. B* **77**, 245435-245441 (2008).

[43] F. Romanato, K.H. Lee, G. Ruffato and C.C.Wong, "The role of polarization on surface plasmon polariton excitation on metallic gratings in the conical mounting", *Appl. Phys. Lett.* **96**, 111103 (2010).

[44] J. Chandezon, D. Maystre and G. Raoult, "A new theoretical method for diffraction gratings and its numerical application", *J. Optics (Paris)* **11**, No. 4, 235-241 (1980).

[45] J. Chandezon, M.T. Dupuis and G. Cornet, "Multicoated gratings: a differential formalism applicable in the entire optical region", *J. Opt. Soc. Am.* **72**, No. 7, 839-846 (1982).

[46] S.J. Elston, G.P. Bryan-Brown and J.R. Sambles, "Polarization conversion from diffraction gratings", *Phys. Rev. B* **44**, No.12, 6393-6400 (1991).

[47] G. Granet, J.P. Plumey and J. Chandezon, "Scattering by a periodically corrugated dielectric layer with non identical faces", *Pure Appl. Opt.* **4**, No.1, 1-5 (1995).

[48] T.W. Preist, N.P.K. Cotter and J.R. Sambles, "Periodic multilayer gratings of arbitrary shape", *J. Opt. Soc. Am. A* **12**, No. 8, 1740-1749 (1995).

[49] L. Li, G. Granet, J.P. Plumey and J. Chandezon, "Some topics in extending the C-method to multilayer-coated gratings of different profiles", *Pure Appl. Opt.* **5**, No.2, 141-156 (1996).

[50] J.P. Plumey, B. Guizal and J. Candezon, "Coordinate transformation method as applied to asymmetric gratings with vertical facets", *J. Opt. Soc. Am. A* **14**, No. 3, 610-617 (1997).

[51] L. Li, "Multilayer-coated diffraction gratings: differential method of Chandezon et al. revisited", *J. Opt. Soc. Am. A* **11**, 2816-2828 (1994).

[52] L. Li, "Using symmetries of grating groove profiles to reduce computation cost of the C-method", *J. Opt. Soc. Am. A* **24**, 1085-1096 (2007).

[53] E.J. Post, *Formal Structure of Electromagnetics* (North-Holland, Amsterdam, 1962).

[54] A. Zygmund, *Trigonometric Series* (Cambridge U. Press, Cambridge 1977).

[55] L. Li, "Use of Fourier series in the analysis of discontinuous periodic structures", *J. Opt. Soc. Am. A* **13**, No. 9 (1996).

[56] L. Li, "Justification of matrix truncation in the modal methods of diffraction gratings", *J. Opt. A: Pure Appl. Opt.* **1**, 531-536 (1999).

[57] G. Ruffato and F. Romanato, "Near-field numerical analysis of Surface Plasmon Polaritons propagation on metallic gratings". Accepted by *The internation journal for computation and mathematics in electrical and electronic engineering* (Special Issue June 2012).

[58] G. Ruffato, G. Zacco and F. Romanato, "Surface Plasmon Polaritons Excitation and Propagation on Metallig Gratings: far-field and near-field numerical simulations", accepted by *Journal of Materials Science and Engineering A* (2011).

[59] S. Ekgasit, C. Thammacharoen and W. Knoll, "Surface Plasmon Resonance Spectroscopy Based on Evanescent Field Treatment", *Anal. Chem.* **76**, 561-568 (2004).

[60] W. Hinsberg, F. A. Houle, J. Hoffnagle, M. Sanchez, G. Wallraff, M. Morrison, S. Frank, "Deep-ultraviolet interferometric lithography as a tool for assessment of chemically amplified photoresist perfomormance", *Journal of Vacuum Science and Technology B* **16**, 3689 (1998).

[61] F. Romanato, H. K. Kang, K. H. Lee, G. Ruffato, M. Prascolu, C. C. Wong, "Interferential lithography of 1D thin metallic sinusoidal gratings: accurate control of the profile for azimuthal angular dependent plasmonic effects and applications", *Microelectronic Engineering* **86**, 573-576 (2009).

[62] G. Zacco, F. Romanato, A. Sonato, D. Sammito, G. Ruffato, M. Morpurgo, D. Silvestri, M. Carli, P. Schiavuta, G. Brusatin, "Sinusoidal plasmonic crystals for bio-detection sensors", *Microelectronic Engineering* **88**, 1898 (2011).

[63] Technical data sheet for NOA optical adhesives; Norland Products, Inc.: New Brunswick, NJ.

[64] B. Bhushan, *Handbook of Nanotechnology*, Springer (2004).

[65] N. Yao, Z. L. Wang, *Handbook of Microscopy for Nanotechnology*, Springer (2005).

[66] H. Fujiwara, *Spectroscopic Ellipsometry – Principles and Applications*, Wiley (2007).

[67] D. E. Aspnes and A. A. Studna, "High precision scanning ellipsometer", *Appl. Opt.* **14**, 220-228 (1975).

[68] Y. T. Kim, R. W. Collins, K. Vedam, "Fast scanning spectroelectrochemical ellipsometry: in situ characterization of gold oxide"*, Surf. Sci.,* **223**, 341-350 (1990).

[69] A. Roseler and W. Molgedey, "Improvement in accuracy of spectroscopic IR ellipsometry by the use of IR retarders", *Infrared Physics* **24**, 1-5 (1984).

[70] M. Bass, *Handbook of Optics,* 2nd ed., McGraw-Hill (1995).

[71] R. C. Jones, "A new calculus for the treatment of optical systems: description and discussion of the calculus", *J. Opt. Soc. Am.* **31**, 488-493 (1941).

[72] W. G. Driscoll, W. Vaughan, *Handbook of Optics*, McGraw-Hill (1978).

[73] J. M. M. de Nijs and A. van Silfhout, "Systematic and random errors in rotating analyzer ellipsometry", *J. Opt. Soc. Am. A*, **5**, 773-781 (1988).

[74] A. Roseler. "IR spectroscopic ellipsometry: instrumentation and results", *This Solid Films*, **234**, 307-313 (1993).

[75] J. T. Cabral, S. D. Hudson, C. Harrison, and J. F. Douglas*,* "Frontal Photopolymerization for Microfluidic Applications", *Langmuir* 20, 10020-10029 (2004).

[76] E. Dorsey, *Properties of Ordinary Water-Substance*, Reinhold Publishing Corporation (1940).

[77] L. S. Jung, C. T. Campbell, T. M. Chinowsky, M. N. Mar, S. S. Yee, "Quantitative Interpretation of the Response of Surface Plasmon Resonance Sensors to Adsorbed Films", *Langmuir* **1998**, 14, 5636-5648 (1998).

[78] A. Ulman, "Formation and Structure of Self-Assembled Monolayers", *Chem. Rev.* **96**, 1533-1554 (1996).

[79] X. F. Ang, F. Y. Li, W. L. Tan, Z. Chen and C. C. Wong, "Self-assembled monolayer for reduced temperature direct metal thermocompression bonding", *Appl. Phys. Lett.* **91**, 061913 (2007).

[80] C. D. Bain, E. B. Troughton, Y. T. Tao, J. Evall, G. M. Whitesides, R. G. Nuzzo, "Formation of monolayer films by the spontaneous assembly organic thiols from solution onto gold", *J. Am. Chem. Soc.* **111**, 321-335 (1989).

[81] Y. Martin, P. Vermette, "Low-Fouling Amine-Termintaed Poly(ethylene glycol) Thin Layers and Effect of Immobilization Conditions on Their Mechanical and Physicochemical Properties", *Macromolecules* **39**, 8083-8091 (2006).

[82] A. Sonato, G. Ruffato, M. Natali, G. Zacco, M. Morpurgo, D. Silvestri, M. Dettin and F. Romanato, "Plasmonic platforms for biodetection devices", *2011 International Workshop on Biophotonics*, DOI: 10.1109/IWBP.2011.5954822 (2011).

[83] Z. Ma, G. Zhang, X. Zhai, L. Jin, X. Tang, M. Yang, P. Zheng, W. Wang, "Fractal crystal growth of poly(ethylene oxide) crystals from its amorphous monolayers", *Polymer* **49**, 6, 1629-1634 (2008).

[84] J. E. Mark and P. J. Flory, "The configuration of the Polyoxyethylene Chain", *Journal of the American Chemical Society* **87**, 7, 1415-1423 (1965).

[85] Y. Ding, M. W. Chen, J. Erlebacher, "Metallic mesoporous nanocomposites for electrocatalysis", *J. Am. Chem. Soc.* **126**, 6876-6877 (2004).

[86] A. Wittstock, J. Biener, M. Baumer, "Nanoporous gold: a new material for catalytic and sensor applications", *Chem. Phys. Chem.* **12**, 12919-12930 (2010).

[87] M. B. Cortie, A. I. Maaroof, G. B. Smith, "Electrochemical capacitance of mesoporous gold", *Gold Bull.* **38**, 14-22 (2005).

[88] X. Lang, L. Quian, P. Guan, J. Zi and M. Chen, "Localized surface plasmon resonance of nanoporous gold", *Appl. Phys. Lett.* **98**, 093701 (2011).

[89] T. Fujita, L. H. Qian, K. Inoke, J. Erlebacher and M. W. Chen, "Three-dimensional morphology of nanoporous gold", *Appl. Phys. Lett.* **92**, 251902 (2008).

[90] J. Biener, G. W. Nyce, A. M. Hodge, M. M. Biener, A. Hamza and S. A. Maier, "Nanoporous Plasmonic Metamaterials", *Advanced Materials* **20**, 1211-1217 (2008).

[91] N. A. Senior and R. C. Newman, "Synthesis of tough nanoporous metals by controlled electrolytic dealloying", *Nanotechnol.* **17**, 2311-2316 (2006).

[92] X. Lu, T. J. Balk, R. Spolenak and E. Arzt, "Dealloying of Au-Ag thin films with a composition gradient: influence on morphology of nanoporous Au" *Thin Solid Films* **515**, 7122-7126 (2007).

[93] S. Cattarin, D. Kramer, A. Lui and M. Musiani, " Preparation and characterization of goold nanostructures of controller dimension by electrochemical techniques", *J. Phys. Chem. C* **111**, 12643-12649 (2007).

[94] S. Cattarin, D. Kramer, A. Lui and M. Musiani, "Formation of nanostructured gold sponges by anodic dealloying. EIS investigation of product and process", *Fuel Cells* **9**, 209-214 (2009).

[95] S. Parida, D. Kramer, C. A. Volkert, H. Rosner, J. Erlebacher, J. Weissmuller, "Volume change during the formation of nanoporous gold by dealloying" *Phys. Rev. Lett.* **97**, 035504 (2006).

[96] Y. Sun and T. J. Balk, "Evolution of structure, composition and stress in nanoporous gold thin films with grain-boundary cracks", *Metall. Mater. Trans. A* **39**, 2656-2665 (2008).

[97] K. M. Mayer and J. H. Hafner, "Localized Surface Plasmon Resonance Sensors", *Chem. Rev.* **111**, 3828-3857 (2011).

[98] G. B. Smith, A. I. Maaroof and A. Gentle, "Homogenized Lorentz-Drude optical response in highly nanoporous conducting gold layers produced by de-alloying", *Optics Communications* **271**, 263-268 (2007).

[99] R. W. Cohen, G. D. Cody, M. D. Coutts and B. Abeles, "Optical properties of granular silver and gold films", *Physical Review B* **8**, 3689-3701 (1973).

[100] F. Yu, S. Ahl, A. M. Caminade, J. P. Majoral, W. Knoll, J. Erlebacher, "Simultaneous excitation of propagating and localized surface Plasmon resonance in nanoporous gold membranes", *Anal. Chem.* **78**, 7346-7350 (2006).

[101] M. C. Dixon, T. A. Daniel, M. Hieda, D. M. Smilgies, M. H. W. Chan, D. L. Allara, "Preparation, structure and optical properties of nanoporous gold thin films" *Langmuir* **23**, 2414-2422 (2007).

[102] A. I. Mararoof, A. Gentle, G. B. Smith, M. B. Cortie, "Bulk and surface plasmons in highly nanoporous gold films" *J.Phys. D. appl. Phys*. **40**, 5675-5682 (2007).

[103] F. Romanato, K. H. Lee, H. K. Kang, G. Ruffato and C. C. Wong, "Sensitivity enhancement in grating coupled surface plasmon resonance by azimuthal control", *Opt. Express* **17**, 12145-12154 (2009).

[104] G. Ruffato and F. Romanato, "Grating-Coupled Surface Plasmon Resonance in the conical mounting with polarization modulation", submitted to *Optics Letters* (2012).

[105] W. H. Press, S. A. Teukolsky, W. Vetterling, B. P. Flannery, *Numerical Recipes in C++: the art of scientific computing*, 2nd edition, Cambridge University Press (2002).

[106] R. L. Aggarwal, L. W. Farrar, E. D. Diebold and D. L. Polla, "Measurement of the absolute Raman scattering cross section of the 1584-cm^{-1} band of benzenethiol and the surface-enhanced Raman scattering cross section enhancement factor for femtosecond laser-nanostructured substrates", *J. Raman Spectroscopy* **40**, 1331-1333 (2009).

[107] G. Ruffato, F. Romanato, D. Garoli, S. Cattarin, "Nanoporous gold plasmonic structures for sensing

applications", *Opt. Express* **19**, 13164-13170 (2011).

[108] J. D. Joannopoulos, S. G. Johnson, J. N. Winn, R. D. Meade, *Photonic Crystals – Molding the Flow of Light*, Princeton University Press (2008).

[109] G. B. Arfken, H. J. Weber, F. E. Harris, *Mathematical Methods for Physicists*, Sixth edition, Elsevier (2005).

[110] M. G. Moharam and T. K. Gaylord, "Rigorous coupled-wave analysis of planar-grating diffraction", *J. Opt. Soc. Am.* **71**, 811-818 (1981).

[111] M. G. Moharam, D. A. Pommet, E. B. Grann, T. K. Gaylord, "Stable implementation of the rigorous coupled-wave analysis for surface-relief gratings: enhanced transmittance matrix approach", *J. Opt. Soc. Am. A* **12**, 5, 1077-1086 (1995).